공학박사학위논문

고압터빈 노즐 냉각을 위한 막냉각 홀 배열의 강건 최적설계

Robust Design Optimization of Film Cooling Hole Array for High Pressure Turbine Nozzle

2017 년 2 월

서울대학교 대학원

기계항공공학부

이 상 아

고압터빈 노즐 냉각을 위한 막냉각 홀 배열의 강건 최적설계

Robust Design Optimization of Film Cooling Hole Array for High Pressure Turbine Nozzle

지도교수 이 관 중

이 논문을 공학박사 학위논문으로 제출함

2016 년 2 월

서울대학교 대학원

기계항공공학부

이 상 아

이상아의 공학박사 학위논문을 인준함

2016 년 12 월

위 원 장 : 金奎弘

부위원장 : 李管中

위 원 : 鄭信圭

위 원 : 黃元泰

위 원 : 李同鎬

Abstract

Robust Design Optimization of Film Cooling Hole Array for High Pressure Turbine Nozzle

Sanga Lee
School of Mechanical and Aerospace Engineering
The Graduate School
Seoul National University

Film hole array optimization has been started and considered recently, despite its various difficulties. With its early stage attention in the research field, there are many issues that should be addressed. One of the significant issues in film hole array optimization is the existence of uncertainty in a high-pressure turbine. Film holes in the 1st stage turbine nozzle work under high uncertainty conditions, the main source of which arises from the manufacturing tolerance and varying flow conditions of the turbine inlet and cooling system. Without consideration of these factors, the optimization results can be ineffective or cause critical failure of the mission if there is any difference between the operating and design condition.

In this study, three separate robust design optimization studies for a film cooling hole array are performed under consideration of manufacturing and operational

uncertainties. To determine the design variables, the film hole array is parameterized by using newly suggested shape functions with five design variables. The Efficient Design Optimization method coupled with the Kriging model and Monte Carlo simulation, as well as the Genetic Algorithm are used as robust design optimization methods. The manufacturing tolerance and blowing ratio variance of a film hole and the turbine inlet temperature profile are considered as an uncertainty and probabilistic density function, and the variation range of these uncertainties are quantified referring to the open literature by several random variables

Thus, film hole arrays showing high cooling performance and high robustness to the uncertainties are successfully obtained; sequentially, the results are compared with each other to derive the following conclusions. Manufacturing tolerance is the most influential followed by variation of the blowing ratio, while the variation of the turbine inlet temperature profile hardly affects the film cooling performance. The region whose temperature fluctuates the most on the nozzle surface appears differently according to the uncertainties, but the random variables related to the holes near the leading edge of the nozzle have a larger impact on the cooling performance than the others regardless of the type of uncertainty.

Key words: High Pressure Turbine, Film Cooling, Film Hole Array, Robust Design Optimization, Manufacturing Tolerance, Uncertainty in Cooling System, Blowing ratio, Turbine Inlet Temperature

Student Number: 2012-30182

Table of Contents

Nomenclature

English symbols

A_{PS}	area of the nozzle pressure side surface
$B(\cdot)$	beta function
c_p	specific heat capacity at constant pressure
c_v	specific heat capacity at constant volume
C_x	turbine nozzle axial chord
D	film hole diameter
$d(\cdot)$	distance function
E	expectation
$E[I(\cdot)]$	expected improvement
$f_x(\cdot)$	probability density function
$F_x(\cdot)$	cumulative density function
h	enthalpy
k	turbulent kinetic energy
L	film hole length
M	blowing ratio
$\dot{m}$	mass flow rate
m	number of children in genetic algorithm
P	film hole pitch
P	pattern factor
p	pressure
p	probability
R	gas coefficient
$\boldsymbol{R}$	correlation matrix
R_{ij}	Reynolds stress tensor
R_ic	curvature of the array variable for the shape function

$R_i g$	gradient of the array variable for the shape function
$R_i s$	spacing variable for the shape function
$R_i x$	chordwise location variable for the shape function
$R_i y$	spanwise location variable for the shape function
r	expansion ratio of the hole distance
$r_{\max}$	bais factor
S	Sutherland constant
s	root mean squared error of the predictor for the Kriging model
T	temperature
t	time
$\boldsymbol{U}$	vector of velocity
$\boldsymbol{u}$	fluctuating velocity component in turbulent flow
X	random variable
$\boldsymbol{x}$	vector denoting the position in the design space for the Kriging model
$y(\cdot)$	unknown function
$Z(\cdot)$	deviation from the constant model

Greek symbols

α_i	manufacturing factor of injection angle
β	constant global model of the Kriging model
β	coefficient of thermal expansion (for the Boussinesq approximation)
ε	turbulence dissipation rate
η	film cooling effectiveness
θ	correlation parameter
λ	thermal conductivity
μ	dynamic viscosity
ρ	density
σ	standard deviation
τ	molecular stress tensor

Φ	standard normal distribution
ϕ	standard normal density

Subscripts

ad	adiabatic
aw	adiabatic wall
avg	average
c	cooling air
c	cross-over
curve	curvature element of the hole location
dev	deviation
grad	gradient element of the hole location
hole	film cooling hole
m	mutation
min	minimum
max	maximum
ref	reference
tot	total
t	turbulent
w	property on the wall
∞	flow condition of main passage

Superscripts

-1	inverse matrix
^	estimated value
—	normalized value

Abbreviations

BR	blowing ratio

CDF	Cumulative Density Function
CFD	Computational Fluid Dynamics
DDO	Deterministic Design Optimization
DOE	Design Of Experiment
EI	Expected Improvement
GA	Genetic Algorithm
HPT	High Pressure Turbine
LHS	Latin Hypercube Sampling
NGV	Nozzle Guide Vane
MCS	Monte Carlo Simulation
MSE	Mean Square Error
MT	manufacturing tolerance
PDF	Probabilistic Density Function
RDO	Robust Design Optimization
SF	Scaling Factor
SST	Shear Stress Transport
TIT	Turbine Inlet Temperature

Acronyms

ANOVA	ANalysis Of Variables
EGO	Efficient Global Optimization
RANS	Reynolds Averaged Navier-Stokes

List of figures

List of tables

Chapter 1. Introduction

1.1 Film cooling technique

Gas turbines are widely used for aircraft propulsion and in land-based power generation; thus, their efficiency and performance extensively affect the environment and industrial benefit. Figure 1.1 plots specific core power production, which can be related to specific thrust, as a function of turbine inlet temperature (TIT). This figure shows that the thermal efficiency and power output of gas turbines increase with increasing TIT, which is clearly one of the key technologies in raising gas turbine engine performance.

Figure 1.2 shows the reason why turbine blades need to be cooled with increasing TIT. To double the engine power in aircraft gas turbines, the TIT should increase from 2500°F to 3500°F using the same amount of cooling air. A future aircraft gas turbine would have a higher TIT with the same amount of hotter cooling air from high-pressure compressor bleed. Therefore, it is obvious that high-temperature material development or highly sophisticated cooling schemes is/are important issues for high-performance, high-power gas turbines for the next century.

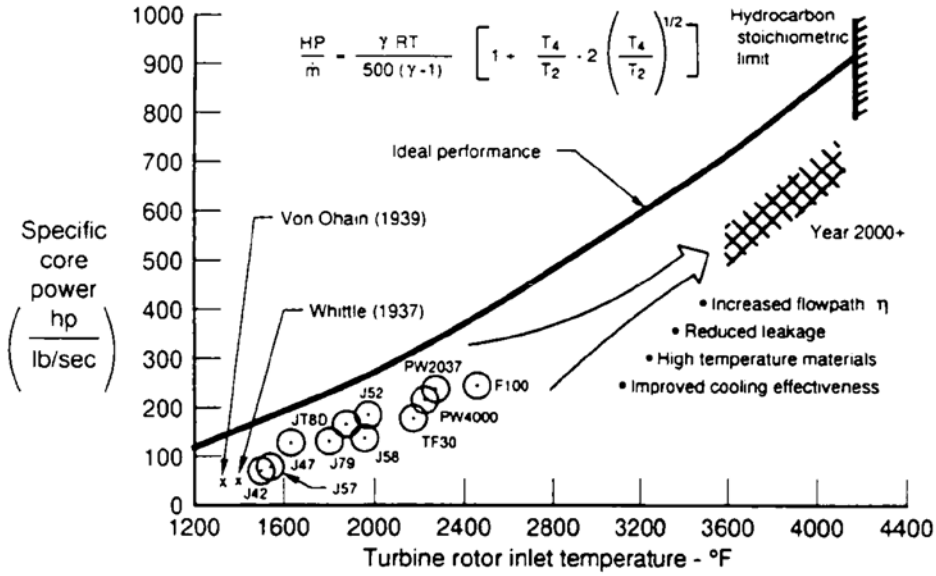

Fig. 1.1 Improvement of cycle power output according to increase of turbine inlet temperature [1]

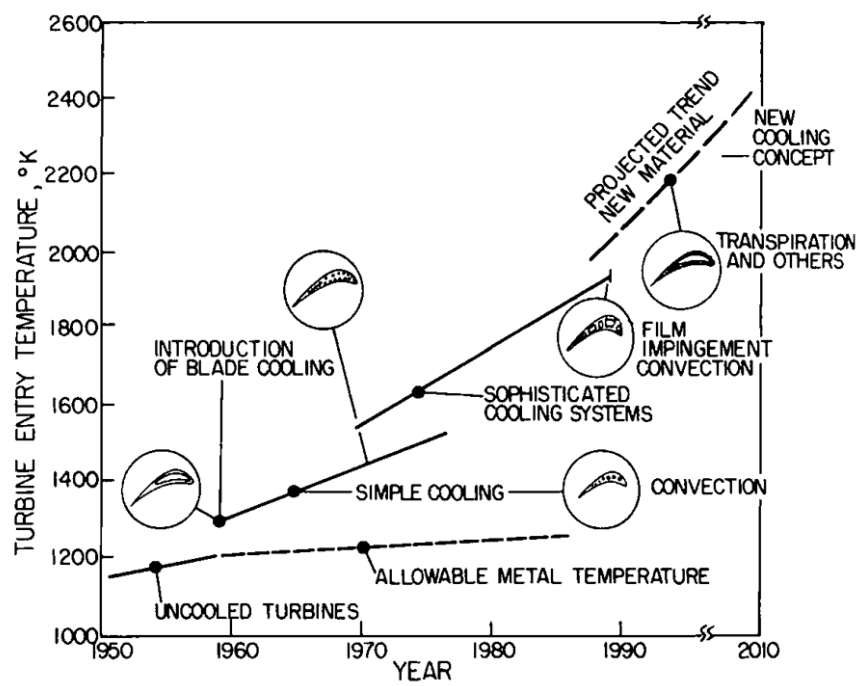

Fig. 1.2 Variation of turbine entry temperature over recent years [2, 3]

There are various techniques for cooling the blade in a turbine both internally and externally. Internal cooling is achieved by passing the cooling air through several serpentine passages inside the blade and extracting the heat from the outside of the blade. Jet impingement, rib turbulator, dimple and pin-fin cooling are also used as methods of internal cooling and support the heat transfer inside the passage.

External cooling, also called film cooling, is one of the cooling techniques that has contributed to the significant increase of turbine inlet temperature. It directly protects the surface by forming a thin layer of cooling air discharged from discrete holes on the wall. [4]

Film cooling performance is mainly affected by the flow properties of cooling air ejected from the holes against those of the gas passing through the main passage. Because it is much easier to shape or relocate the film holes than to change the conditions of either the cooling air or main flow, several studies have been carried out regarding film hole shape and the relative position of the holes to improve the film cooling performance.

- **Research on film cooling hole shape**

The basic idea of shaping the film hole is to mitigate the lifting force of cooling air ejected from the hole, sequentially spreading it more widely on the surface. With a non-shaped, cylindrical hole, cooling air makes a strong pair of vortices, also known as Kidney vortices. These vortices detach the cooling air from the

surface. The method most commonly used to reduce the strength of a Kidney vortex is to expand the exit area of the film hole to diffuse the cooling air as it reaches the surface. The shaped holes adopting this idea are known as fan-shaped holes, whose exit area is expanded in the lateral direction from a certain point, and laid-back holes, whose exit area is forwardly expanded into the surface from a certain point. [5-31]

Over the past decade, the idea has been developed and many interesting shapes of holes have been suggested, including dumbbell- and bean-shaped holes [32], crescent-shaped holes [33], Nekomimi holes [34, 35], sister holes [36-38], and many non-named shaped holes derived from optimization studies. [39, 40] Eventually, Nita et al. [41] employed the Proper Orthogonal Decomposition (POD) method to derive an optimum hole shape with nearly no geometrical constraints and specific design variables.

However, despite the high performance of these holes, they are hardly used in practice, and the shaped holes of early days, such as the fan-shaped hole and laid-back hole, are still widely used. This is mainly because their tricky and delicate shapes are hard to manufacture and easily wear out during operation.

- **Research on positioning of film cooling holes**

Meanwhile, changing the position of the holes has an advantage over modifying film hole shape. With recent stage of studies on hole shapes, achieving performance improvement by modifying the hole shape without any side effect is

assumed to be nearly impossible. Generally, a film hole is manufactured to be as small as possible, as a high manufacturing cost is required to make a delicate modification to one. In contrast, the dimension of hole location is comparably larger than that of hole shape; thus, it does not increase the manufacturing cost by much. The location of holes also has a large impact on film cooling performance because it is not the absolute flow condition of cooling air but the relative flow condition of cooling air to the main flow condition, which is important for the performance of film cooling.

Nevertheless, compared to the research on hole shape itself, the arrangement of film holes on real geometry has been paid little attention thus far. There have been studies of the distance or spacing between holes [42-46], but most of the studies are limited to the relative position of a pair of holes or a combination of two or three holes, with simplified geometry such as a flat plate or converging/diverging nozzle.

The lack of research focused on film hole arrangement on real geometry is mainly observed because numerical simulation of film holes with real geometry is not much easier than an experimental study, not to mention the fact that an experimental study with real geometry is much harder than that with simplified geometry. Simultaneous evaluation of the flow fields around multiple film cooling holes is highly time-consuming, even with the rapid enhancement of computing power. This prevents the role of numerical simulation for rows of film cooling holes away from the optimization study, which requires numerous case evaluations

and actively has been carried out on the film hole shape, remaining as only a supportive tool for experimentation.

Additionally, some of the difficulties come from the fact that there is no known guide to define the location of film holes. To design something systemically, such as by means of an optimization method, it is necessary to define the design variables first. This requirement has brought about the development of useful functions to present the arbitrary shape of a target object, such as PARSEC for airfoil. However, a presentation method for the hole arrangement on real geometry has not yet been suggested.

Nonetheless, several studies have overcome these difficulties, taking real turbine geometry into account. Johnson et al. [47-49] optimized the film cooling hole shape and array pattern on the pressure side of a realistic vane geometry using the genetic algorithm. Film cooling performance was obtained using computational fluid dynamics (CFD) and to reduce the cost, the film holes were replaced by a transpiration boundary and the near wall temperature was taken as an objective function. The optimum array pattern was selected among previously selected candidates.

Most recently, Chi et al. [50] conducted optimization of the film hole arrangement of HPT vanes, also using the genetic algorithm. A 1D heat transfer model was used to obtain film cooling performance, and conditions for the model were obtained from CFD analysis. The position of the holes is defined by two sets of parameters: the representative location of each row of holes and the individual hole location within a row.

1.2 Uncertainties in High Pressure Turbine

Although the aforementioned studies successfully initiated film cooling hole arrangement optimization on real gas turbine geometry, there still remains large room for further improvement in this subject. One of the most significant issues is the existence of uncertainties.

As mentioned before, HPT is highly loaded and exposed to strong temperature and thermal gradients. Within this severe environment, the life of hot components could be affected even by small variations. Much open the literature has reported the significance of uncertainties on HPT, especially those arising from TIT and the cooling system.

- **Uncertainties in Turbine Inlet Temperature**

Montomoli et al. [51] and Salvadori et al. [52] reported that two temperature distributions with identical mean value but different radial shape can have a completely different impact on the rotor lifespan. These results imply that not only mean TIT value but also TIT distribution is important, from the perspective of turbine longevity. However, prediction of the TIT profile is highly challenging work and still has limited accuracy because of the following reasons.

First, the exhausted gas from a combustor chamber has an extremely unsteady nature. Despite a combustor being designed with certain exhausted gas temperature distribution in mind, this temperature distribution is hardly guaranteed to exist in practice. A strong residual swirl from the combustor exit distorts the temperature

distribution, causing the hot streak to migrate. The hot region could also be extended by the secondary flows and its interaction with the passage vortex. For the same reason, the turbulence level of the combustor exit is almost unknown.

Moreover, there is a measurement problem. The most accurate temperature measurements system available for high temperature could give an error of 0.6%, but its operating condition is limited to approximately 1,600 K [53], which means that the sensors for monitoring the engine performance are not placed in the combustor exit but in the first stages of the low pressure turbine. This causes the acquired data to be affected by a high level of uncertainty, to say nothing of the errors arising from calibration drift, degradation of the material, and conduction and radiation errors. The total uncertainty in the measurements could be as high as 2%, which amounts to $\pm$ 30 K at 1500 K. [54]

Recent works have tried to measure the effect of realistic conditions on an HPT cooled vane heat flux, and Salvadori et al. [55] reported that the effects could result in a $\pm$ 20% difference of the heat flux. This leads to the important conclusion that uncertainty in the combustor exit section plays a key role in the evaluation of the residual life of HPT components.

- **Uncertainties in turbine cooling system**

The previously addressed harsh environment generated by a combustor also brings about strong spanwise variations of cooling parameters, e.g., up to $\pm$ 30% for the density ratio and $\pm$ 50% for the blowing ratio. [54] These are critical

parameters determining the film cooling performance, and these values of variation could yield a significant difference from the designed performance. If these parameters are lower than necessary, the cooling air would be dissipated in the early stage, while if they are higher than necessary, the cooling air would be easily lifted off from the surface. In either case, the degradation of cooling performance is inevitable.

Moreover, there is another issue of uncertainty: manufacturing tolerance. Moeckel [56] reported that among all HPT geometrical parameters, the cooling system is the most influential when there is possible geometrical difference from the original design. It becomes even more substantial in regard to the film cooling because it is manufactured to be as small as possible. Bunker [57] investigated the manufacturing factors of a typical blade design and their levels of effects on cooling, including 7 manufacturing factors for film cooling. According to the investigation, 5° for 3 angle factors, 10% for diameter and surface spacing, 7% for the length-to-diameter ratio, and 30% for the shaped exit specification are possible ranges for each manufacturing tolerance. However, these are the most important among the tolerances such that a variation of 10% of hole diameter can reduce the blade life by 33%.

1.3 Motivation and scope of the dissertation

From the review of previous research addressed so far, finding the optimum arrangement of film holes is found to be clearly worth pursuing. However, it is also obvious that the uncertainty in HPT and film cooling is so substantial that without consideration of them, the optimization results could be non-effective or even degrade the performance when applied to actual geometries.

Thus, the present study attempts to improve turbine cooling performance by rearranging the film holes, under consideration of uncertainties. To attain this end, a robust design optimization procedure (RDO) is suggested to take the uncertainties in HPT and film hole into account and is sequentially applied to film holes on the nozzle vane pressure side.

This paper is organized as follows: After the introduction of Chapter 1, fluid and thermal analysis and the RDO method are described in Charter 2. This chapter introduces the CFD method of ANSYS CFX utilized in the study and its modification to address high temperature flow. Additionally, as one of the RDO methods, the Efficient Global Optimization (EGO) method, using the Kriging and Genetic Algorithm (GA), and Monto Carlo Simulation (MCS) are described.

In Chapter 3, grid and boundary conditions for the reference NGV model are set, and then the fully cooled reference model is simplified to reduce the computational cost.

In Chapter 4, deterministic design optimization is performed to determine the validity of the methodology addressed in Chapter 2, except for the probabilistic

assessment part. Through this chapter, arrangement of the film holes is parameterized based on the newly suggested shape functions, which consist of only a few design variables, and the deterministic optimization results are discussed and compared with the experimental study to validate the results.

In Chapter 5, uncertainties which will be employed in the study are introduced. As described above, among many uncertainties in HPT, the most substantial sources of uncertainties—TIT profile, blowing ratio, and manufacturing tolerance for film hole—are chosen. To address these uncertainties in the RDO study, they are presented based on several random variables and quantified using probabilistic distribution functions in this chapter.

In Chapter 6, robust design optimization studies considering 3 uncertainties are performed. The results of RDO considering manufacturing tolerance, RDO considering variance of blowing ratio, and RDO considering TIT distortion are addressed in sequence and, lastly, compared with each other. From the results, some insights into the characteristics of uncertainties and film hole arrangement are derived. Finally, the conclusion is given in Chapter 7.

.

Chapter 2. Numerical approach

2.1 Fluid and thermal analysis

2.1.1 Governing equations

For flow field and thermal analysis, the compressible steady Reynolds averaged Navier-Stokes (RANS) equations employed in ANSYS CFX are used. [58] The governing equations are presented as eqs. (2.1) ~ (2.3).

$$\frac{\partial \rho}{\partial t} + \frac{\partial}{\partial x_j}\left(\rho U_j\right) = 0 \tag{2.1}$$

$$\frac{\partial \rho U_i}{\partial t} + \frac{\partial}{\partial x_j}\left(\rho U_i U_j\right) = -\frac{\partial p}{\partial x_i} + \frac{\partial}{\partial x_j}\left(\tau_{ij} - \rho\overline{u_i u_j}\right) \tag{2.2}$$

$$\frac{\partial \rho h_{tot}}{\partial t} - \frac{\partial p}{\partial t} + \frac{\partial}{\partial x_j}\left(\rho U_j h_{tot}\right) = \frac{\partial}{\partial x_i}\left(\lambda \frac{\partial T}{\partial x_i} - \rho\overline{u_j h}\right) + \frac{\partial}{\partial x_j}\left[U_i\left(\tau_{ij} - \rho\overline{u_i u_j}\right)\right] \tag{2.3}$$

where τ is the molecular stress tensor and h_{tot} is the mean total enthalpy, given by

$$h_{tot} = h + \frac{1}{2}U_i U_i + k \tag{2.4}$$

k is turbulent kinetic energy:

$$k = \frac{1}{2}\overline{u_i^2} \tag{2.5}$$

The flow is regarded as fully turbulent because the optimization target of this study is film holes at the nozzle pressure side surface on which flow transits to turbulence almost immediately after the flow reaches the nozzle and is relaminarized. The heat transfer level and pressure coefficient of the nozzle pressure side surface hardly change compared to those on the suction side, whose transition point is at the middle of the blade.

2.1.2 Turbulent modeling

In eq. (2.3), there is an unknown term including the Reynolds stress tensor:

$$R_{ij} \equiv -\rho\overline{u_i u_j} \tag{2.6}$$

For turbulence closure, the k-ω-based shear stress transport (SST) model was used. It is a two-equation eddy viscosity turbulence model that utilizes the original k-ω model of Wilcox inside the boundary layer and switches to the standard k-ε model in the freestream. The model, developed by Menter [59, 60], has been shown to perform well in flows with adverse pressure gradients and a separated flow region. [61]

The eddy viscosity hypothesis assumes that the Reynolds stresses can be related to the mean velocity gradients and eddy (turbulent) viscosity by the gradient diffusion hypothesis, in a manner analogous to the relationship between the stress and strain tensors in laminar Newtonian flow:

$$-\rho\overline{u_i u_j} = \mu_t\left(\frac{\partial U_i}{\partial x_j}+\frac{\partial U_j}{\partial x_i}\right)-\frac{2}{3}\delta_{ij}\left(\rho k+\mu_t\frac{\partial U_k}{\partial x_k}\right) \tag{2.7}$$

where μ_t is the eddy viscosity or turbulent viscosity, which must be modeled.

To blend the k-ε model with the k-ω model, the k-ε model is transformed to k-ω formulation by multiplying by $(1-F_1)$ and then added to the k-ω model, which is multiplied by F_1. The resulting transport equations for the SST model are

$$\frac{\partial(\rho k)}{\partial t}+\frac{\partial}{\partial x_j}(\rho U_j k)=\frac{\partial}{\partial x_j}\left[\left(\mu+\frac{\mu_t}{\sigma_k}\right)\frac{\partial k}{\partial x_j}\right]+P_k-\beta'\rho k\omega \tag{2.8}$$

$$\frac{\partial(\rho\omega)}{\partial t}+\frac{\partial}{\partial x_j}(\rho U_j \omega)=$$

$$=\frac{\partial}{\partial x_j}\left[\left(\mu+\frac{\mu_t}{\sigma_\omega}\right)\frac{\partial \omega}{\partial x_j}\right]+(1-F_1)2\rho\frac{1}{\sigma_\omega\omega}\frac{\partial k}{\partial x_j}\frac{\partial \omega}{\partial x_j}+\alpha\frac{\omega}{k}P_k-\beta\rho\omega^2 \tag{2.9}$$

The eddy viscosity μ_t is obtained from eq. (2.10)

$$\mu_t=\frac{a_1\rho k}{\max(a_1\omega, SF_2)} \tag{2.10}$$

Here, S is strain-rate tensor. Additionally, blending functions F_1 and F_2 are defined as eqs. (2.11) ~ (2.12)

$$F_1 = \tanh(\arg_1^4) \tag{2.11}$$

$$\text{with:} \quad \arg_1 = \min\left(\max\left(\frac{\sqrt{k}}{\beta' \omega y}, \frac{500\nu}{y^2 \omega} \right), \frac{4\rho k}{CD_{kw} \sigma_{w2} y^2} \right)$$

$$CD_{kw} = \max\left(2\rho \frac{1}{\sigma_{\omega 2} \omega} \frac{\partial \omega}{\partial x_j}, 1.0 \times 10^{-10} \right)$$

$$F_1 = \tanh(\arg_2^4) \tag{2.12}$$

$$\text{with:} \quad \arg_2 = \max\left(\frac{2\sqrt{k}}{\beta' \omega y}, \frac{500\nu}{y^2 \omega} \right)$$

The coefficients of the SST turbulence model, α, β, σ_k, and σ_ω, are also obtained by blending the coefficients of the k-ω model, denoted as ϕ_1, with those of the transformed k-ε model (ϕ_2).

$$\phi = F_1 \phi_1 + (1 - F_1) \phi_2 \tag{2.13}$$

Constant values for each model can be found in Ref. [62].

2.1.3 Treatment of wall

ANSYS CFX provides an automatic near-wall treatment option for ω-based models. This option switches automatically from wall functions to a low-Reynolds

near-wall formulation as the mesh is refined. It requires a finer mesh near the wall, hence placing many grid points inside the viscous sub-layer. This formulation is recommended for simulations requiring accurate boundary layer calculations, such as heat transfer predictions. In k-ω turbulence models, the wall boundary conditions for the k-equation are accounted for using the automatic near-wall-treatment option. [61]

2.1.4 Heat transfer calculation

As a working fluid, ideal air is used. Because the operating temperature of HPT is extremely high, dynamic viscosity, heat capacity, and thermal conductivity are not constant but vary with the flow temperature. CFX provides a kinetic theory named the modified Eucken model [63] to calculate thermal conductivity in eq. (2.3), and it enables thermal conductivity to be obtained using dynamic viscosity and heat capacity, as presented in eq. (2.14).

$$\frac{\lambda}{\mu c_v} = 1.32 + 1.77\frac{R}{c_v} \tag{2.14}$$

To use this formulation, a 4th-order zero pressure polynomial for specific heat (c_p/R) is formulated as a function of temperature, using tabulated data. The polynomial is presented as eq. (2.15), whose R square value for the data [64] is 0.9999.

$$\frac{c_p}{R} = 3.5388 - 6.7762\times10^{-04}T + 2.2695\times10^{-06}T^2 - 1.4414\times10^{-09}T^3 + 2.9195\times10^{-13}T^4 \quad (2.15)$$

Additionally, the dynamic viscosity is obtained from the Sutherland formula as eq. (2.16)

$$\frac{\mu}{\mu_0} = \frac{T_{ref} + S}{T + S}\left(\frac{T}{T_{ref}}\right)^n \quad (2.16)$$

The reference molecular viscosity μ_0 is set to 1.716×10^{-5} Pa·S and the Sutherland constant S is set to 110.4 K. The reference temperature T_{ref} and the temperature exponent n are set to 273.15 K and 1.5, respectively.

Figure 2.1 shows the results of comparison between the thermal conductivity obtained by solving eqs. (2.14) ~ (2.16) and the data from the work of Kadoya et al. [65] Although a certain degree of difference between the two values is observed near a high temperature of approximately 2,000 K, it is confirmed that they match well in most of the regions of interest in this study.

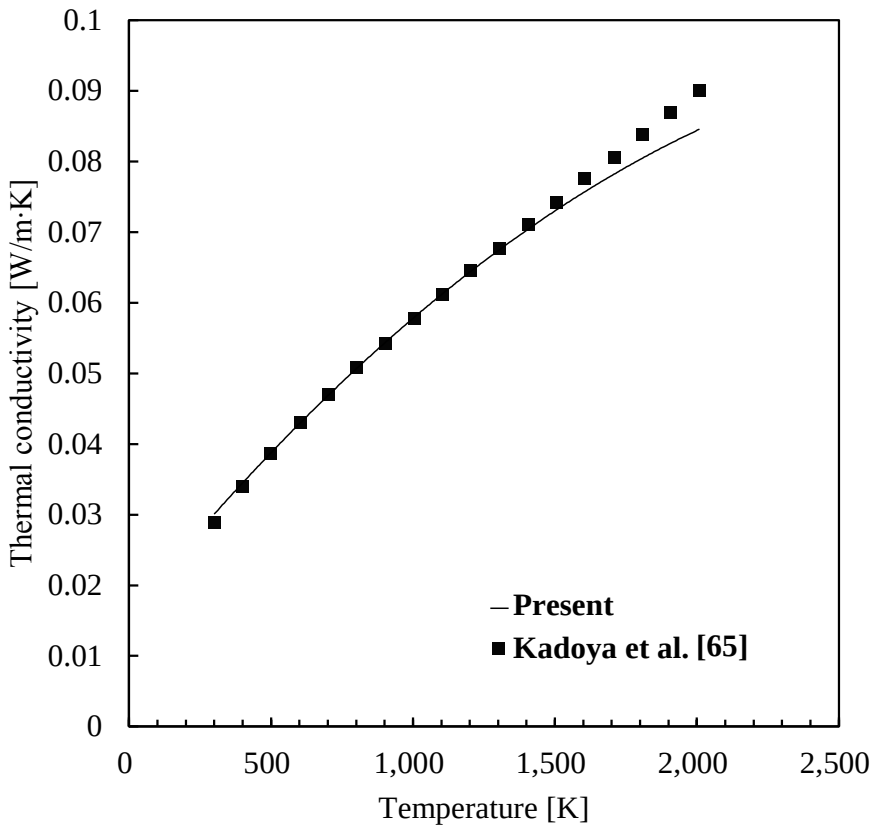

Fig. 2.1 Comparison of thermal conductivity

2.2 Design Optimization method

2.2.1 Kriging model

Because GAs or Monte Carlo Simulation (MCS) requires tens of thousands of function evaluations, it is impossible to directly apply GAs or MCS to problems that require high computational loads for the function evaluation, such as CFD. To address this issue, surrogate models have been adopted in most optimization problems using CFD to substitute for the direct function evaluation. In this study, the Kriging model is used as a surrogate model. The Kriging model is one of the interpolation models that has a reputation for good predictability of non-linear response. [66, 67] A Kriging model is presented as the sum of the global model and the localized deviation given by eq. (2.17).

$$y(\boldsymbol{x}) = \beta + Z(\boldsymbol{x}) \tag{2.17}$$

$\boldsymbol{x}$ is an m-dimensional vector, m is the number of variables, β is a global model, and $Z(\boldsymbol{x})$ is the local deviation of the global model. In numerous cases, β is constant and $Z(\boldsymbol{x})$ is derived from the correlation function and the correlation parameter. The correlation function is a function of the distances between the sampling points; the correlation parameter can be acquired via maximum likelihood estimation. Even when the same sampling points are used, the Kriging model could be different, depending on the type of correlation function. In this study, the Kriging model of

Jeong et al. [68] is adopted, which uses the Gaussian function as a correlation function.

In the model, the local deviation at an unknown point, $\boldsymbol{x}$, is expressed using stochastic processes. The sample points are interpolated with the correlation function to estimate the trend of the stochastic processes. The correlation between $Z(\boldsymbol{x}^i)$ and $Z(\boldsymbol{x}^j)$ is strongly related to the distance between the two corresponding points, i.e., $\boldsymbol{x}^i$ and $\boldsymbol{x}^j$. In the Kriging model, a special weighted distance is used instead of the Euclidean distance, as follows:

$$d(\boldsymbol{x}^i, \boldsymbol{x}^j) = \sum_{k=1}^{m} \theta_k \left| x_k^i - x_k^j \right|^2 \tag{2.18}$$

where θ_k ($0 \le \theta_k \le \infty$) is the k-th element of the correlation vector parameter θ. By using the specially weighted distance and the Gaussian random function, the correlation between the point $\boldsymbol{x}^i$ and $\boldsymbol{x}^j$ is defined as

$$corr\left[Z(\boldsymbol{x}^i), Z\left(\boldsymbol{x}^j\right) \right] = \exp\left[- d(\boldsymbol{x}^i, \boldsymbol{x}^j) \right] \tag{2.19}$$

The Kriging predictor, i.e., a function estimated by the Kriging model, can be expressed as

$$\hat{y}(\boldsymbol{x}) = \hat{\beta} + \boldsymbol{r}'\boldsymbol{R}^{-1}(\boldsymbol{y} - \boldsymbol{1}\hat{\beta}) \tag{2.20}$$

where $\hat{\beta}$ is the estimated value of β; R denotes the matrix whose (*i, j*) entry is $corr\left[Z(\boldsymbol{x}^i), Z(\boldsymbol{x}^j)\right]$. The i-th element of vector ***r*** is

$$r_i(\boldsymbol{x}) \equiv corr\left[Z(\boldsymbol{x}), Z(\boldsymbol{x}^i)\right] \tag{2.21}$$

and $\boldsymbol{y} = [y(x^1), ..., y(x^n)]$. The unknown parameter to be estimated for constructing the Kriging model is θ. This parameter can be estimated by maximizing the following likelihood function.

$$Ln(\hat{\beta}, \hat{\sigma}^2, \boldsymbol{\theta}) = -\frac{n}{2}\ln(2\pi) - \frac{1}{2}\ln\left(|\boldsymbol{R}|\right) - \frac{n}{2}\ln(\hat{\sigma}^2) - \frac{1}{2\hat{\sigma}^2}\left(\boldsymbol{y} - \boldsymbol{1}\hat{\beta}\right)' \boldsymbol{R}^{-1}\left(\boldsymbol{y} - \boldsymbol{1}\hat{\beta}\right) \tag{2.22}$$

where ***1*** denotes an m-dimensional unit vector. Maximizing the likelihood function is an m-dimensional unconstrained non-linear optimization problem. In this paper, GAs are adapted to solve the present problem.

2.2.2 Efficient design optimization method

Selecting adequate experimental points plays a major role in constructing an accurate and reliable surrogate model. The initial experimental points could be selected using Design of Experiment (DOE). [69] Latin Hypercube Sampling (LHS) is one of the space filling concept DOE methods; LHS selects evenly distributed points in the design space. [70]

Although the accuracy of the surrogate model improves when the sampling points fill the design space more evenly, it is inefficient to select additional experimental points over the entire design space because the region of interest of most studies is only the region near the optimum points. Therefore, to efficiently improve the accuracy of the Kriging model, a repeated process of updating the DOE set in the vicinity of the optimum points is used. Here, the Efficient Global Optimization (EGO) method determines the next sampling point efficiently via the stochastic process based on the previous optimization results. [71] In this study, the Expected Improvement (EI) given by eq. (2.23) suggested by Schonlau [72] is used as a criteria for selecting additional sampling points.

$$E[I(\boldsymbol{x})] = (f_{\min} - \hat{\boldsymbol{y}})\Phi\left(\frac{f_{\min} - \hat{\boldsymbol{y}}}{s}\right) + s\phi\left(\frac{f_{\min} - \hat{\boldsymbol{y}}}{s}\right) \tag{2.23}$$

Φ and ϕ refer to the probability density function (PDF) and the cumulative density function (CDF) of a standard normal distribution, respectively. The first term has a high value in the region where the fitness is high, while the second term has a high value in the region where the uncertainty is high. In other words, the accuracy near the optimum and the accuracy of the entire Kriging model are improved simultaneously by selecting the high EI points as additional sampling points.

Meanwhile, there are cases that are not able to locate the region of interest. In these cases, EI is inappropriate as an EGO criteria. Robust design optimization

(RDO), performed in this study, is one of these cases. This is because in the RDO problem, not only nominal value but also statistic momentums of the design point, such as the mean or variation, are of interest. These values cannot be obtained using the Kriging model alone but can only be obtained via probabilistic assessment of the model. Therefore, instead of EI, mean square error (MSE) of the Kriging model is used as an EGO criteria for the RDO problem. MSE can be obtained by using eq. (2.24)

$$s^2(x) = \hat{\sigma}^2\left[1 - \mathbf{r}'\mathbf{R}^{-1}\mathbf{r} + \frac{(1 - \mathbf{1}\mathbf{R}^{-1}\mathbf{r})^2}{\mathbf{1}`\mathbf{R}^{-1}\mathbf{1}}\right] \tag{2.24}$$

MSE, also used when calculating the EI value in eq. (2.23), indicates the uncertainty at the estimation point. It means that selecting MSE as a criterion for an additional sample yields improvement of the reliability of the entire design space.

Once the initial Kriging model is constructed, GA is performed to determine the points having high EI or MSE of the objectives. Then, three points among the solutions are selected as additional sampling points and the DOE set is updated to include those points. [68, 73] After this step, two different strategies are employed for each deterministic design optimization (DDO) and RDO problem.

For the case of the DDO problem, the Kriging model is assumed to converge if the EGO fails to find the enhanced value of the objectives five times in a row. The searching process for optimum points is performed using this converged Kriging model.

For the case of the RDO problem, the Kriging model is assumed to converge if the average error of additional sampling points is less than 3%. This means that the maximum error of the Kriging model is not much larger than 3%. This converged Kriging model is used for probabilistic assessment.

2.2.3 Monte Carlo simulation

For probabilistic assessment, MCS is used. MCS produces a probability distribution of events by using lots of repeated processes with random sampling, of which a possible value is determined using the prescribed probabilistic density function (PDF).

For a given random variable X, the probability that X will take on a value X is defined by the probability density function:

$$f_X(x) = \Pr[X = x] \tag{2.25}$$

where $f_X(x) \geq 0$ for all x. The probability that the random variable X will take on a value less than a specified threshold value x is defined by the distribution function for that random variable, often also termed the cumulative distribution function:

$$F_X(x) = \Pr[X \leq x] \tag{2.26}$$

where $0 \le f_X(x) \le 1$ for all *x*. For a continuous random variable *X*, the probability density function, $f_X(x)$, and cumulative distribution function, $F_X(x)$, are related as follows:

$$F_X(x) = \int_{-\infty}^{x} f(t)dt \tag{2.27}$$

$$f_X(x) = \frac{d(F_X(x))}{dx} \tag{2.28}$$

The probability density and cumulative distribution functions for a given probability distribution are generally defined as a function of one or more distribution parameters that define the location, shape, or dispersion of the distribution. In this study, Gaussian distribution, Normal distribution, and Gumbel distribution are used as the PDF for input variables.

The normal distribution is the "bell curve" distribution most commonly used to describe the nature phenomena. This distribution is a two-parameter distribution defined in terms of the mean μ and standard deviation σ of the random variable *X*, as in eq. (2.29)

$$f_X(x) = \frac{1}{\sigma\sqrt{2\pi}} \exp\left[\frac{-(x-\mu)^2}{2\sigma^2}\right], \quad -\infty \le x \le \infty \tag{2.29}$$

The Gumbel distribution is also known as an extreme value distribution, often used to describe the breaking strength of materials, breakdown voltage in

capacitors, and gust velocities encountered by an aircraft. The Gumbel PDF for the largest element is presented as eq. (2.30)

$$f_X(x) = \beta \exp[-\beta(x-\alpha) - \exp[-\beta(x-\alpha)]], \quad -\infty \le x \le \infty, \quad \beta > 0 \tag{2.30}$$

The Gumbel PDF for the smallest element is presented as eq. (2.31)

$$f_X(x) = \beta \exp[\beta(x-\alpha) - \exp[\beta(x-\alpha)]], \quad -\infty \le x \le \infty, \quad \beta > 0 \tag{2.31}$$

Although the surrogate model is used to reduce the computational burden, it is still computationally intensive to carry out MCS with random sampling. Therefore, the descriptive sampling technique is introduced for MCS. The descriptive sampling technique generates sample points by dividing each random variable distribution into *n* intervals of equal probability and randomly combining samples from these intervals for each random variable to produce design points. [74]

2.2.4 Genetic algorithm

Genetic algorithms (GAs) are the most popular type of evolutionary algorithm and have been successfully used as an optimization technique to resolve practical engineering problems. The search technique employed by GAs is based on the mechanisms of natural evolution and selection. The search starts from an initial

ensemble of solutions, also called chromosomes or individuals that are randomly selected from the design space. [75, 76]

The main steps of a GA are [77]:

- Initialize a population of m individuals $\mathbf{x_1}^{(1)},...,\mathbf{x_m}^{(1)}$ on the discretized design space and evaluate the fitness function for each individual in the population.
- At generation *n*, repeat the following steps for creating a couple of offspring up to when *m* children $\mathbf{x_1}^{(n+1)},...,\mathbf{x_m}^{(n+1)}$ have been generated,
  - Select a pair of parents,
  - Apply the cross-over operator with probability p_c, giving birth to two children. If no cross-over takes place, the two offspring are exact copies of their parents. The cross-over probability is generally quite high (P_c~0.90)
  - Apply the mutation operator to each allele of the two offspring with probability p_m. The mutation probability is generally quite low (p_m~0.01) since it is applied to every allele and not to the whole individual and since the aim of GAs is to use cross-over more than mutation as the main responsible of the evolution,
- The new population replaces completely the previous one and the fitness of their individuals is evaluated, if *m* is odd one children is discarded at

random, no survival of the fittest applies unless and elitism operator is adopted.

Apart from the initialization, the steps are repeated until the termination criteria are met. The procedures of the DDO and RDO problem are shown in Fig. 2.2 and Fig. 2.3, respectively.

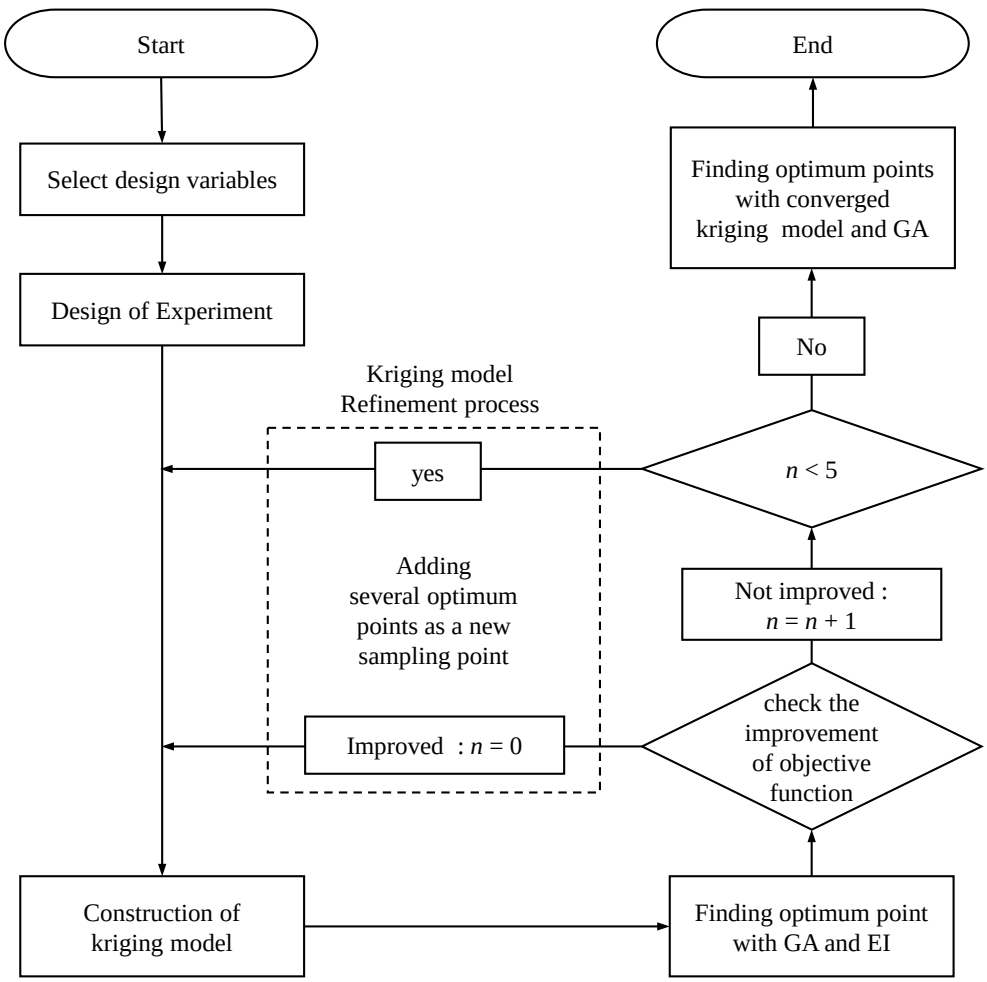

Fig. 2.2 Deterministic design optimization flow chart

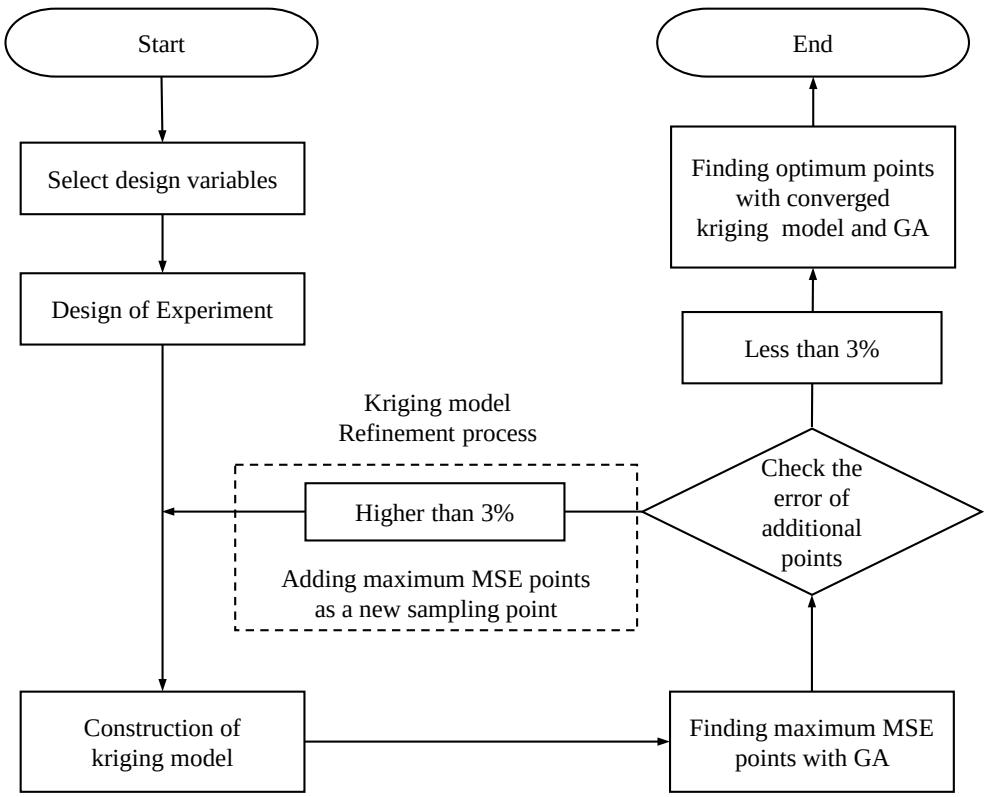

Fig. 2.3 Robust design optimization flow chart

Chapter 3. Reference model

3.1 Aerodynamic design of the nozzle

The target turbine nozzle is designed for the 1st stage HPT of a 10,000 lbf-class aircraft gas turbine engine. The mean radius of the turbine is 275 mm, the number of nozzles is 56, and the average span length of each nozzle is approximately 20 mm. The true and axial chord length of the nozzle are 41 mm and 23 mm, respectively, and the flow inlet and exit angle are zero and 74°, respectively. The inlet and outlet Reynolds numbers, based on the true chord length, are approximately 3.9×10^5 and 2.1×10^6, respectively. Figure 3.1 shows the aerodynamic geometry of the 1st-stage turbine, including the rotors. The detailed design procedure and specification of the turbine are summarized in Rhee et al. [78] and Kang et al. [79]

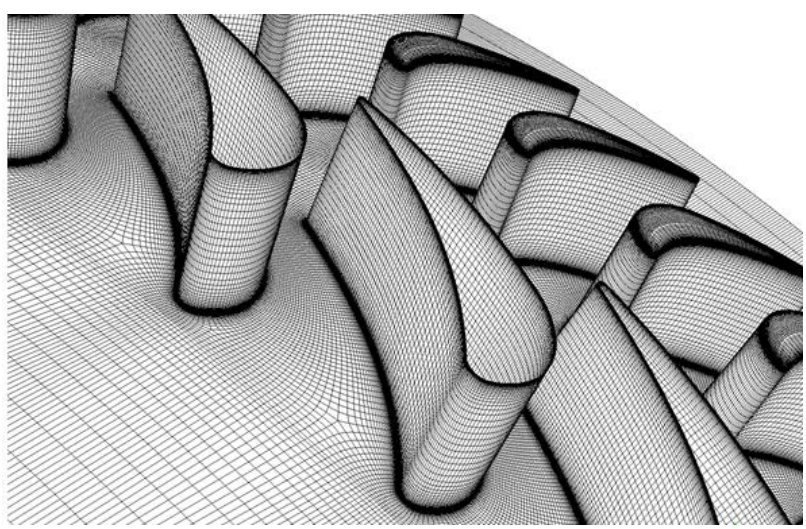

Fig. 3.1 The 1st stage HPT aerodynamic design

3.2 Cooling design of the nozzle

There are two main cooling passages for the nozzle cooling, as shown in Fig. 3.2. P#1 is located near the leading edge, while P#2 is located at the center of the airfoil. Inside P#1, pedestals are installed on the leading-edge sidewall to promote the mixing of cooling air. Parts of supplied cooling air are discharged through the six rows of film cooling holes and cool the entire nozzle surface. Inside P#2, rib turbulators are installed on the pressure sidewall to enhance the heat transfer. Parts of the induced cooling air go outside through the two rows of film cooling holes for the pressure side cooling or pass through the impingement holes and cool the suction sidewall. The air passing the impingement holes goes through the trailing edge pedestals and is sequentially discharged from the slots at the trailing edge.

The optimization target of this study is the arrays of film cooling holes on the pressure side. From the leading edge, the arrays are denoted as ROW0, ROW1 and ROW2 sequentially, and the “pressure side” is defined from ROW0 to the trailing edge in this study. The number of holes is 11, 10, and 9 for ROW0, ROW1, and ROW2, respectively.

All the film cooling holes have the same shape, as shown in Fig. 3.3, but different injection angles. The injection angle of ROW0 is 34°, whereas that of the others is 30° with respect to the nozzle surface. The diffusion angle is 10° in the spanwise direction, and the diffusion location is at the 1/3 point of the hole length from the hole inlet.

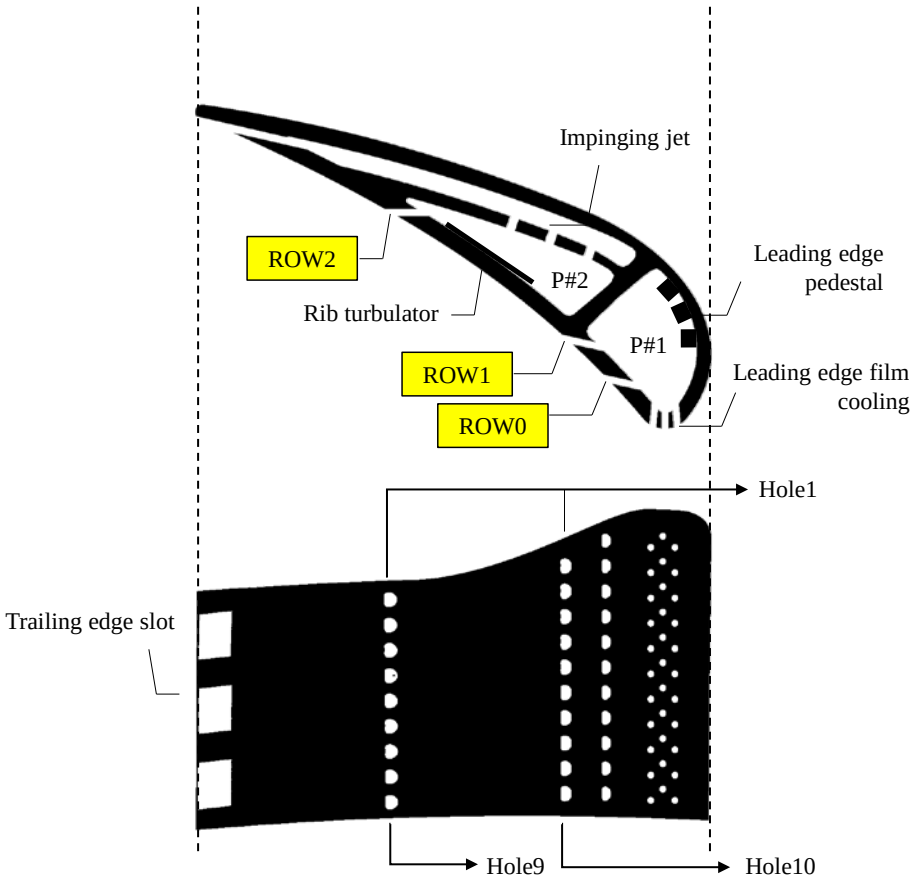

Fig. 3.2 Description of cooling design for the nozzle

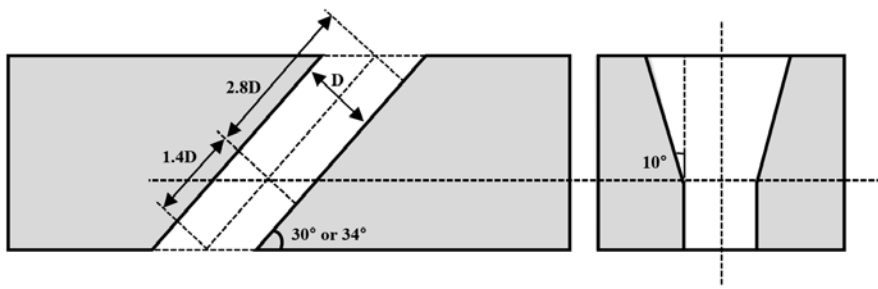

Fig. 3.3 Description of the film cooling hole geometry

Film holes are aligned in a straight line. Axial positions of each row are $0.15C_x$, $0.28C_x$, and $0.67C_x$ for ROW0, ROW1 and ROW2, respectively. Holes have uniform distance of 3.6D, where D denotes a hole diameter, which is 0.5 mm.

3.2.1 Grid and boundary conditions

Figure 3.4 depicts the computational domain for the cooled nozzle, the boundary conditions, and the generated grids. The total pressure and total temperature at the nozzle and cooling passage inlet, evaluated through the cycle analysis, are given, and the static pressure for the outlets is specified. Conduction effects are not considered in this study; thus, the nozzle surface is treated as an adiabatic wall. The numerical domain includes a single passage of the HPT with a periodic boundary condition, and the total number of grid elements is approximately 25 million.

The turbine inlet temperature has a parabolic profile, with an average temperature of 1,673 K and maximum temperature of 1,830 K. The turbulent intensity is set to 5%. The other boundary conditions are listed in Table 3.1.

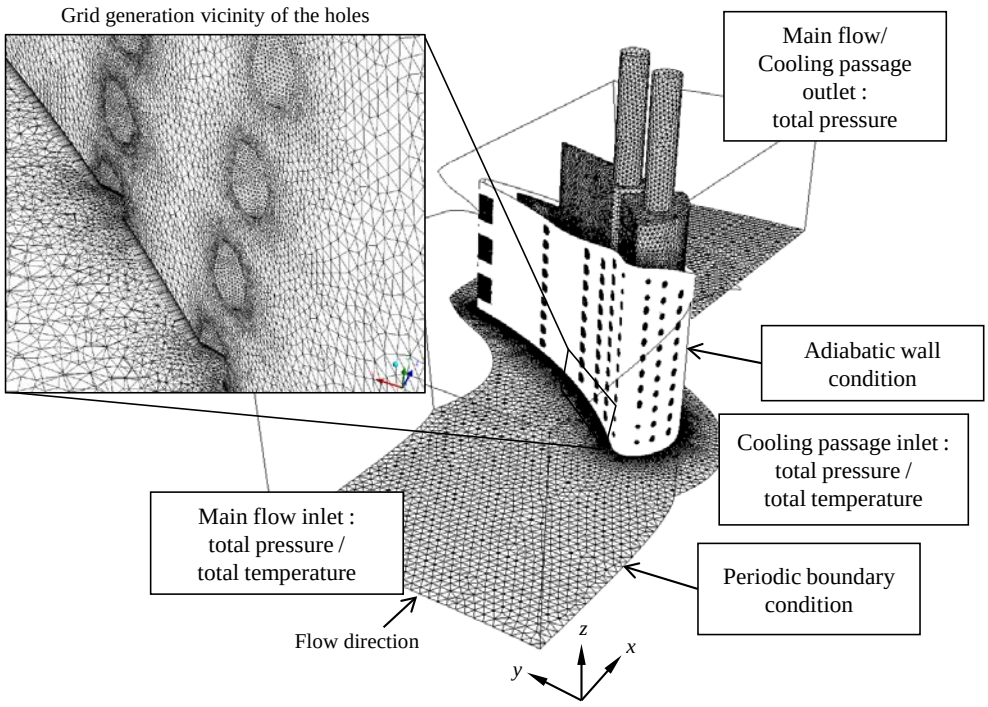

Fig. 3.4 Grid generation and boundary conditions for the nozzle with original cooling design

Table 3.1 Boundary conditions

Location	Conditions	Value
Main passage inlet	Total pressure	30.685 bar
	Average total temperature	1,673 K
Main passage outlet	Static pressure	15.650 bar
Cooling passage inlet	Total pressure	32 bar
	Total temperature	837 K
Cooling passage outlet	Total pressure	31.9 bar

3.3 Simplified cooled nozzle

Because many function evaluations are required during the optimization process, reducing the elapsed time for function evaluations is essential for design affordability. The simplest way to shorten the elapsed time is to reduce the number of grid elements. The computational domain for the reference cooled nozzle consists of 25 million grid elements, but it can be reduced by a substantial amount if the configuration of the nozzle is simplified. The simplified cooled nozzle is modeled by eliminating the internal cooling components and the suction side/leading edge film cooling holes from the nozzle with the original design.

The blowing ratio defined in eq. (3.1) is one of the dominant factors that determine the film cooling performance.

$$M = \frac{\rho_c U_c}{\rho_\infty U_\infty} \tag{3.1}$$

If the blowing ratio of the simplified cooled nozzle is equivalent to that of the fully cooled nozzle, then it can be assumed that the film cooling holes of the simplified cooled nozzle have an equivalent performance to those of the reference cooled nozzle. From eq. (3.1), the mass flow rate of the cooling air of both models should be identical to ensure that these nozzles have equivalent blowing ratio because the shapes of the film cooling holes of both models are identical.

3.3.1 Grid and boundary conditions

The cooling air of the reference cooled nozzle is induced by the pressure difference between the inlet and outlet of the cooling passages. However, it is not appropriate to apply the same boundary conditions to the cooling passages of the simplified cooled nozzle because the internal cooling components that cause the total pressure loss of the cooling air are eliminated. Therefore, instead of the total pressure boundary condition, the mass flow rate boundary conditions, presented as eq. (3.2) ~ (3.3), are applied to the inlet and outlet of the cooling passages of the simplified cooled nozzle.

$$\dot{m}_{in\_simple} = \dot{m}_{in\_ref} \tag{3.2}$$

$$\dot{m}_{out\_simple} = \dot{m}_{in\_ref} - \dot{m}_{PS\_holes\_ref} \tag{3.3}$$

The induced total mass flow rate of the cooling air is applied as an inlet boundary condition, while the sum of the mass flow rates of the cooling air ejected from the pressure side film cooling holes subtracted from the induced total mass flow rate is applied as an outlet boundary condition. These values of the mass flow rate of the cooling air are obtained from the analysis results of the nozzle with the original cooling design. Figure 3.5 shows the grid and boundary conditions of the simplified cooled nozzle. The number of grid elements is reduced from 25 million to 8 million.

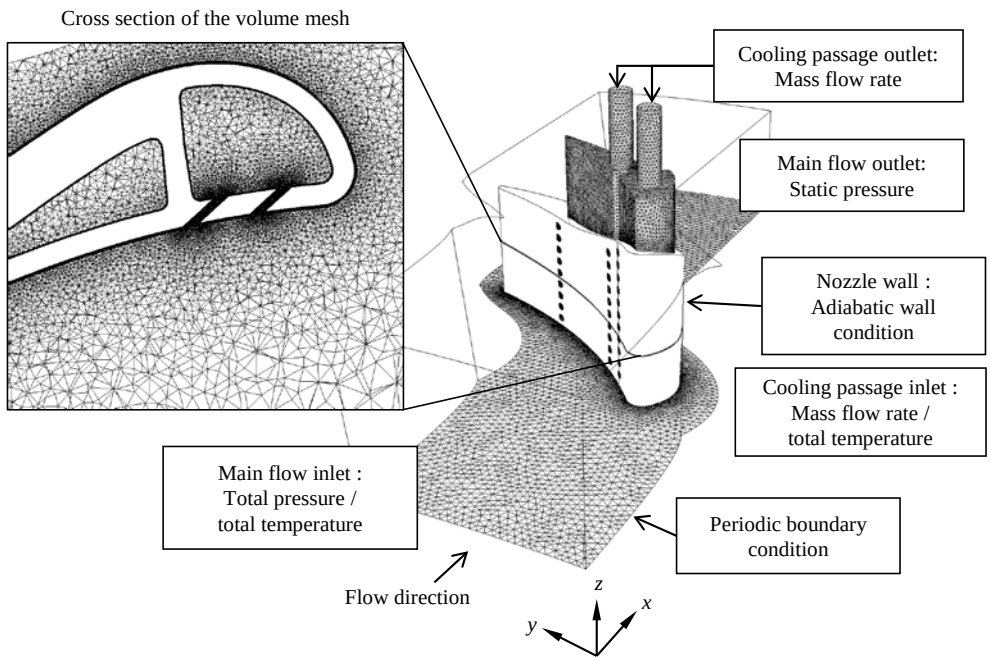

Fig. 3.5 Computational domain and boundary conditions for simplified cooled nozzle

3.4 Comparison of the results

To validate this approach, the blowing ratios of the fully cooled nozzle and the simplified cooled nozzle are compared; the results are shown in Fig. 3.6. The differences between the blowing ratios of the two models are within 5%. The hub side holes under the 6th hole show relatively large differences, but that much value does not substantially affect the film cooling performance. This is confirmed in Fig. 3.7, which shows the laterally averaged film cooling effectiveness at the normalized chordwise position to the axial chord length. The adiabatic film cooling effectiveness can be obtained from eq. (3.4).

$$\eta_{ad} = \frac{T_{aw} - T_{\infty}}{T_c - T_{\infty}} \tag{3.4}$$

T_{∞} is the temperature of the external flow, T_{aw} is adiabatic wall temperature, and T_c is the temperature of the cooling air. Because the turbine has a parabolic inlet temperature profile and is operated in transonic condition, it is difficult to determine the bulk temperature for T_{aw}. Thus, the adiabatic local surface temperature obtained from the analysis results of the nozzle without cooling is used as T_{∞}. The temperature distribution of the simplified cooled nozzle and the nozzle with the original design show good agreement with each other; additionally, the average and the trend of the blowing ratios of each row are substantially well matched. The results indicate that the optimization based on the simplified cooled nozzle is also valid for the nozzle with the original cooling design.

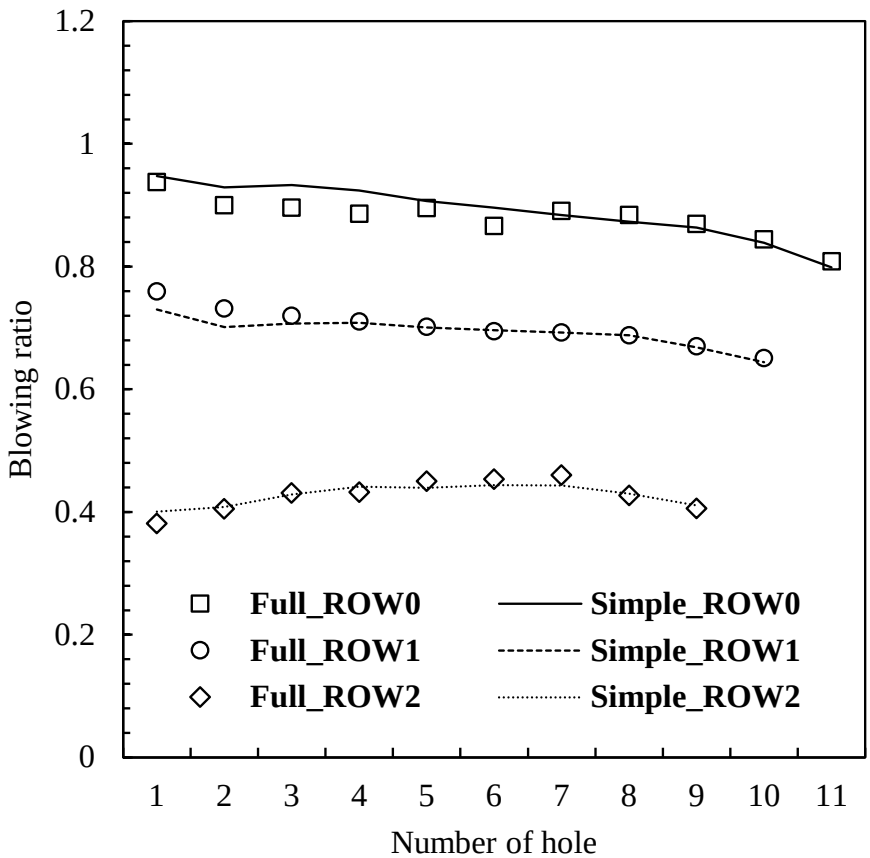

Fig. 3.6 Comparison of the blowing ratios

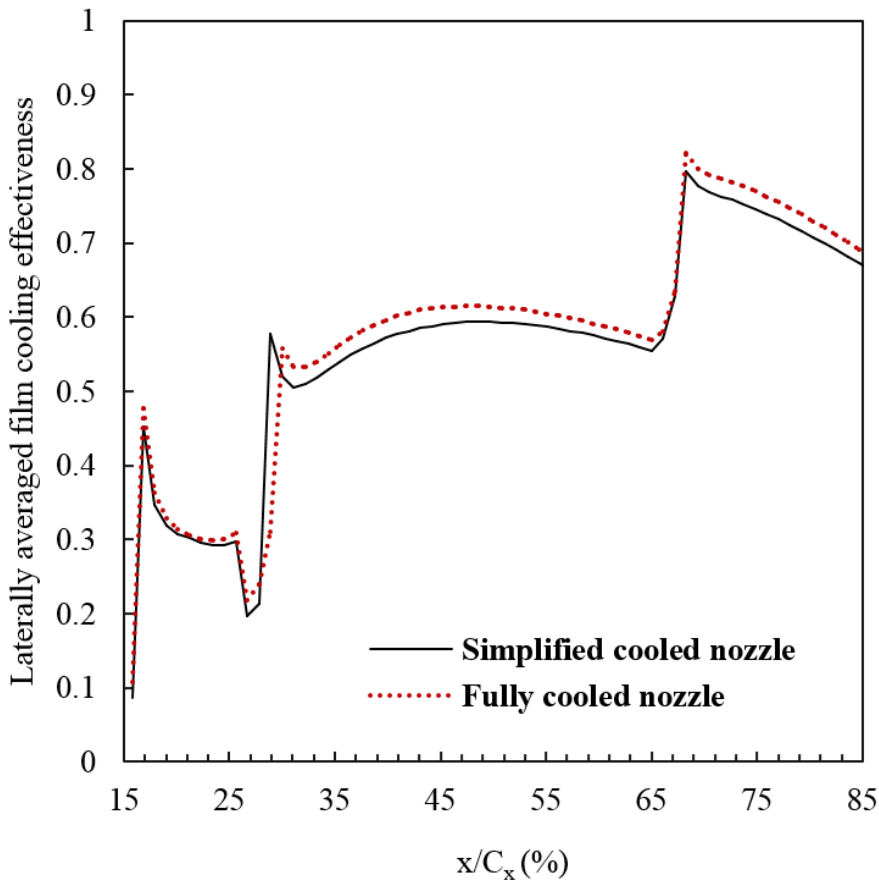

Fig. 3.7 Comparison of the laterally averaged film cooling effectiveness

Chapter 4. Deterministic optimization for the arrangement of film cooling holes

4.1 Parameterization for film hole array

To define the chordwise location of the holes, three design variables - chordwise location (R_ix), array gradient (R_ig), and array curvature (R_ic) - are used. R_ix is the hole position in the axial direction of the i-th row, which is normalized by the axial chord length of the nozzle. Because the respective location of the holes in the row could be different, R_ix refers to the location of the closest hole to the hub. The values of R_ig and R_ic range from -1 to +1. A value of +1 for R_ig indicates that the array has a diagonal shape, which splits the entire design space 1:1, to the lower right surface and the upper left surface. In contrast, a value of -1 for R_ig indicates that the array has a diagonal shape, which splits the entire design space 1:1, to the lower left surface and the upper right surface. Similarly, R_ic = +1 corresponds to the array that has a half ellipse shape convex towards the upstream and fills the entire design space, and R_ic = -1 corresponds to the array that has a half ellipse shape convex towards the downstream and fills the entire design space. The hole position in the axial direction defined by each variable is represented in eqs. (4.1) and (4.2), and Fig. 4.1(a) shows the schematic definition of the chordwise location variables.

$$x_{i,j_{grad}} = \frac{(y_{i,j} - y_{i,\min})}{(y_{i,\max} - y_{i,\min})}\mathbf{R_i g}(x_{i,\max} - \overline{\mathbf{R}}_\mathbf{i}\mathbf{x}) + \overline{\mathbf{R}}_\mathbf{i}\mathbf{x}\,,\ (0 \le \mathbf{R_i g} \le 1) \tag{4.1}$$

$$= \frac{(y_{i,j} - y_{i,\min})}{(y_{i,\max} - y_{i,\min})} \mathbf{R_i g}(\overline{\mathbf{R}}_\mathbf{i}\mathbf{x} - x_{i,\min}) + \overline{\mathbf{R}}_\mathbf{i}\mathbf{x}, \quad (-1 < \mathbf{R_i g} \le 0)$$

$$x_{i,j_{curve}} = a_0 y_{i,j}{}^2 + a_1 y_{i,j} + a_2, \tag{4.2}$$

$$\begin{bmatrix} y_{i,\max}^2 & y_{i,\max} & 1 \\ \{y_{i,\min} + (y_{i,\max} - y_{i,\min})/2\}^2 & (y_{i,\max}/2) & 1 \\ y_{i,\min}^2 & y_{i,\min} & 1 \end{bmatrix} \begin{bmatrix} a_0 \\ a_1 \\ a_2 \end{bmatrix} = \begin{bmatrix} \overline{\mathbf{R}}_\mathbf{i}\mathbf{x} \\ G \\ \overline{\mathbf{R}}_\mathbf{i}\mathbf{x} \end{bmatrix}$$

$$G = \mathbf{R_i c}(x_{i,\max} - \overline{\mathbf{R}}_\mathbf{i}\mathbf{x}) + \overline{\mathbf{R}}_\mathbf{i}\mathbf{x}, \qquad (0 \le \mathbf{R_i c} \le 1)$$

$$= \mathbf{R_i c}(\overline{\mathbf{R}}_\mathbf{i}\mathbf{x} - x_{i,\min}) + \overline{\mathbf{R}}_\mathbf{i}\mathbf{x}, \qquad (-1 < \mathbf{R_i c} \le 0)$$

The parameters $x_{i,j}$ and $y_{i,j}$ represent the hole position in the axial direction and the radial direction of the j-th hole of the i-th array, respectively. $x_{i,min}$ and $x_{i,max}$, denote the hole position in the axial direction of the low and high boundary of the i-th array's design space, respectively, and $y_{i,\min}$, and $y_{i,\max}$ denote the hole position in the radial direction of the low and high boundary, respectively. Subscripts of the $x_{i,j}$, grad and curve, indicate that each value is the gradient or curvature element of the array. Both $x_{i,j_{grad}}$ and $x_{i,j_{curve}}$ add up to the final position in the axial direction of the holes.

Because the array moves up and down, $y_{i,\min}$ is a function of $R_i x$ and $R_i y$, and $y_{i,\max}$ is the a function of $R_i x$, $R_i y$ and $R_i g$. These functions for $y_{i,min}$ and $y_{i,max}$ are highly determined by the nozzle geometry, especially the hub and shroud contouring shape. $R_i y$ is the value that normalizes the radial position of the array to

the half-length of the design space so that the values range from -1 to +1. The distances between the holes are also parameterized by the hole spacing (R_is) variable. Because the radial distances between the holes are designed to follow a geometric progression, the hole spacing increases or decreases monotonically. When $r_{i,l}$ is the expansion ratio that minimizes the hole interval at the hub side, and $r_{i,h}$ is the expansion ratio that minimizes the hole interval at the shroud side, r_i, the expansion ratio of the *i*-th row is determined by eq. (4.3). In consideration of manufacturability, the hole spacing is designed to be larger than 2.4D. The spanwise location of the *j*-th hole of the *i*-th array is given by eq. (4.4), and the schematic definition is described in Fig. 4.1(b). *n* refers to the number of the holes, and $y_{i,1}$ is equal to $y_{i,\min}$.

$$r_i = \mathbf{R_i s}\frac{(r_{i,h} - r_{i,l})}{2} + \frac{(r_{i,h} + r_{i,l})}{2} \tag{4.3}$$

$$y_{i,j} = y_{i,j-1} + \frac{r_i^{\,j-1}}{\sum_{k=1}^{n-1} r_i^{\,k}}(y_{i,\max} - y_{i,\min}), \qquad i = 1,2 \qquad j = 2,3,\cdots,n \tag{4.4}$$

By substituting $y_{i,j}$ of eq. (4.4) into eqs. (4.1) and (4.2), $x_{i,j\mathrm{grad}}$ and $x_{i,j\mathrm{curve}}$ are obtained. Next, by summing the two values, the final positions of all of the holes are determined.

Fig. 4.2 shows the arbitrary arrays of film cooling holes on real geometry generated by the shape function.

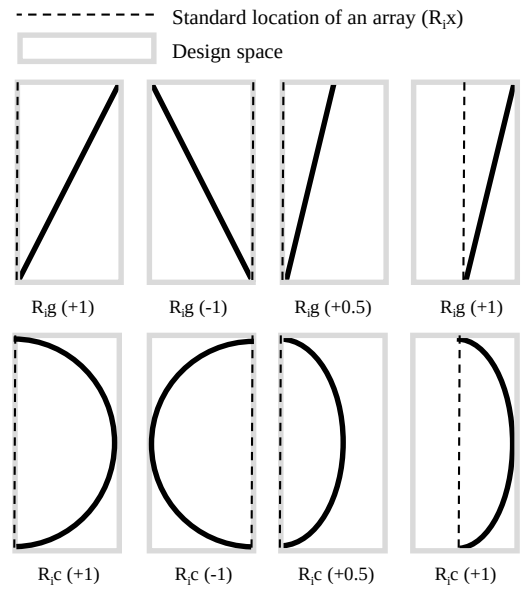

(a) For span location of the holes

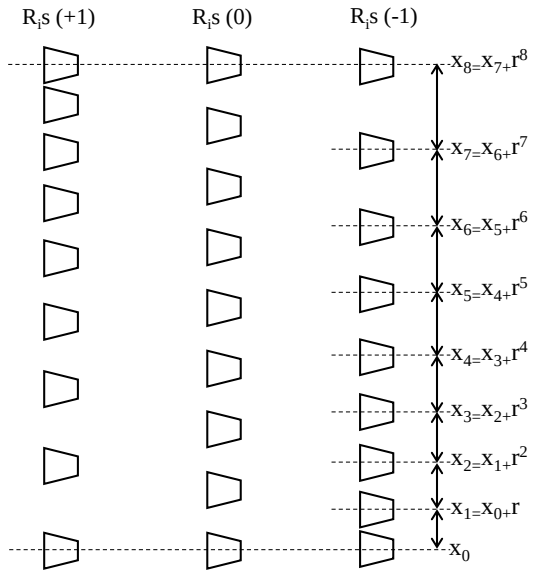

(b) For chordwise location of the holes

Fig. 4.1 Schematic description of the design variables

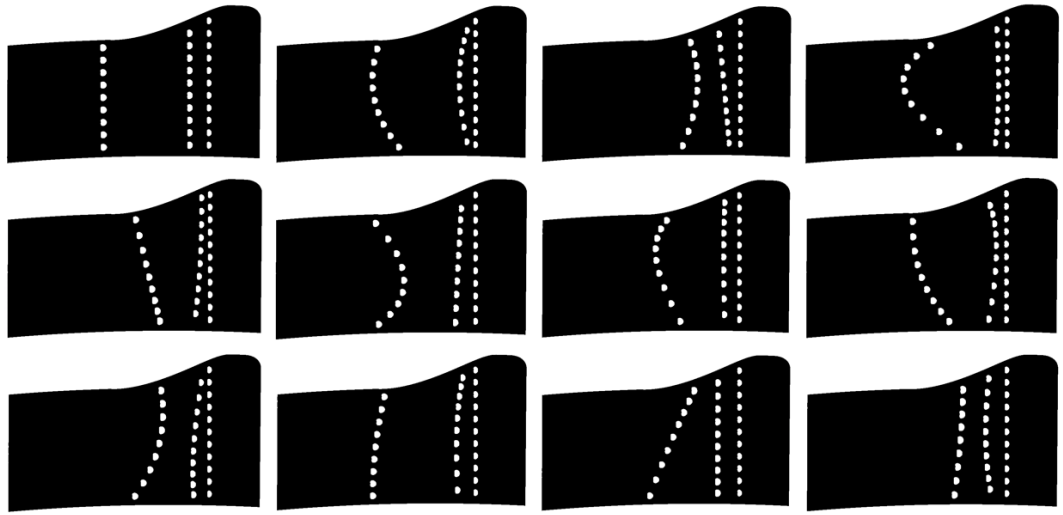

Fig. 4.2 Various film cooling hole arrays generated by the shape function

4.2 Optimization results

4.2.1 Problem definition

The major concern of the designing turbine cooling system is not only to reduce the surface temperature but also to reduce the temperature deviation of the adjacent regions. It is because that a temperature difference causing a thermal stress places a burden on the materials. In consideration of this issue, two objective functions are defined. One is to minimize the average surface temperature of the nozzle pressure side, and the other is to minimize the standard deviation of the surface temperature of the nozzle pressure side.

Also, mass flow rate of the cooling air is restricted as a constraints, because increase of cooling air could lead the deterioration of the entire turbine efficiency. This constraint condition is considered in an implicit manner by setting the boundary condition of the cooling passage inlet to constant value, $\dot{m}_{C_{ref}}$. This value is obtained by analyzing the reference cooled nozzle. Therefore, although the total mass flow ejected from the holes can slightly vary depending on the hole array shape, the difference is nearly negligible amount, approximately less than $0.005\% \dot{m}_{C_{ref}}$.

The optimization problem is formulated as follows.

Objectives

$$\text{Min. } T_{avg} = \frac{1}{A_{PS}} \iint_{A_{PS}} T_w(s) ds \tag{4.5}$$

$$\text{Min. } T_{dev} = \left\{ \frac{1}{A_{PS}} \iint_{A_{PS}} (T_w(s) - T_{avg})^2 \, ds \right\}^{1/2} \tag{4.6}$$

Constraint

$$\dot{m}_c - \dot{m}_{c_{ref}} \leq \varepsilon \tag{4.7}$$

The design spaces for each design variable are listed in Table 4.1. All of the design variables, except R_ix, are normalized values about the design space, so that the values range from -1 to +1. The (-) sign of R_ig and R_ic indicates that the array is leaned or curved to the flow direction, and the (+) sign indicates that the array is leaned or curved to the opposite direction. The (-) sign of R_iy and R_is indicates that the holes are more clustered near the hub than the shroud, and the (+) sign indicates that the holes are more clustered near the shroud than the hub. The optimization results will be presented by three values: the values of each objective function and the adiabatic film cooling effectiveness, defined in eq. (3.4)

Table 4.1 Design spaces for each design variable

Design Variable	Lower bound	Baseline	Upper bound
R_1x	0.183	0.252	0.268
R_1y	-1	0	1
R_1g	-1	0	1
R_1c	-1	0	1
R_1s	-1	0	1
R_2x	0.393	0.666	0.666
R_2g	-1	0	1
R_2c	-1	0	1
R_2s	-1	0	1

3.2.2 Optimization results

Sixty initial experimental points about nine design variables are selected and evaluated to construct the Kriging model. Then Pareto front that maximizes the EIs of each objective is drawn, and three of them, having maximum EI of the each objective and the mid-point of those two points, are selected as additional sampling points. This process is repeated until the Kriging model is converged.

Figure 4.3 shows the change of the objective functions during repeated processing. T_{avg} is not further improved after the 2nd refinement process, and T_{dev} is not further improved after the 5th refinement process. Therefore, the Kriging model was assumed to be converged after the 9th refinement process.

Figure 4.4 depicts the objective function values of the baseline and the additional sampling points, where a linear trend is found between both of the objective functions. Because the EI value is related to the minimum function value of the Kriging model as well as the uncertainty of the Kriging model, the additional sampling points have lower objective functions than the initial sampling points. This result indicates that the refinement of the Kriging model using EGO method is efficient because the accuracy of the model is intensively improved at the vicinity of the optimum points. The goodness of fits and the standardized residuals between the calculation and the estimation derived from the cross-validation analysis of the converged Kriging model, are shown in Fig. 4.5. Note that all of the estimated values of the Kriging model are in good agreement with the calculated values, although the accuracy of the model was refined only around the optimum points. In

addition, because the residuals of all of the estimated values are within 99.7% confidence interval, the Kriging model can be regarded to have sufficient reliability.

Once the Pareto front is obtained, three points among the non-dominated solutions are selected as the optimum points, which have the minimum T_{avg}, the minimum T_{dev}, and the minimum sum of the two objective functions.

OPT1 Min. T_{avg}

OPT2 Min. $(T_{dev} + T_{avg})$

OPT3 Min. T_{dev}

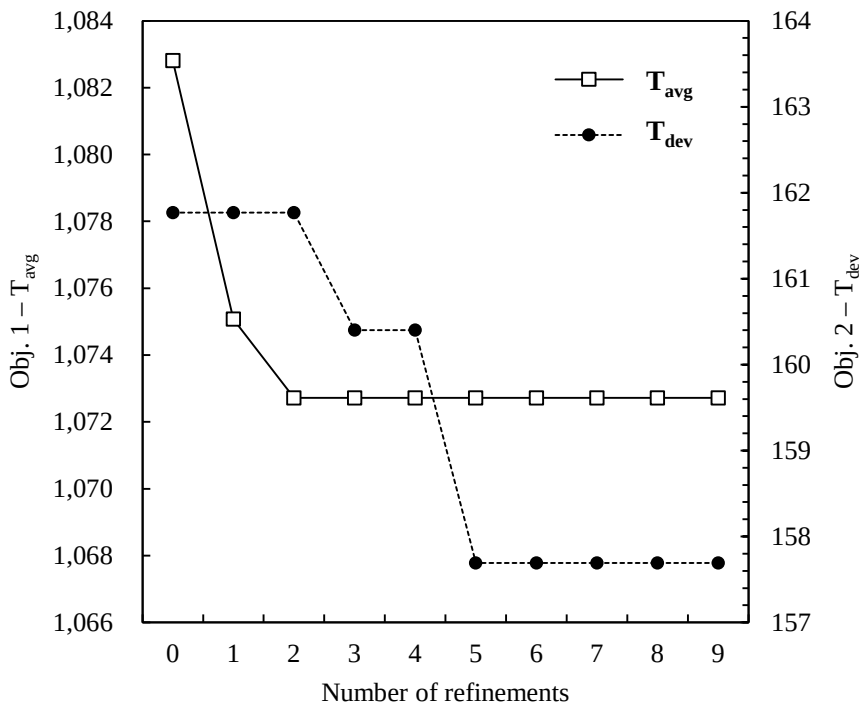

Fig. 4.3 Change of the objective functions

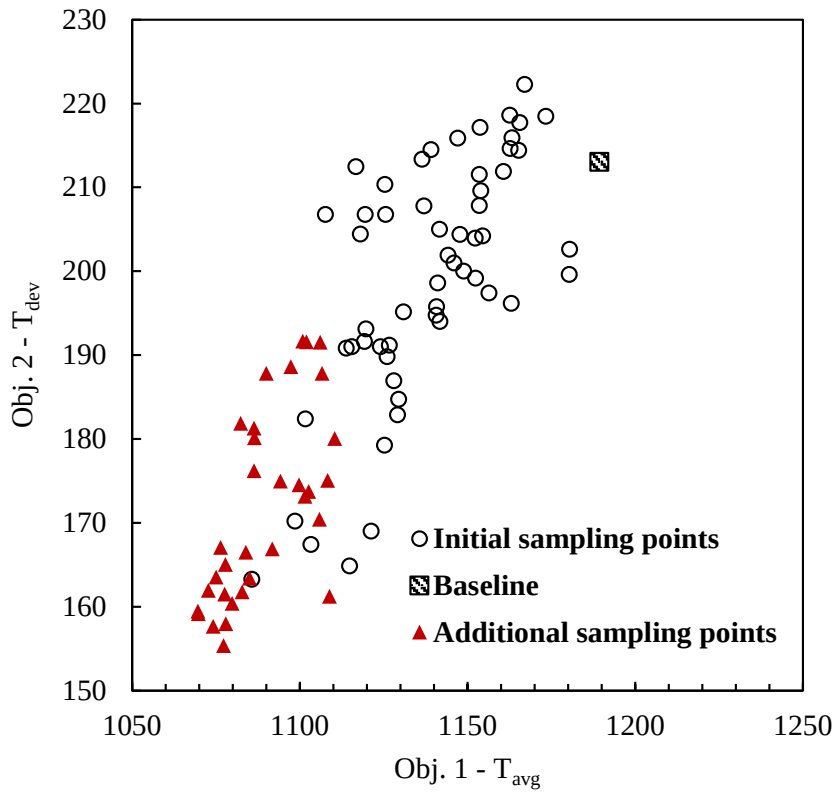

Fig. 4.4 Objective functions of the initial and the additional sampling points

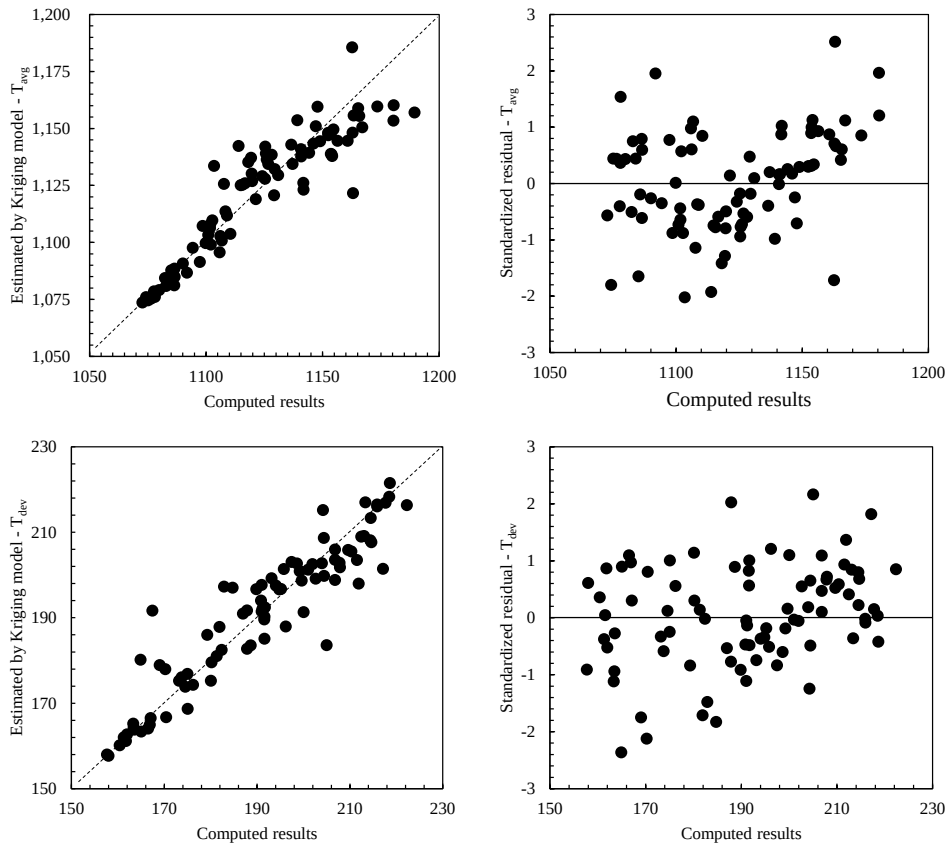

Fig. 4.5 Cross-validation results of the converged Kriging model

In addition, the non-dominated solutions are divided into three groups using clustering analysis, and the points that represent each group are suggested as another optimum points. *K-means* is used as a clustering method, which minimizes the distances between each cluster and each point [80]. Representative points correspond to the average value of the design variables of all of the points in each group, and each of those points is named REP1, REP2, and REP3. The trends and the characteristics of the optimum configurations regarding the objectives and the variables will be identified by these optima.

Figure 4.6 shows the optimum points on the Pareto front, and their configuration. The points involved in group 1, including the OPT1, OPT2, and REP1, have relatively lower T_{avg} than other non-dominated solutions. The points involved in group 2, including REP2, have T_{avg} that is higher than that of group 1 but lower than that of group 3, and T_{dev} that is higher than that of group 3 but lower than that of group 1. The points involved in group 3, including REP3 and OPT3, have relatively lower T_{dev} than the other non-dominant solutions. The estimated objective functions of the selected optima were validated by the calculation; the error of all of the six optima was confirmed to be less than 1%.

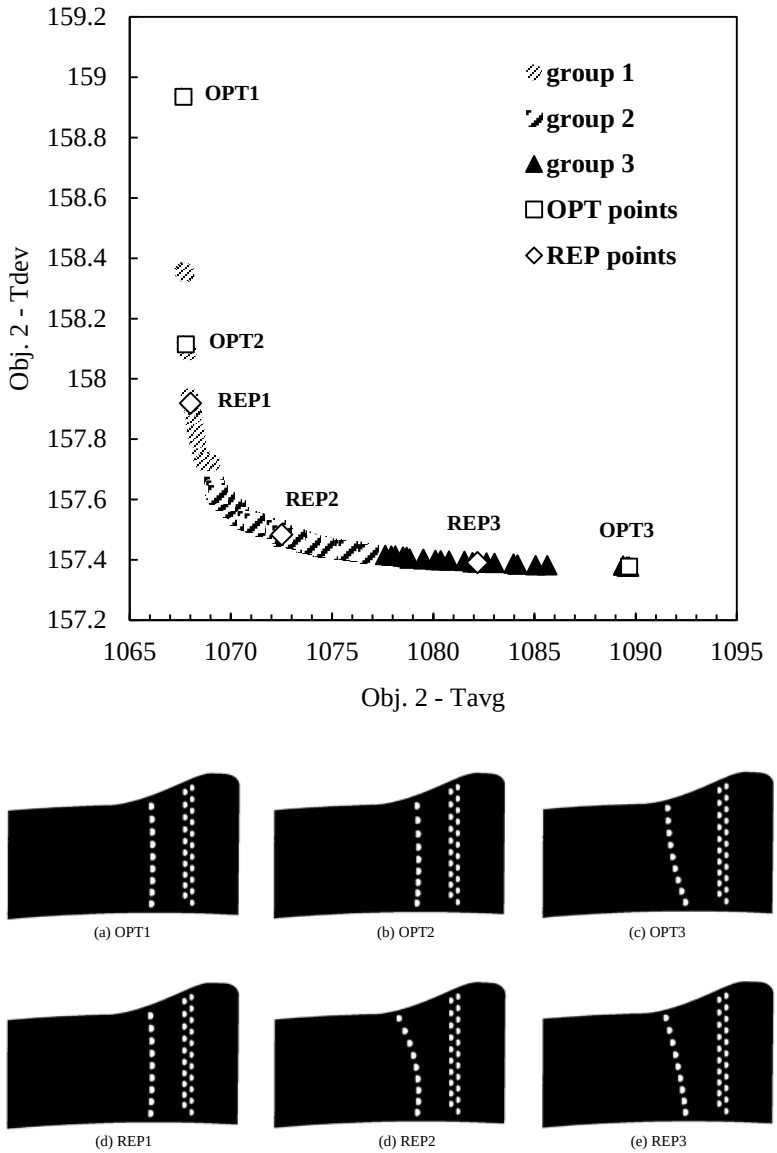

Fig. 4.6 Location of the optima on the grouped Pareto front and their configuration

Objective functions of the optima are listed in Table 4.2. The average reduction rate of T_{avg} is 9.83%, and the average reduction rate of T_{dev} is 25.89%. The optima for which T_{avg} decreased the most are OPT1, OPT2, and REP1, and the reduction rate of T_{avg} is approximately 10.11%. The performance of these three optima is substantially identical. The optimum for which T_{dev} decreased the most is OPT3, and reduction rate of T_{dev} is 27.13%. These results indicate that the cooling performance of the nozzle pressure side is greatly improved. In addition, the objective functions were confirmed to have linear trends with each other in the whole design space, but they follow a trade-off relationship in the vicinity of the optimum points.

Because trade-off relation between two objectives is so weak that the error of Kriging model seems possible to affect this relation. However, it is confirmed from Fig. 4.7 that analysis results by CFD is still has the trade-off relation.

The optimized shape of ROW1 appeared to be identical in all of the optima. The holes of ROW1 move upstream, at the boundary of the design space, and they are arranged in a staggered manner relative to the holes of ROW0. In contrast, optimized shape of ROW2 is slightly different by each group. The change of the array shape can be quantitatively investigated by examining the change of the design variables. The variables of REP2, REP3, OPT3 and, on behalf of group 1, REP1, are listed in Table 4.3 and the exact chordwise location of every holes of OPT1 and OPT3 are listed in Table 4.4 and 4.5.

Table 4.2 Comparison of the objective functions

	T_{avg} [K]	T_{dev} [K]		T_{avg} [K]	T_{dev} [K]
Baseline	1189.4	213.057	Baseline	1189.4	213.057
OPT1	1069.29	159.662	REP1	1069.18	159.302
Difference	-120.11	-53.395	Difference	-120.22	-53.755
Difference (%)	-10.10%	-25.06%	Difference (%)	-10.11%	-25.23%
OPT2	1069.25	158.856	REP2	1074.04	157.943
Difference	-120.15	-54.201	Difference	-115.36	-55.114
Difference (%)	-10.10%	-25.44%	Difference (%)	-9.70%	-25.87%
OPT3	1077.26	155.262	REP3	1075.87	156.352
Difference	-112.14	-57.795	Difference	-113.53	-56.705
Difference (%)	-9.43%	-27.13%	Difference (%)	-9.55%	-26.61%

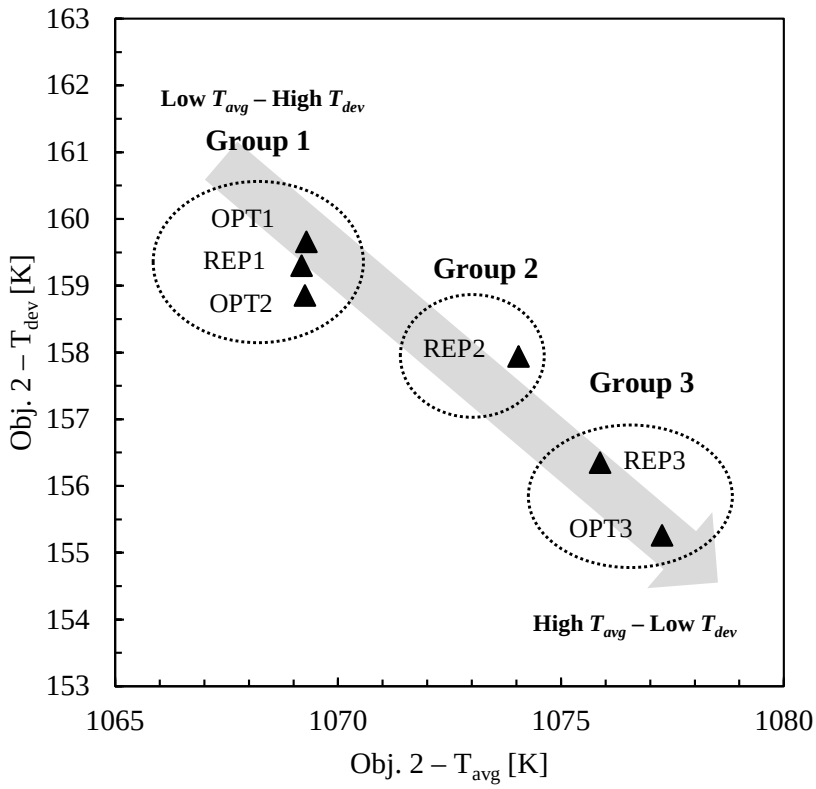

Fig. 4.7 Objective functions of the optima obtained by CFD

Table 4.3 Design variables of the baseline and the optima

Design Variable	Baseline	REP1	REP2	REP3	OPT3
R_1x	0.25	0.183	0.183	0.183	0.183
R_1y	0	0.682	0.718	0.718	0.718
R_1g	0	0.993	0.937	0.923	0.936
R_1c	0	0.309	0.375	0.374	0.377
R_1s	0	0.278	0.243	0.238	0.236
R_2x	0.67	0.395	0.396	0.396	0.396
R_2g	0	0.045	-0.354	-0.378	-0.347
R_2c	0	0.956	0.733	0.180	-0.0978
R_2s	0	0.048	0.125	0.090	0.116

Table 4.4 Hole location and spacing of OPT1

ROW1	x/C_x	p/D	ROW2	x/C_x	p/D
Hole1	0.183		Hole1	0.394	
		4.02			4.45
Hole2	0.183		Hole2	0.390	
		3.91			4.31
Hole3	0.183		Hole3	0.388	
		3.80			4.09
Hole4	0.183		Hole4	0.386	
		3.69			3.89
Hole5	0.183		Hole5	0.386	
		3.59			3.69
Hole6	0.183		Hole6	0.387	
		3.49			3.51
Hole7	0.183		Hole7	0.388	
		3.39			3.33
Hole8	0.183		Hole8	0.391	
		3.30			3.16
Hole9	0.183		Hole9	0.395	
		3.21			
Hole10	0.183				

Table 4.5 Hole location and spacing of OPT3

ROW1	x/C_x	p/D	ROW2	x/C_x	p/D
Hole1	0.183		Hole1	0.492	
		3.95			3.93
Hole2	0.183		Hole2	0.490	
		3.86			3.86
Hole3	0.183		Hole3	0.485	
		3.77			3.79
Hole4	0.183		Hole4	0.478	
		3.68			3.72
Hole5	0.183		Hole5	0.467	
		3.59			3.65
Hole6	0.183		Hole6	0.454	
		3.51			3.58
Hole7	0.183		Hole7	0.438	
		3.43			3.52
Hole8	0.183		Hole8	0.419	
		3.35			3.45
Hole9	0.183		Hole9	0.396	
		3.27			
Hole10	0.183				

For these optima, the values of R_1g and the R_1c are meaningless because the sign of these variables are (+) and R_1x is on the lower boundary of the design space. There is no more space for ROW1 to curve or to incline. The value of R_1y increases until the holes of ROW1 have staggered positions relative to the holes of ROW0. In addition, from the value of R_1s, the holes of ROW1 are found to be slightly clustered at the hub side.

In case of ROW2, similar to ROW1, R_2x is on the lower boundary of the design space, but ROW2 of REP2, REP3, and OPT3 are inclined and curved to the trailing edge because one or both of the values of R_2g and R_2c are negative. Whereas, REP1 has a positive value of R_2g and R_1c, consequently, ROW2 of REP1 appeared to be straightly aligned same as ROW1s. REP2, REP3 and OPT3 are similar in value of R_2g, which is 0.34~0.38, while the value of R_2c decreases in the following order: REP2, REP3 and OPT3. The value of R_2c of each optimum is 0.73, 0.18 and -0.10, respectively, i.e., the shape of the arrays is changed from the convex to the concave to the flow direction. The location of the holes at the both ends of the array appeared to be identical because all of the ROW2 variables, except R_1c, are similar in all cases. Only the direction and magnitude of the curvature between two holes are different.

In the case of REP2, ROW2 has a straight line on the lower surface of the mid-span and has a diagonal line inclined to the trailing edge on the upper surface of the mid-span. The entire array shape appears as a convex curve to the flow direction. In the case of REP3, ROW2 is inclined from the hub to the shroud, such that the

entire array shape appears to be closer to a diagonal line than a curve. In the case of OPT3, ROW2 is inclined from the hub to the mid-span and has a straight line on the upper surface of the mid-span. Thus, the whole array shape appears as a concave curve to the flow direction. Similar to the holes of ROW1, those of ROW2 of all of these four cases are slightly clustered to the hub side, but less than ROW1.

Figure 4.8 shows the adiabatic film cooling effectiveness of the baseline and the optima, OPT1 and OPT3. The film cooling effectiveness at the surface between ROW0 and ROW1 is found to be significantly improved by relocating holes of ROW1, which move forward and upward and cover the large uncooled area of that surface. In addition, in the baseline, the film cooling effectiveness near the hub is lower than that near the shroud, whereas in the optima, the film cooling effectiveness near the hub is higher than that near the shroud. This result occurs because the hole distances near the hub become smaller than those near the shroud, thereby leading to improvement of the film cooling performance near the hub of the nozzle.

From Fig. 4.8, the high-cooling region and the low-cooling region are found to appear alternately in the baseline, but this pattern is mitigated in the optima. As a result, the temperature deviation is notably mitigated at the optima by virtue of the hole staggering and the hole clustering. Figure 4.9 shows the film cooling effectiveness at the normalized span location of the baseline and the optima. For $x=0.35C_x$, the variation of the film cooling effectiveness is greatly reduced compared to the baseline over the entire region, except at both ends of the span,

where the film cooling is unable to cover the surface. For x=0.8Cx, although the average film cooling effectiveness decreases, the variation is notably reduced.

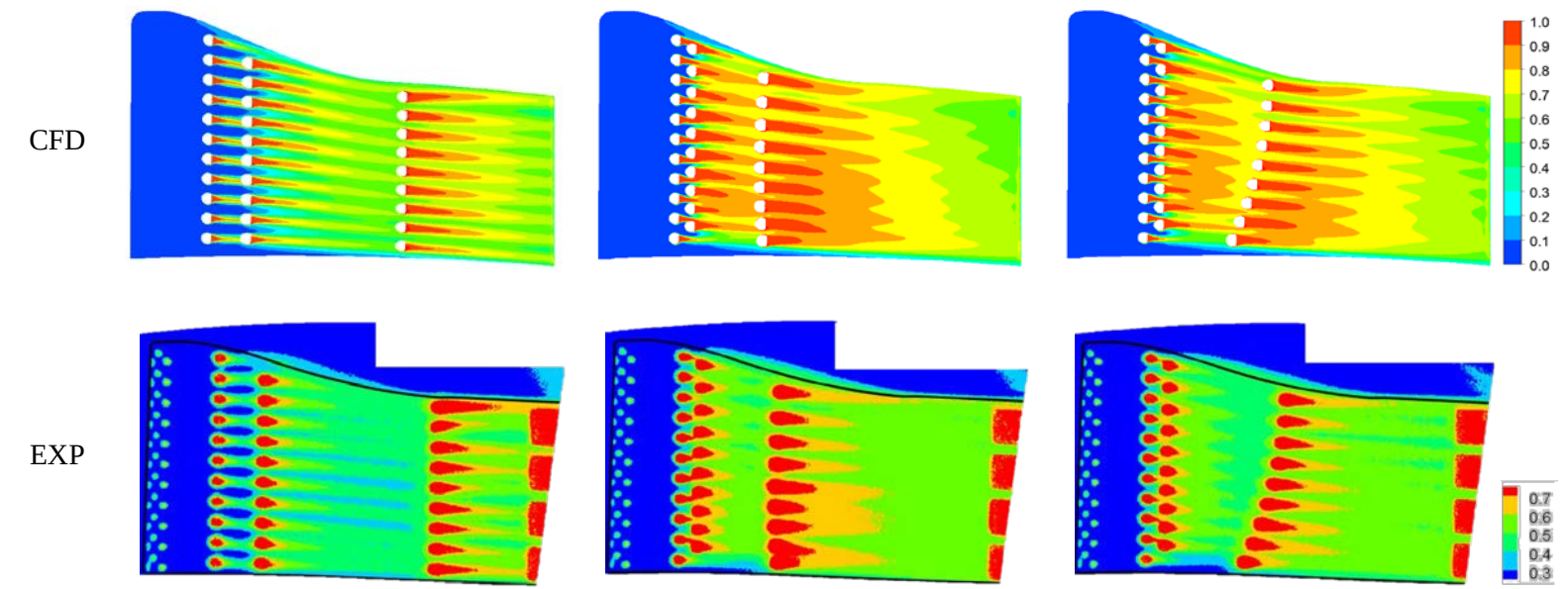

Fig. 4.8 Film hole array generation using the shape functions

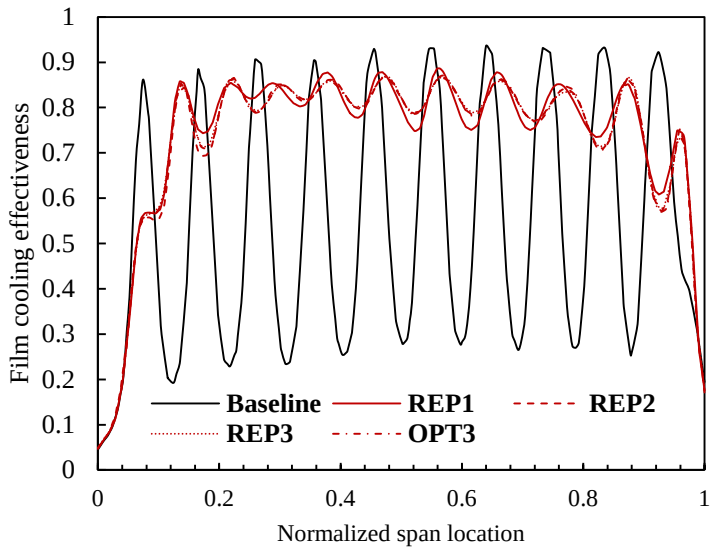

(a) at x=0.35Cx

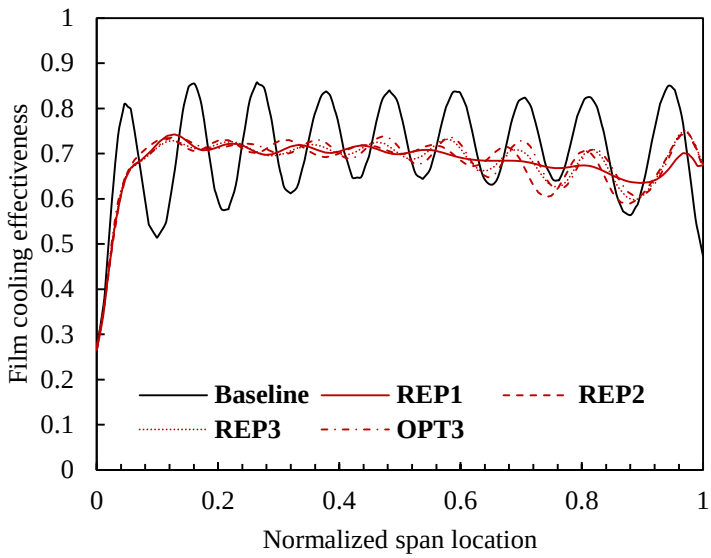

(b) at x=0.80C

Fig. 4.9 Comparison of the film cooling effectiveness

To validate the effectiveness of optimization results, experimental study is performed with transonic turbine cascade test facility in Korea Aerospace Research Institute (KARI).

Figure 4.10 presents the schematic view of experimental set up, which comprises the main air supply line, the test section, the secondary flow supply system, and the control system. The 500 HP compressor supplies the air which passes through the 300kW heater and venturi flow meter into the test section and then discharged to ambient air. Two 50 HP compressors supply the air to the manifold and control valve system for simulating the coolant flow. The FLIR Infrared camera with the optical access window made of Germanium is installed near the sidewall of the test section for measuring the temperature distribution on the surface.

There are five nozzle guide vanes and four flow passages in the annular turbine sector cascade. The test nozzle vanes shown in Fig. 4.11 are three times scaled-up model of the design geometry and made by a stereo-lithography method. They have all the cooling components, as well as pressure side film cooling holes.

The average values and contours of film cooling effectiveness obtained by experiments are given in Fig. 4.8 and 4.12. It is obvious that there are certain discrepancy between CFD and experiment, so different contour levels are applied to compare the pattern and trend of film cooling effectiveness in Fig. 4.8. These comparison results show the over-estimation of CFD analysis, but also indicate that their trend and pattern of the film cooling effectiveness are quite similar.

Detailed set up procedure of experiment and comparison study between CFD and experiment was elaborated in Rhee et al.'s work [78].

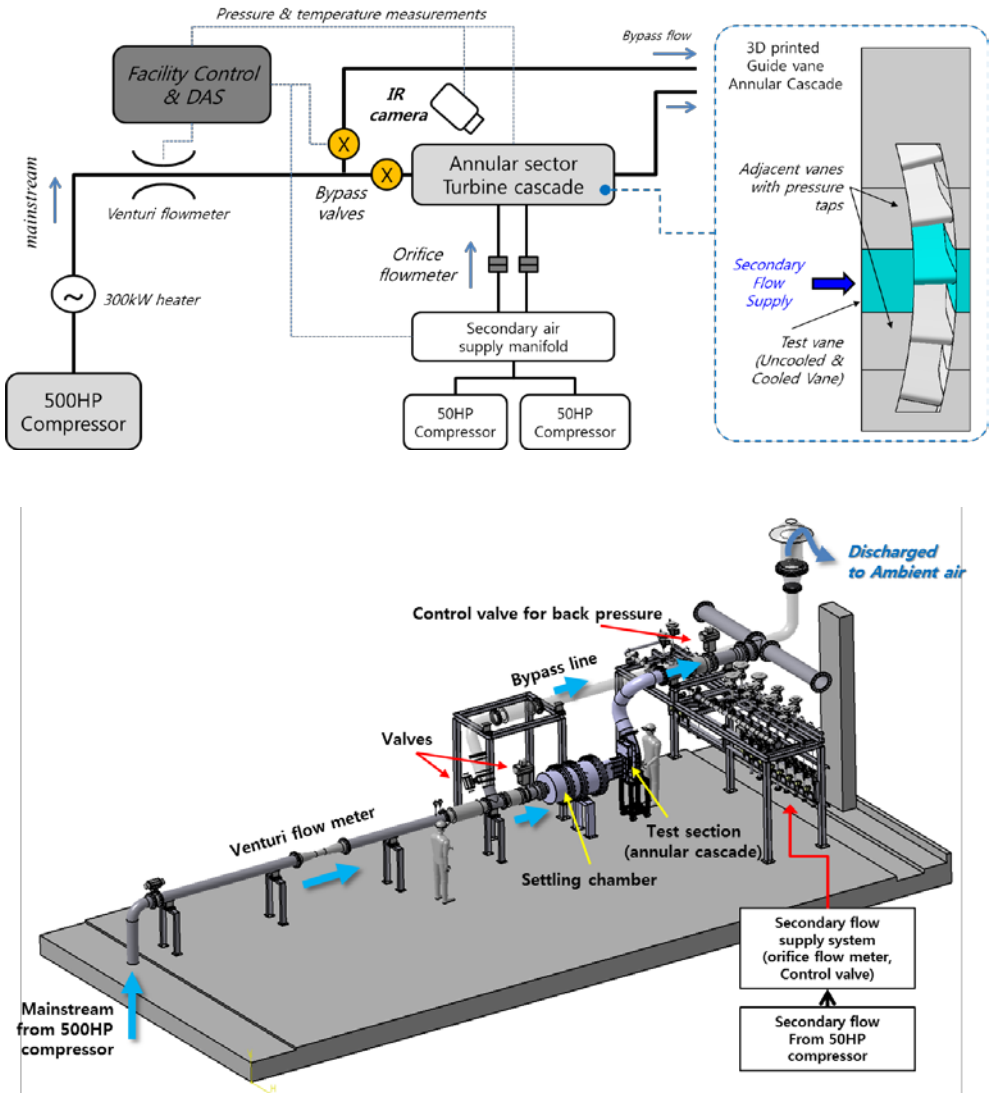

Fig. 4.10 Schematic diagram of experimental apparatus

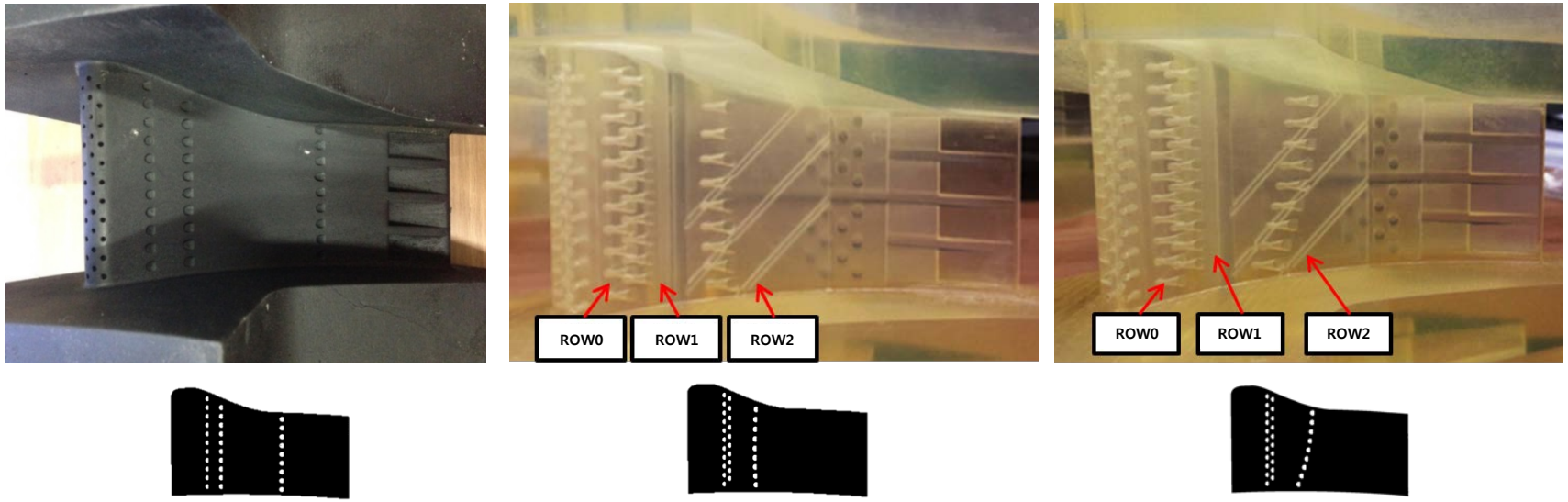

(a) Baseline (with black paint coated) (b) OPT1 (c) OPT3

Fig. 4.11 Experimental model of the nozzle

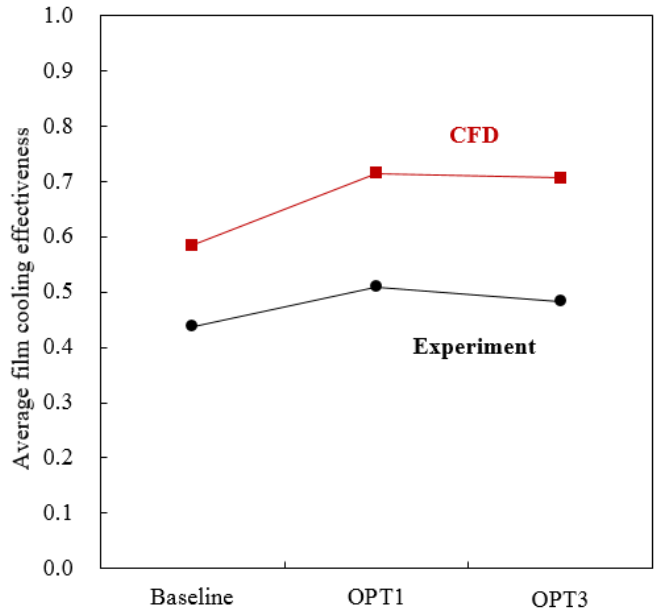

(a) Averaged film cooling effectiveness

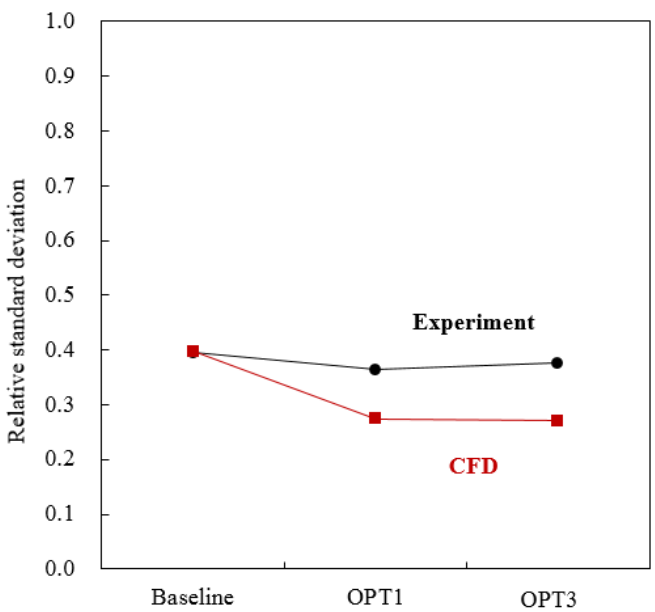

(b) Relative standard deviation of the film cooling effectiveness

Fig. 4.12 Comparison of CFD results with experiment

From the analysis of variables (ANOVA), it is possible to investigate the influence of each variable on each objective function. [81] Because the variables are parameterized by the shape function, the influence of each variable on the objective functions is not independent. Therefore, the variables are divided into two groups. One group is the group of the chordwise location variables, including $R_i x$, $R_i g$, and the $R_i C$, which are related to the axial direction hole position. The other group is the group of the spanwise location variables, including $R_i y$ and $R_i s$, which are related to the radial direction hole position. The ANOVA results of the non-dominated solutions are shown in Fig. 4.13. The graphs show that ROW1 has a dominant influence on both of the two objective functions. In particular, T_{dev} is almost determined by the shape of ROW1. However, because the shapes of ROW1 of the optima are substantially identical, T_{dev} appeared to be nearly unchanged compared to T_{avg} on the Pareto front.

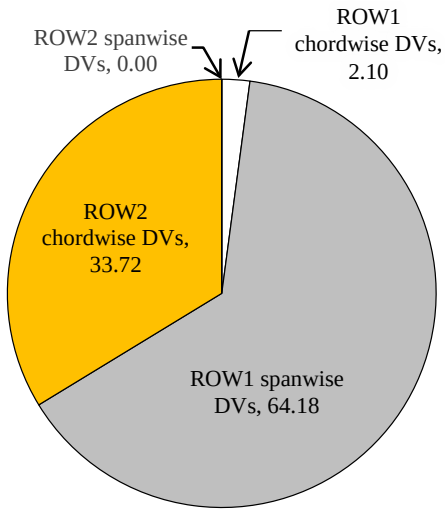

(a) Obj. 1 - T_{ave}

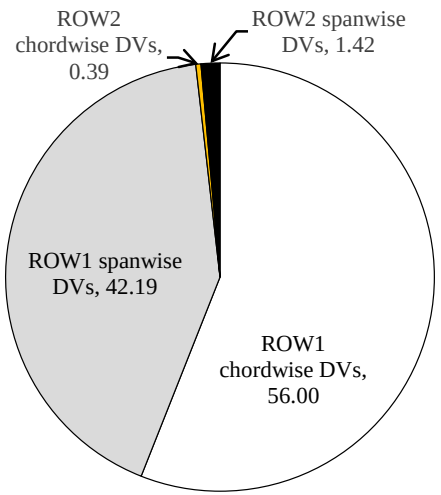

(b) Obj. 2 - T_{dev}

Fig. 4.13 ANOVA results of the optimization results

In the case of ROW1, while T_{dev} is similarly affected by the both groups, T_{avg} is dominantly affected by the group of spanwise location variables. It can be interpreted that, to form a staggered position to ROW0 is more effective than to cover the uncooled area between ROW0 and ROW1, in T_{avg} reduction. However, these two effects similarly affect the T_{dev} reduction. In contrast to the case of ROW1, the spanwise location variables of ROW2 have a dominant influence on T_{dev}, and the chordwise location variables of ROW2 have a dominant influence on T_{avg}.

Temperature contours near the pressure side surfaces are shown in Fig. 4.14. For the baseline case, the coolant ejected from each hole is hardly interact with each other, and makes separate cooling region. On the other hand, for the optimum cases, coolant interacts with each other, is attached to the surface, and then consequently builds evenly distributed cooling region.

Figure 4.15 shows the laterally averaged adiabatic film cooling effectiveness of the baseline cooled nozzle, and simplified cooled nozzle with the optimum film cooling hole arrays. Compared to the baseline, the film cooling effectiveness of the optimum arrays is greatly improved over the entire surface except trailing edge, whose cooling performance is deteriorated to a certain degree, because all of film cooling holes are moved upstream. Comparing the film cooling effectiveness between the optimum arrays, there is certain degree of difference for 0.4~0.5 C_x, but they are substantially identical in other regions. REP1, whose array shapes are close to straight lines, has the maximum film cooling effectiveness of 0.85 at $0.4C_x$,

which is the highest among all of the configurations. REP2, REP3, and OPT3 have the maximum film cooling effectiveness of 0.83 at $0.5C_x$. ROW2s of these configurations are curved and inclined to the trailing edge, and $0.5C_x$ is the end point of the ROW2s. The baseline has the maximum film cooling effectiveness of 0.80 at $0.85C_x$, much closer to the trailing edge than other configurations.

At the $0.4\sim0.5C_x$ region, because the holes of ROW2s are distributed differently, the distribution of the film cooling effectiveness is also appeared to be different. Film cooling effectiveness of REP1 rapidly increases at $0.4C_x$ and decreases until the trailing edge. Those of the other configurations increase slowly from $0.4C_x$ to $0.5C_x$, and then decrease. Because the REP1 has the highest film cooling effectiveness among the optima, other optimum arrays have higher T_{avg} than REP1, by amount of the difference of the wall temperature between REP1 and the other optimum arrays at the $0.4\sim0.5C_x$ region. This result indicates that REP1 is the most effective film cooling hole array, and to reduce the temperature deviation, loss of some degree of cooling performance of film cooling is inevitable. To this end, some of the holes of the ROW2 move to the trailing edge, consequently, rapid decrease of the temperature become smooth.

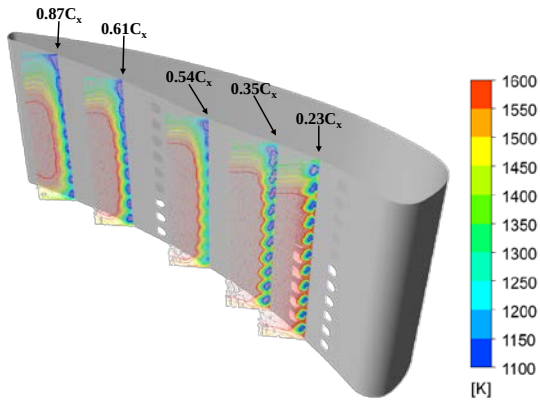

(a) Baseline

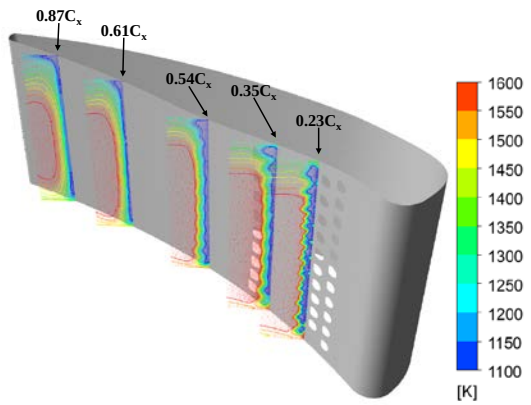

(b) OPT1

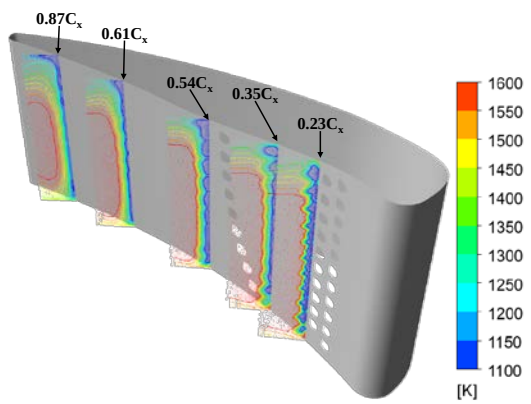

(c) OPT2

Fig. 4.14 Temperature contour near the surface

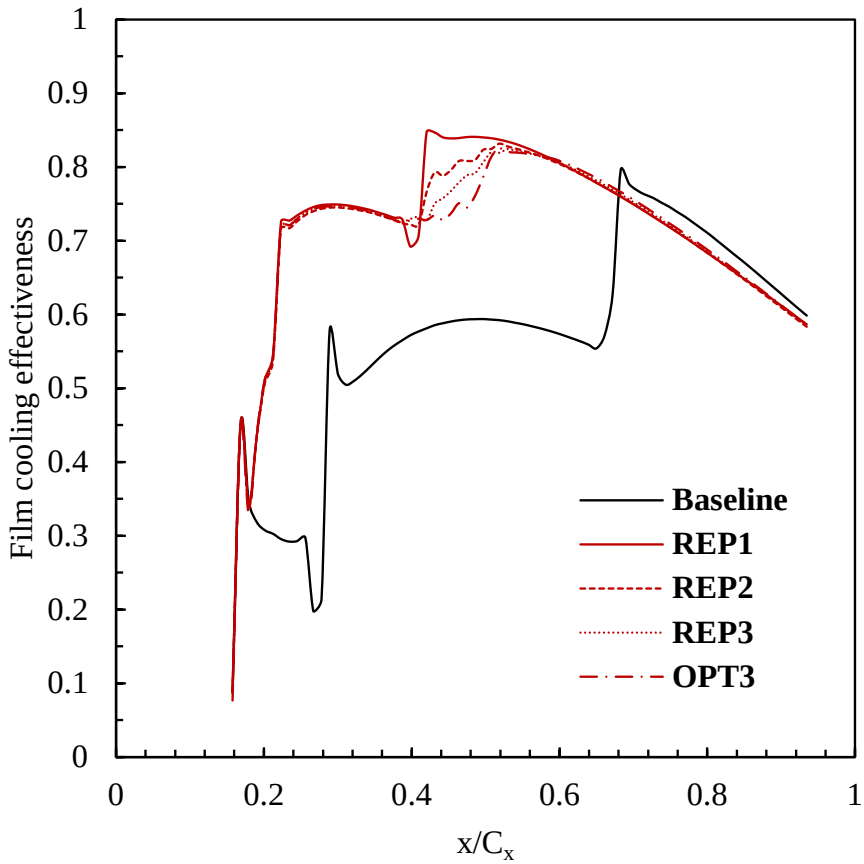

Fig. 4.15 Comparison of the laterally averaged film cooling effectiveness

The average blowing ratio of each array is listed in Table 4.6. Because the mass flow rate of the cooling air ejected from the film cooling holes is restricted by the boundary condition, the change of the blowing ratio is caused by the change of the external flow condition. Because the flow through the nozzle is accelerated, the holes located downstream have a relatively lower blowing ratio. Because ROW0 is unchanged, the blowing ratio of ROW0 is also unchanged. The blowing ratios of the optimum ROW1s are almost the same with each other, but are quite higher than that of the baseline because the holes of the ROW1s of all of the optima move upstream. Generally, it is known that the low blowing ratio yields high film cooling effectiveness, while on the concave surface, such as a nozzle pressure side, a high blowing ratio yields high film cooling effectiveness. The results indicate that the combination of the increase of the blowing ratios, the reduction of the uncooled area, and the performance improvement of each film cooling holes leads to a great improvement of the cooling performance of the nozzle with the optimum arrays.

The blowing ratios of the ROW2s appeared to be different because the shapes of the optimum arrays are different with each other. The blowing ratio of the baseline, whose ROW2 holes are located on the downstream end of the design space, is the lowest, and that of REP1, whose ROW2 holes are located on the upstream end of the design space, is the highest. Because the blowing ratio decreases as the average chordwise hole location increases, the value of the blowing ratio decreases in the order of REP2, REP3, and OPT3. REP1, which has the highest cooling performance, is found to have the highest blowing ratio.

Table 4.6 Comparison of the blowing ratios

	ROW0	ROW1	ROW2
Baseline	0.89	0.69	0.43
REP1	0.90	0.83	0.78
REP2	0.90	0.83	0.74
REP3	0.90	0.83	0.71
OPT3	0.90	0.83	0.67

Chapter 5. Uncertainties in the film hole array optimization

5.1 Manufacturing tolerance of film hole

As mentioned in Chapter 1, Bunker [57] categorized 7 manufacturing factors for a film cooling hole. However, these factors are not entirely independent in real film hole geometry. Some manufacturing factors may appear in a coupled manner. For example, a change of the film hole orientation with respect to the flow could change the exit hole shape or hole length simultaneously.

For that reason, 2 representative manufacturing factors, which are assumed to cover all of the effects of manufacturing tolerance, are defined. One is the injection angle (α_i); the other is the scaling factor (SF). Film holes are modeled using a fan-shaped film hole core, as shown in Fig. 5.1, and the injection angle is defined as the hole core orientation with respect to the nozzle surface; the scaling factor is defined as an extension/extraction ratio of the hole core. Because the nozzle wall thickness is unchanged, the film hole length to diameter ratio (L/D), film hole angle to surface tangent, film hole orientation to external/internal flow, and film hole pitch to diameter ratio (P/D) change with the variation of injection angle; additionally, the film hole diameter, film hole L/D, film hole P/D, and film hole exit shape change with the variation of the scaling factor. The tolerance range of the scaling factor is determined to be 10%, based on Bunker's work [57], but the range of the injection angle is reduced from 5° to 3° by considering the real geometry and modeling restrictions.

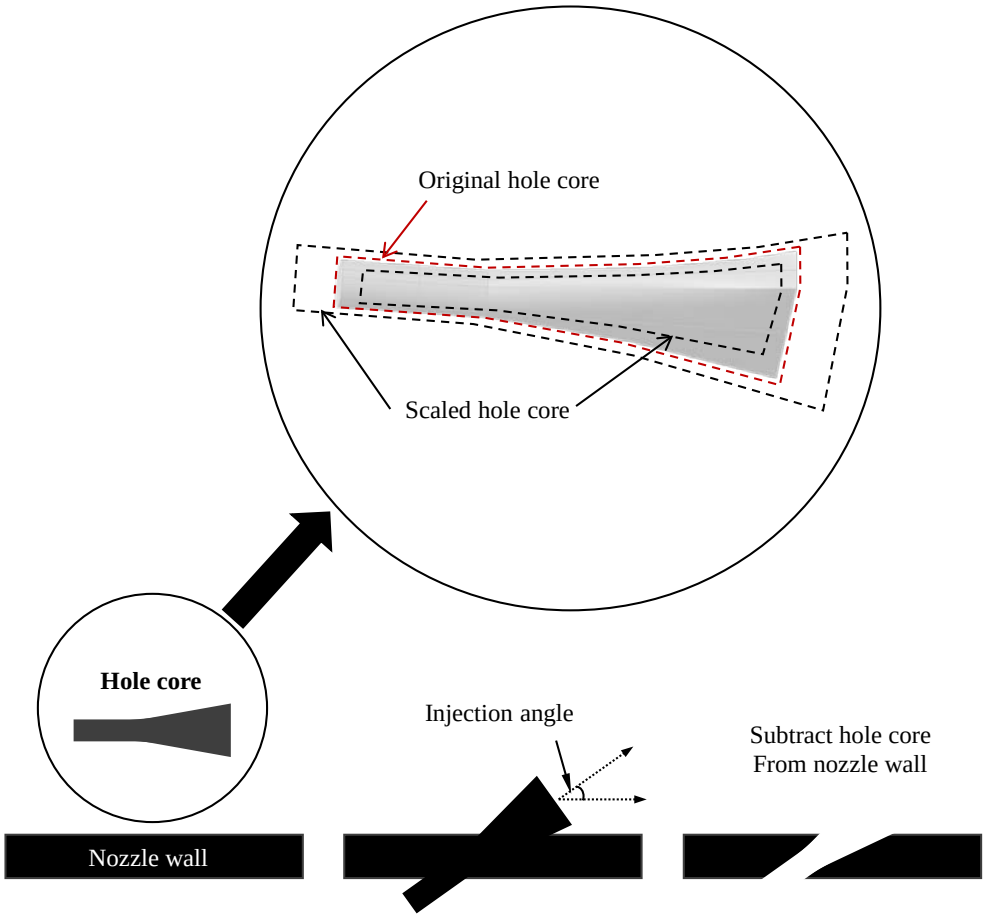

Fig. 5.1 Applying uncertainties to the process of film hole modeling

The corresponding variation range of Bunker's seven manufacturing factors [57] with the variation of newly defined manufacturing factors has been investigated and listed in Table 5.1. The variation range of film hole diameter, three factors regarding hole orientation, and film hole P/D have a prescribed value—10% and 3°. Only film hole L/D and film hole shape exit spec have been calculated from the hole with intentionally modeled tolerance. As a result, both of the factors appear to have a greater variation than Bunker's work [57], despite the fact that the variation range for hole orientation is reduced from 5° to 3°. One of the reasons could be that the hole considered is a fan-shaped hole, which is more sensitive to the manufacturing tolerance than a cylindrical hole.

Table 5.1 Comparison of the tolerance of manufacturing factors

Tolerance Factor	Bunker [57]	Present
Film hole diameter (effective)	10%	10%
Film hole L/D	6%	-17%~21%
Film hole angle to surface tangent	5°	3°
Film hole orientation to external flow	5°	3°
Film hole orientation to internal flow	5°	3°
Film hole P/D	10%	10%
Film hole shaped exit spec	30%	-31%~45%

The truncated Gaussian distribution is used as a PDF for the uncertainties because it is a generally accepted distribution for natural events and there is no known probabilistic distribution for manufacturing tolerance of a film cooling hole. The standard deviation for the PDF is determined to satisfy the requirement that the probability within the range is 99.9%.

Each hole has its own tolerance in reality. However, it is nearly impossible to render dozens of film holes to have their own tolerance. Therefore, some assumptions are made for simplification: 1) the pressure side surface is a flat plate and 2) holes in the same row are made under the same manufacturing circumstances. From the first assumption, the variance of the injection angle is identically applied to all of the holes at the pressure side surface. From the second assumption, the variance of the scaling factor is identically applied to the holes in the same row. Thus, it is possible to address the tolerance of the holes with only 4 uncertainties: injection angle for all holes, SF for holes in ROW0, SF for holes in ROW1, and SF for holes in ROW2. These uncertainties and factors for defining their PDFs—mean (E), standard deviation (σ), and variation range—are listed in Table 5.2.

Table 5.2 Related factors for PDF of manufacturing tolerance

	Scaling factor (SF0, SF1, SF2)	Injection angle (α_i)
Mean (E)	1.0000	30.0000
Variance (σ)	0.0304	0.1204
Range	0.9~1.1	27°~33°
PDF	Gaussian distribution 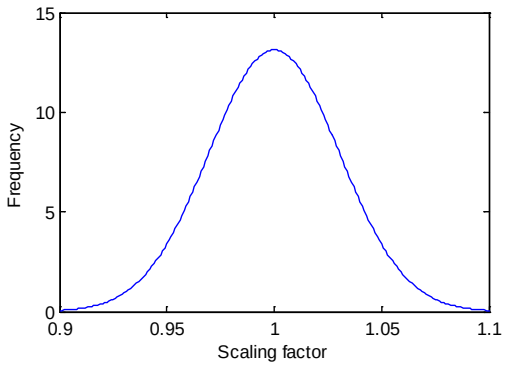	Gaussian distribution 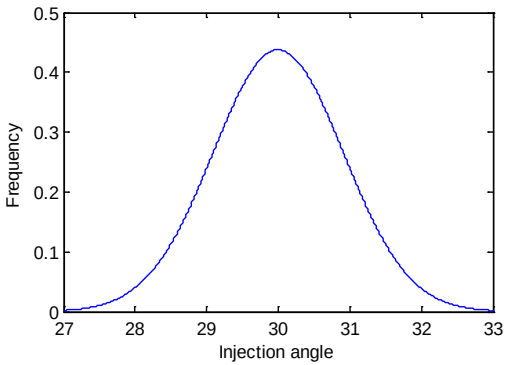

5.2 Blowing ratio of film hole

Blowing ratio is one of the principal factors for film cooling performance. As presented in eq. (3.1), it is defined as a ratio of mass flux between cooling air and main flow. Despite the importance of the blowing ratio in film cooling performance, its variance is inevitable in an actual turbine due to the unsteady nature of the flow fields, interaction of the rotor-stator, manufacturing tolerance of film holes, etc. Abhari [82] investigated the impact of rotor-stator interaction on film cooling; Babaee et al. [83] examined the effects of uncertainty in the blowing ratio on film cooling effectiveness. These studies showed that variance of the blowing ratio is up to 30% and that it changes the film cooling effectiveness by 20% at maximum. Montomoli et al. [54] also reported that up to -50% blowing ratio variation is observed, depending on the combustor exit condition.

Because there is no published literature that investigates the uncertainty in the blowing ratio, the variance of the blowing ratio is determined to be 30%, referring to the studies mentioned above. The PDF type is Gaussian distribution with a mean value of 1.0, which indicates the designed blowing ratio of each hole.

Because blowing ratio can also be interpreted as a ratio of mass flow rates divided by the hole area, the variance of the mass flow rate of the cooling air is equivalent to the variance of the blowing ratio with the same hole configuration. Therefore, the mass flow rates of the supplied cooling air, which are set by boundary conditions of the passage inlet, are controlled to allow the blowing ratio variation.

Table 5.3 shows the factors for defining PDFs and PDF configurations.

Table 5.3 Related factors for PDF of blowing ratio

	1st passage mass flow (M#1)	2nd passage mass flow (M#2)
Mean (E)	1.0000	1.0000
Variance (σ)	0.0912	0.0912
Range	0.7~1.3	0.7~1.3
PDF type	Gaussian distribution 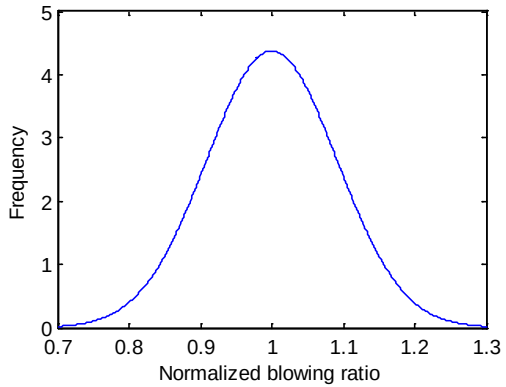	Gaussian distribution 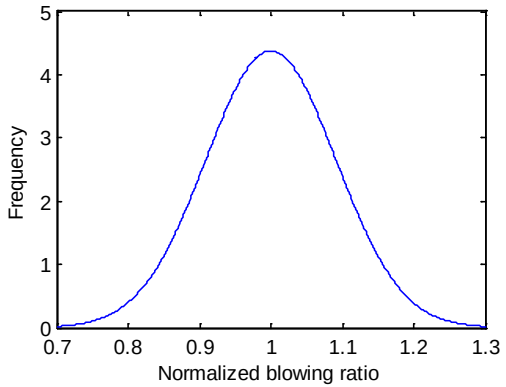

5.3 Turbine inlet temperature distortion

In this study, various types of 2D TIT profiles are applied to consider the circumferential non-uniformity of TIT distribution. The most widely used parameter to represent distortion of the exhausted gas temperature is the Pattern factor (P), which is obtained from eq. (5.1) [84]

$$P = \frac{T_{\max} - T_{avg}}{T_{avg}} \tag{5.1}$$

T_{max} is the maximum temperature; T_{avg} is the average temperature of the TIT profile. Deviation of TIT is easily comprehended based on the Pattern factor, but an additional parameter is required to impose the bias of the temperature distribution. Bias factor (r_{max}) is newly introduced to define the radial location of maximum temperature. r_{max} is a non-dimensional parameter that ranges from 0 to 1.

Generally, the TIT profile is presented in the form of a convex curve that has a comparably low temperature and steep temperature gradient near the wall. To present a TIT profile using P and r_{max}, the beta distribution function in eq. (5.2) is used as a shape function

$$f = \frac{1}{B(q,r)} x^{q-1}(1-x)^{r-1} \tag{5.2}$$

where q and r are the parameters for the beta function, x is the normalized span

location, and $B(\cdot)$ is a beta function, defined as eq. (5.3)

$$B(q,r) = \int_0^1 x^{q-1}(1-x)^{r-1}dx \tag{5.3}$$

Because eq. (5.2) has the maximum temperature at r_{max}, eqs. (5.4) and (5.5) are derived.

$$\left[\frac{1}{B(q,r)} r_{\max}{}^{q-1}(1-r_{\max})^{r-1}\right]' = 0 \tag{5.4}$$

$$\frac{1}{B(q,r)} r_{\max}{}^{q-1}(1-r_{\max})^{r-1} = T_{avg}(P+1) \tag{5.5}$$

Using the two equations above, unknowns q and r can be determined. Once q and r are known, the 2D TIT profile can be drawn. Figure 5.2 shows examples of the TIT profile generated by the present shape functions. Additionally, Fig. 5.3 shows that the shape function is capable of representing the arbitrary generated TIT profiles by experiment [85].

The pattern factor should have a low value between 0.05 and 0.15. [86] Additionally, maximum temperature is recommended to appear at the 2/3 span location because of the stress concentrated on the hub. Taking these into account, probabilistic density functions (PDF) for P and r_{max} are determined. The type of PDF for P is the Gaussian distribution function, and the Gumbel distribution, also known as extreme value distribution, is selected for the PDF of r_{max}. Variation of

each PDF is determined to satisfy the requirement that 99.9% of events occur within the range. Parameters to determine the form of PDF are listed in Table 5.4.

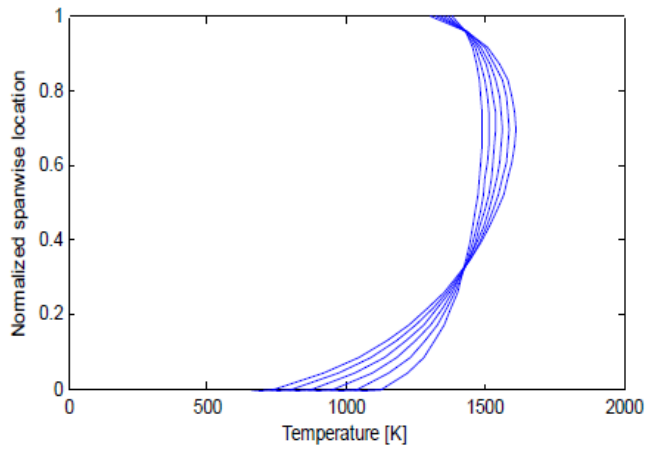

(a) P=0.05, 0.07, 0.09, 0.11, 0.13, 0.15 (r_{max}=0.7, T_{avg}=1420K)

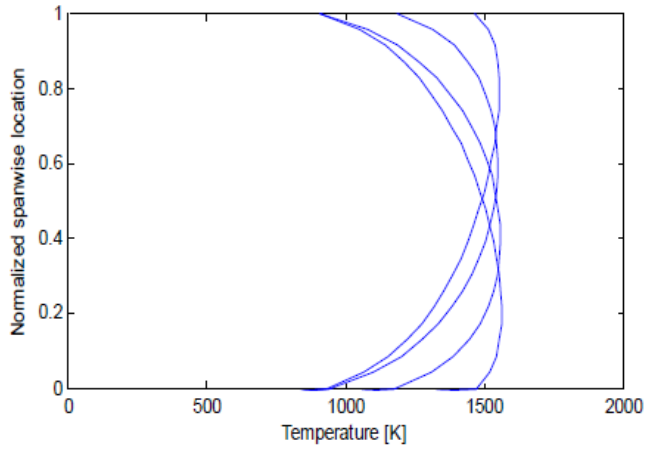

(b) r_{max}=0.2, 0.4, 0.6, 0.8 (P=0.1, T_{avg}=1420K)

Fig. 5.2 TIT profile generated by the shape function

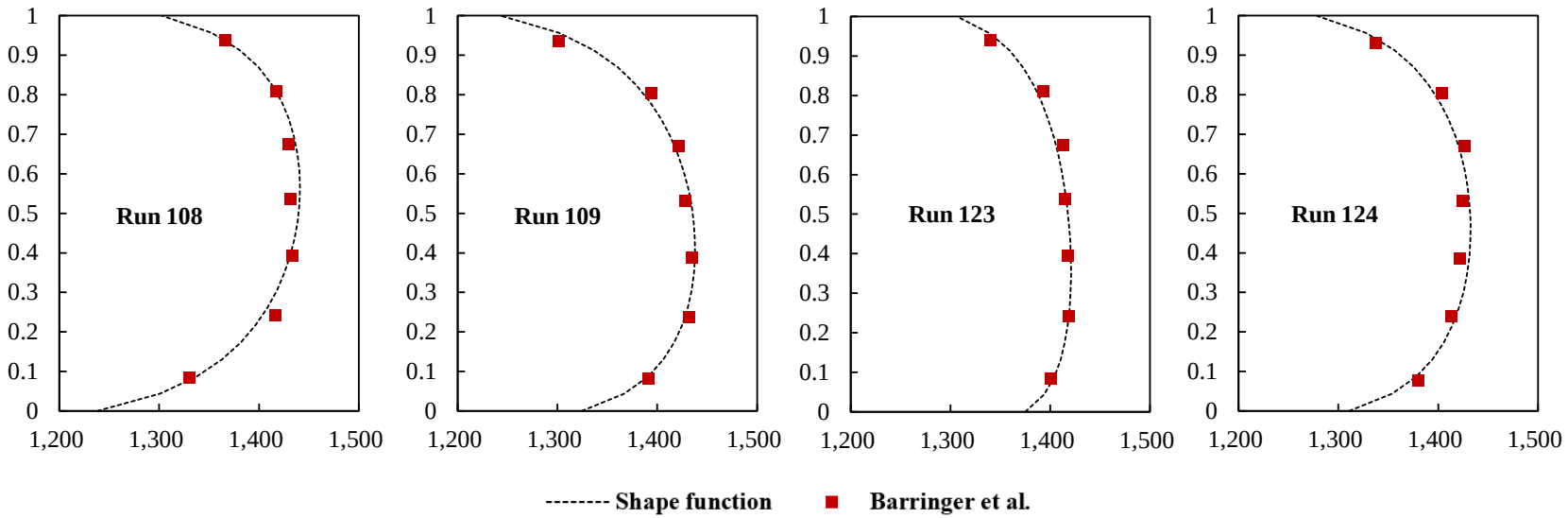

Fig. 5.3 TIT profile generated by the shape function

Table 5.4 Related factors for PDF of TIT distortion

	Pattern factor (PF)	Bias factor (r_{max})
Mean (E)	0.1000	0.6667
Variance (σ)	0.0162	0.1204
Range	0.05~0.15	0.1~0.9
PDF type	Gaussian distribution 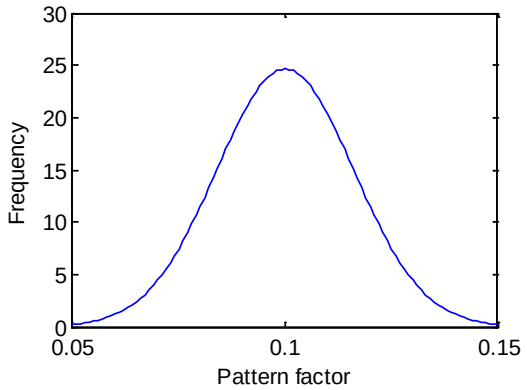	Gumbel distribution 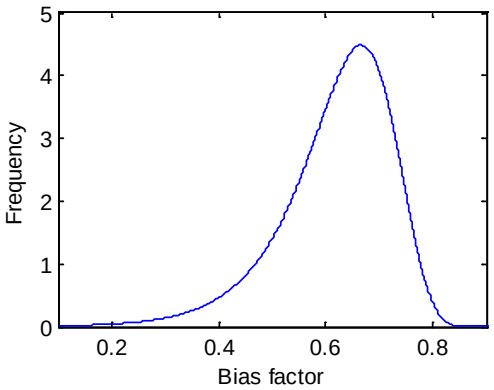

Chapter 6. Robust design optimization for the arrangement of film cooling holes

6.1 Problem definition

In this chapter, three separate robust design optimization studies will be performed. Each study considers three different uncertainties. Therefore, random variables corresponding to each uncertainty are additionally considered in addition to the DDO problem in Chapter 4.

The design variables used in the RDO cases are the same as in the DDO case, as listed in Table 4.1. The performance of film cooling is assessed based on the average surface temperature on the nozzle pressure side. Because a weak trade-off relation between surface temperature variation and average temperature is observed in the DDO study, standard deviation of the surface temperature (T_{dev}) is not considered in the RDO cases.

Instead of the deterministic value of the wall temperature, expectation and standard deviation of average temperature are considered as design objectives. Thus, the RDO problem is inherently a multi-objective optimization problem.

Three constraints are imposed, two on the mass flow and one on $E(T_{avg})$. No constraint is imposed on $\sigma(T_{avg})$ because the solutions having $\sigma(T_{avg})$ larger than the baseline can also be the optimum if they have much smaller $E(T_{avg})$ than that of the baseline.

The Optimization problem is formulated as follows:

Objectives:

Min. $E(T_{avg})$

Min. $\sigma(T_{avg})$

where $T_{avg} = \frac{1}{A_{PS}} \iint_{A_{PS}} T_w(s) ds$

Constraints:

$E(T_{avg}) \leq E(T_{avg})_{base}$

$\dot{m}_{total\_base} \geq \dot{m}_{total}$

$\dot{m}_{hole\_base} \geq \dot{m}_{hole}$

Before the optimization, an adequate number of samplings for MCS should be determined. It can be different depending on the number of variables, and generally, a large number of variables requires a large number of samplings. The maximum number of random variables in this study is 4 for presenting manufacturing tolerance of the film hole; thus, MCS is made to be implemented with 4 random variables and different numbers of samplings–100, 1,000, 10,000, and 100,000—to find the most efficient number of samplings.

The averages of the expectation and standard deviation obtained by implementing MCS five times are shown in Fig. 6.1 according to the number of samplings. The average value of each parameter is presented as a relative value,

which is the difference from the value obtained with 100,000 samplings. The convergence criterion is set to 0.1°.

From the results, it is observed that the average expectations obtained by the MCS with both the random and descriptive sampling method converge after 1,000 samplings. However, the average standard deviation from the MCS with random sampling does not converge until the number of samplings reaches 100,000, whereas that of the MCS with descriptive sampling converges only after 1,000 samples. Hence, it is concluded that 1,000 samplings of MCS with descriptive sampling is sufficient. Because the number of populations and generations of GA are set to 80 and 120, respectively, 9,600,000 function evaluations are required in total to complete the optimization.

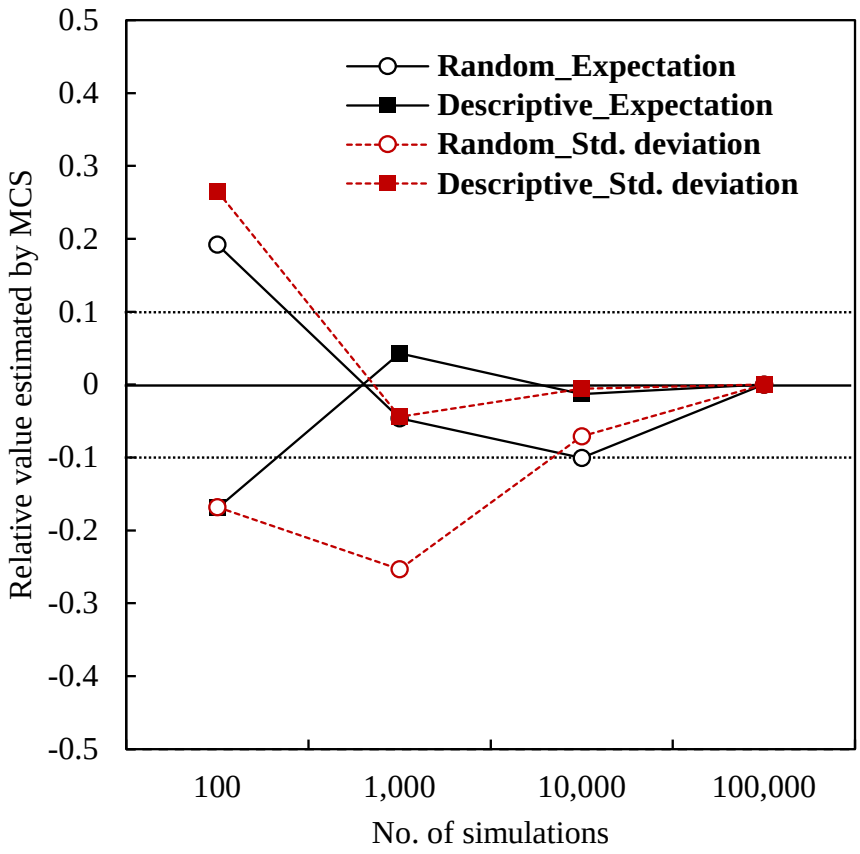

Fig. 6.1 MCS results according to the number of samplings

6.2 RDO results considering manufacturing tolerance

As described in Chapter 5.1 and Table 5.2, 4 random variables—SF0, SF1, SF2, and α_i—are considered to quantify the manufacturing tolerance of the film hole and 9 design variables are used to find the optimum shape of the array. 150 initial experimental points are selected for these 13 variables, and the initial Kriging model is constructed based on the computation results. After a five-fold refinement process and the addition of 100 sampling points to the initial samples, the average difference between the estimated and analyzed value of the additional sampling points falls below 3%. Therefore, the refinement process is terminated and the Pareto front shown in Fig. 6.2 is obtained using the converged models.

The solutions on the Pareto line are broadly categorized into 4 groups: group A, B, C and D. The arrays in group A exhibit a much lower $E(T_{avg})$ than that of the baseline but have a similar level of $\sigma(T_{avg})$ with respect to the baseline. The arrays in group B and C have an $E(T_{avg})$ that lies between the baseline and group A. Additionally, $\sigma(T_{avg})$ in groups B and C are much lower than those of the baseline and group A. The performances of these two groups are apparently similar, but they exhibit substantial differences in the configuration of ROW2. Arrays in group B have a curved shape for ROW2, whereas group C has a straight shape.

The arrays in group D have a similar $E(T_{avg})$ to the baseline but are much more insensitive than the baseline. The arrays in group D appear to have no relation with the other groups and are very different from each other, even in the same group. Additionally, they are distributed very sparsely on the Pareto line. It is

supposed that the difference of $\sigma(T_{avg})$ of the solutions in the region from the end of group B and C to group D is within the error range of the MCS. Moreover, because the performance of the solutions in the region of group D is robust to the tolerance, the configuration of the array should be modified substantially to change the expectation of the performance. Therefore, solutions in group D are less reliable than the others as an optimum.

For these reasons, except for group D, the representative points in each group were selected in the feasible region and validated using CFD. MCS was re-implemented after the validation results were added to the sampling set for the Kriging model. The re-calculated MCS results of the representative optimum points are also presented in Fig. 6.2, denoted by a cross. Note that they are located close to the Pareto line and estimated value, which is denoted by a red triangle.

Table 6.1 summarizes the comparison of the objective functions between the baseline and the three representative optimum points. The optimum points are named OPT-MT1, OPT-MT2, and OPT-MT3, and the design variables for each array configuration are listed in Table 6.2.

For the first objective, $E(T_{avg})$ is reduced at all optimum points, from a minimum of 5.4% to a maximum of 7.7%; for the second objective, $\sigma(T_{avg})$ is reduced at OPT-MT2 and OPT-MT3, by 58.67% and 62.53%, respectively. However, OPT-MT1 has a 4.22% higher $\sigma(T_{avg})$ than the baseline because of the numerical error of the Kriging models.

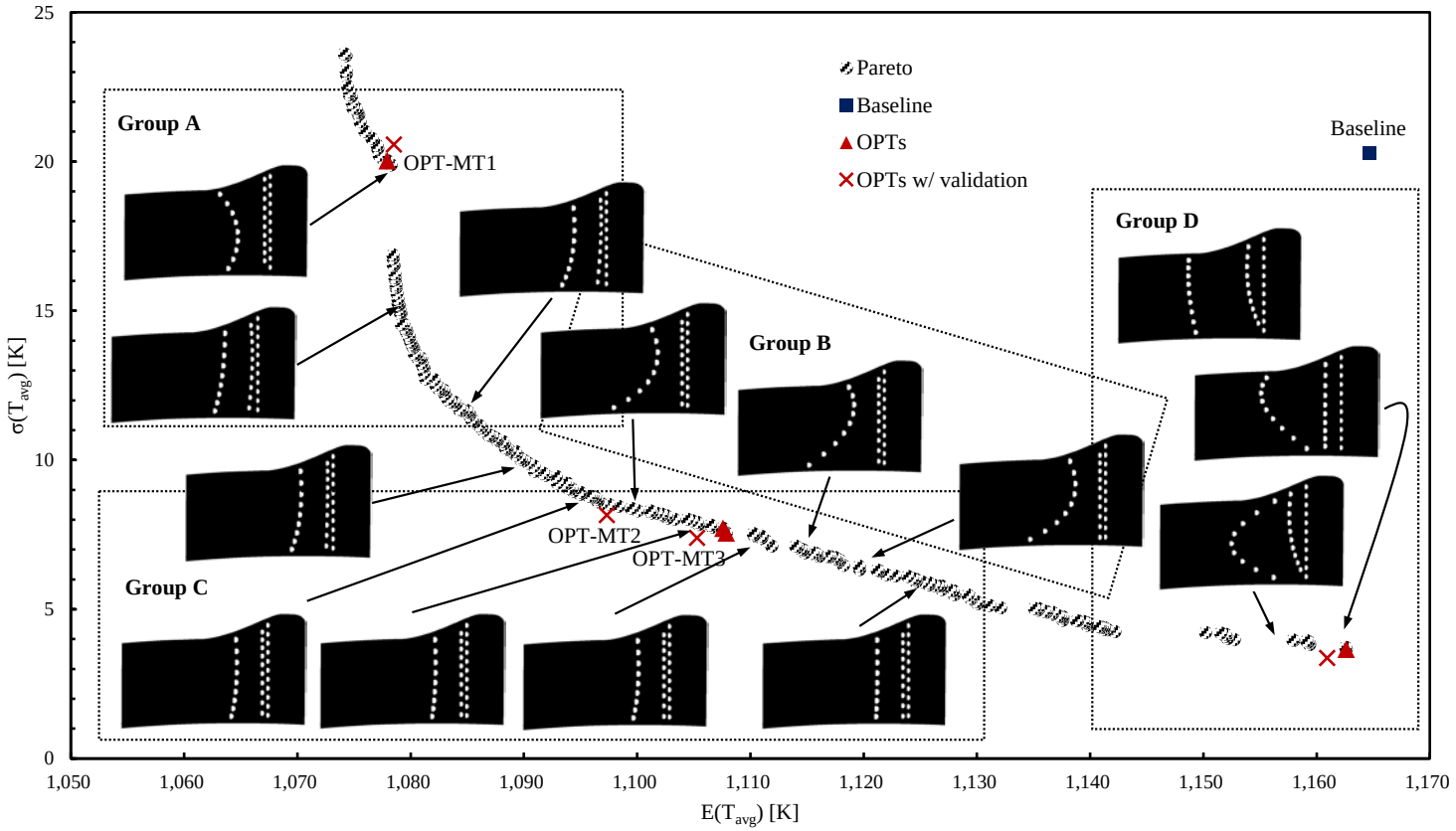

Fig. 6.2 Pareto front and optimum configurations obtained under consideration of manufacturing tolerance

Table 6.1 Optimization results under consideration of manufacturing tolerance

	$E(T_{avg})$ [K]	$\sigma(T_{avg})$ [K]
Baseline	1168.01	19.74
OPT-MT1	1078.51 (-7.66%)	20.57 (+4.22%)
OPT-MT2	1097.31 (-6.05%)	8.16 (-58.67%)
OPT-MT3	1105.28 (-5.37%)	7.40 (-62.53%)

Table 6.2 Design variables of the optima obtained under consideration of the manufacturing tolerance

Design Variable	Baseline	OPT-MT1	OPT-MT2	OPT-MT3
R_1x	0.252	0.183	0.183	0.183
R_1y	0	0.851	-0.555	-0.595
R_1g	0	0.186	0.994	1.000
R_1c	0	0.506	0.998	0.988
R_1s	0	0.225	-0.500	-0.497
R_2x	0.666	0.463	0.404	0.647
R_2g	0	-0.252	0.896	0.900
R_2c	0	0.895	0.898	0.899
R_2s	0	-0.018	0.477	0.402

6.3 RDO results considering variance of blowing ratio

As described in Chapter 5.2 and Table 5.3, 2 random variables—M#1 and M#2—are considered to quantify the variance of the blowing ratio, while 9 design variables are used to find the optimum shape of the array. A total of 96 initial experimental points are selected for these 11 variables, and an initial Kriging model is constructed based on the results. After repeating the refinement process 19 times and adding 76 sampling points to the initial samples, the average difference between the estimated and analyzed value of the additional sampling points falls below 3%. Therefore, the refinement process is terminated and the Pareto front shown in Fig. 6.3 is obtained using the converged models.

The solutions obtained in Chapter 6.2 consist of a mixed combination of various array configurations; even close solutions have different configurations. Therefore, they are categorized into four groups for detailed discussion. Compared to that, optimum solutions obtained in this chapter have consistent configurations depending on the location on the Pareto line. Hence, three optimum points below are selected as representative optimum points and named as OPT-BR1, OPT-BR2, and OPT-BR3.

OPT-BR1 Min. $E(T_{avg})$

OPT-BR2 Min. $(E(T_{avg}) + \sigma(T_{avg}))$

OPT-BR3 Min. $\sigma(T_{avg})$

The configurations of the three optima are also shown in Fig. 6.3; corresponding design variables are listed in Table 6.4. Optimum points are analyzed using CFD and the results are added to the converged DOE set. MCS for each optimum is re-implemented with the modified DOE set; the results are denoted by a cross mark in the same figure. They appear far from the original points, which are presented as triangle marks but are still located close to the Pareto line.

Table 6.3 summarizes the objective functions of the optimum points. The first objective function, $E(T_{avg})$, is reduced in all cases by approximately 5%. The second objective function, $\sigma(T_{avg})$, is reduced from 31.91% to 55.34%.

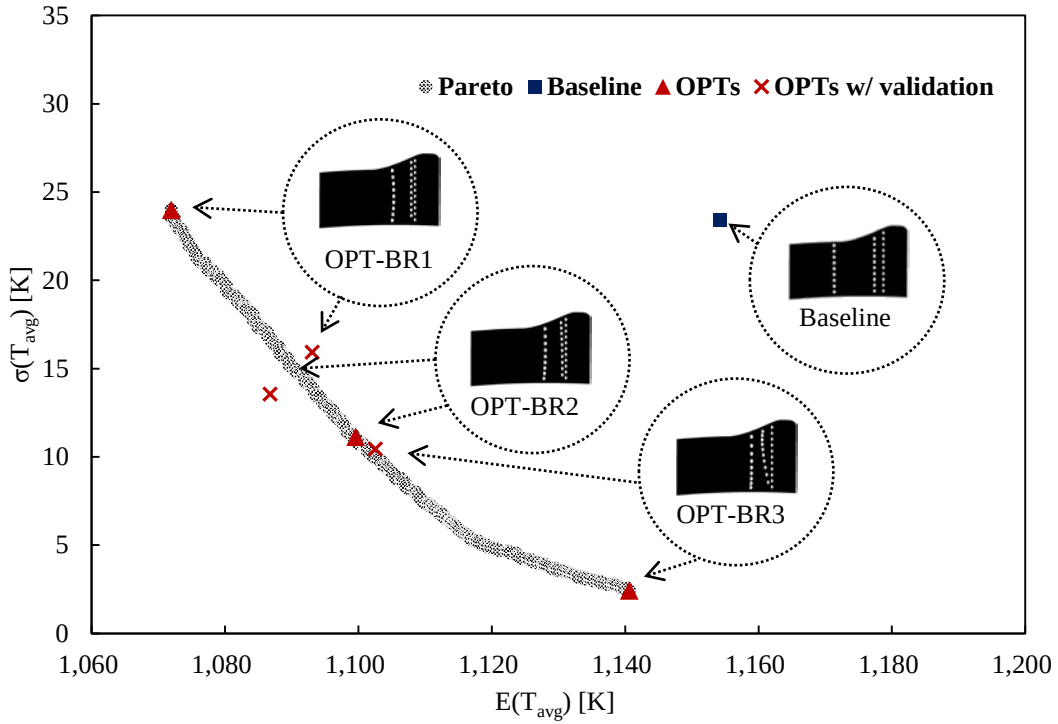

Fig. 6.3 Pareto front and optimum configurations obtained under consideration of variance of the blowing ratio

Table 6.3 Optimization results under consideration of variation of blowing ratio

	$E(T_{avg})$ [K]	$\sigma(T_{avg})$ [K]
Baseline	1154.277	20.34
OPT-BR1	1093.06 (-5.30%)	15.92 (-31.91%)
OPT-BR2	1086.77 (-5.85%)	13.54 (-42.09%)
OPT-BR3	1102.52 (-4.48%)	10.44 (-55.34%)

Table 6.4 Design variables of the optima obtained under consideration of the variance of blowing ratio

Design Variable	Baseline	OPT-BR1	OPT-BR2	OPT-BR3
R_1x	0.25	0.185	0.183	0.183
R_1y	0	0.987	0.403	0.841
R_1g	0	-0.847	-0.198	0.658
R_1c	0	-0.682	0.658	0.573
R_1s	0	-0.993	-0.290	0.058
R_2x	0.67	0.393	0.405	0.411
R_2g	0	0.997	0.712	0.025
R_2c	0	0.879	0.739	0.702
R_2s	0	0.999	0.495	0.084

6.4 RDO considering TIT distortion

As described in Chapter 5.3 and Table 5.4, 2 random variables—P and r_{max}—are considered to quantify the variance of the blowing ratio, while 9 design variables are used to find the optimum shape of the array. A total of 122 initial experimental points are selected for these 11 variables, and an initial Kriging model is constructed based on the computation results. After being refined once, 4 sampling points are added to the initial sampling points and the refinement process is terminated. The Pareto front shown in Fig. 6.4 is obtained using the converged Kriging models.

The representative optimum points below are selected on the Pareto line, similar to that in Chapter 6.3.

OPT-TIT1 Min. $E(T_{avg})$

OPT-TIT2 Min. $(E(T_{avg}) + \sigma(T_{avg}))$

OPT-TIT3 Min. $\sigma(T_{avg})$

The configurations of the three optima are also shown in Fig. 6.4; corresponding design variables are listed in Table 6.6. Optimum points are analyzed using CFD and the results are added to the converged DOE set. MCS for each optimum is re-implemented with the modified DOE set; the results are denoted by a cross mark in the same figure. These validation points are close to the original points, with less than 1% of difference in both $E(T_{avg})$ and $\sigma(T_{avg})$, compared to the original

points.

Table 6.5 summarizes the objective functions of the optimum points. The first objective function, $E(T_{avg})$, is reduced from 2.41% to 8.54%. The second objective function, $\sigma(T_{avg})$, is also reduced, but the values themselves in both optima and the baseline are so small that the absolute difference is nearly negligible.

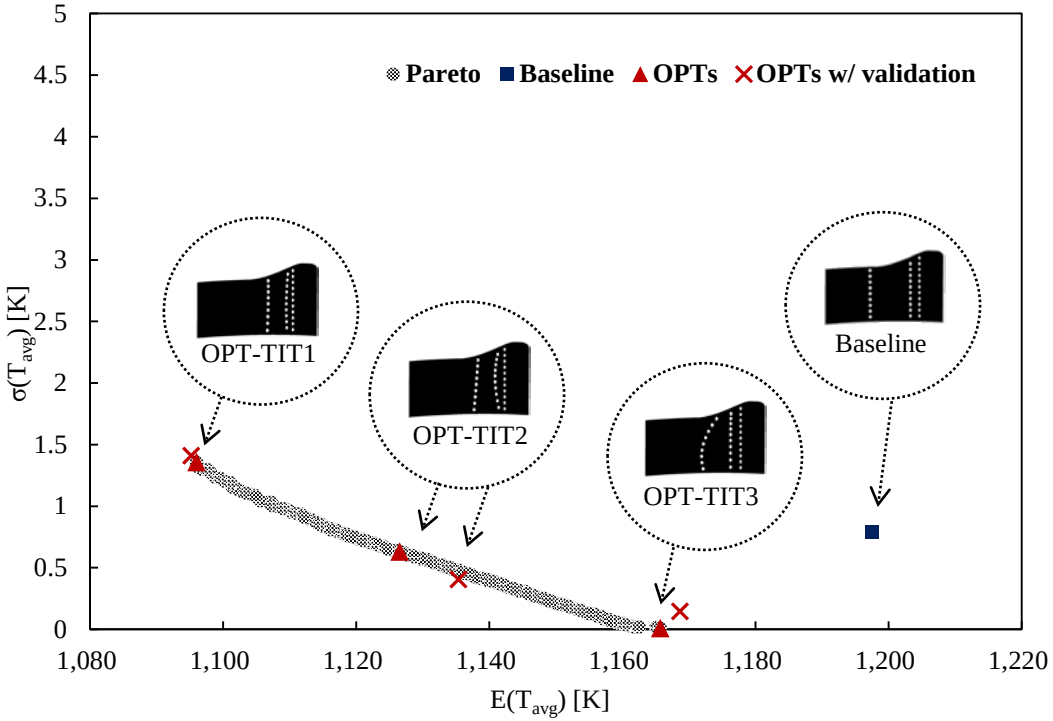

Fig. 6.4 Pareto front and optimum configurations obtained under consideration of TIT distortion

Table 6.5 Optimization results under consideration of distortion of TIT

	$E(T_{avg})$ [K]	$\sigma(T_{avg})$ [K]
Baseline	1197.51	0.79
OPT-TIT1	1095.22	1.41
	(-8.54%)	(+78.06%)
OPT-TIT2	1135.39	0.40
	(-5.19%)	(-48.95%)
OPT-TIT3	1168.65	0.14
	(-2.41%)	(-81.71%)

Table 6.6 Design variables of the optima obtained under consideration of the TIT distortion

Design Variable	Baseline	OPT-TIT1	OPT-TIT2	OPT-TIT3
R_1x	0.25	0.215	0.213	0.264
R_1y	0	0.325	-0.050	0.314
R_1g	0	0.438	-0.238	0.073
R_1c	0	-0.217	-0.835	-0.756
R_1s	0	-0.073	-0.449	-0.614
R_2x	0.67	0.443	0.494	0.561
R_2g	0	0.176	0.385	0.778
R_2c	0	0.087	0.026	-0.367
R_2s	0	-0.384	-0.132	-0.013

6.5 Comparison of the results

For the sake of convenient discussion, each robust optimization case is named as follows.

Case1 optimization case considering manufacturing tolerance

Case2 optimization case considering variance of blowing ratio

Case3 optimization case considering TIT distortion

6.5.1 Pareto front

The most noteworthy feature in Fig. 6.2~6.4 is that the Pareto line obtained by optimization Case3 appeared in a much smaller area than in other cases. (Note that the y-axis range of the graph in Fig. 6.4 is 5~7 times smaller than those in Fig. 6.2 and 6.3.) In other words, the variance of T_{avg} by TIT is much smaller than those by other uncertainties. TIT is known as the key resource that raises the uncertainty in turbine life expectation. However, it is confirmed from the results that TIT has only a weak impact on adiabatic film cooling effectiveness. As shown in eq. 4.8, the film cooling effectiveness is obtained from the temperature of cooling air and main flow. This means that film cooling effectiveness is nearly unchanged as long as the average temperature of TIT remains unchanged, though local film cooling performance can be altered.

6.5.2 Array configuration

Overall, all holes in the optimum array show the tendency to move upstream, especially ROW1 in OPT-MT1, OPT-MT2, OPT-MT3, and OPT-BR1, located in the upper limit of the design space. They are almost straight and have staggered position with respect to holes in ROW0.

Another notable feature in array configurations is the gradual change of the array in Case2. OPT-BR1 has three straight film hole arrays, of which ROW1 and ROW2 move forward to reach the boundary of the design space. The standard chordwise locations of ROW1 and ROW2 of OPT-BR2 and OPT-BR3 are unchanged from OPT-BR1, but holes are gradually clustered to the hub wall, and the space between the holes of ROW0 and ROW1 near the shroud increase, from OPT-BR1 to OPT-BR3.

Meanwhile, there is no consistent change in array shape in Case1 and 3. There are more random variables in Case1 than in the other cases, which leads to performance degradation of MCS. In other words, the Pareto solution obtained in Case1 has comparably large MCS error compared with the other cases. If there is no MCS error, setting aside other errors such as Kriging or CFD, solutions located close to each other on the Pareto line should have similar configurations.

In the case of robust optimization considering TIT distortion, it is obvious that the reason for inconsistency in array configurations comes from the fact that there is nearly no impact of TIT distortion on T_{avg} and that the solutions obtained only depend on $E(T_{avg})$.

6.5.3 Probability distribution

Figure 6.5 depicts the PDFs of optimum arrays obtained by all optimization cases. The distributions are obtained from the MCS with 100,000 samplings. Influence of the uncertainties can be confirmed by examining the dispersion of PDFs. Wide dispersion of the PDF indicates large influence of the uncertainty, while narrow dispersion of the PDF indicates the opposite. From this point of view, it can be said that the most influential uncertainty is manufacturing tolerance, followed by variance of blowing ratio and TIT distortion. These results coincide with the discussion in Chapter 6.5.1 and 6.5.2.

Aside from this relative dispersion of PDFs, PDFs from all cases show the same feature. Compared to the PDF of the baseline, all the distributions of the optima move to the left in the lower T_{avg} direction. The distribution of OPT1 shows the widest dispersion of the probability, even wider than that of the baseline. This implies that film cooling holes with the design of OPT1s show better performance than the baseline in most cases, but extremely poor performance could also be obtained at low probability. For example, in Fig. 6.5(b), T_{avg} could be over 1190 K in 0.1% probability with the OPT-BR1 design. On the other hand, the peak of the distribution of OPT-BR3 is 25%~30% higher than the others and the dispersion is notably narrow, which indicates the robustness of the performance. However, the expectation of the performance is approximately 70 K (5.9%) lower than that of OPT-BR1. OPT-BR2 shows intermediate characteristics of OPT-BR1 and OPT-BR3.

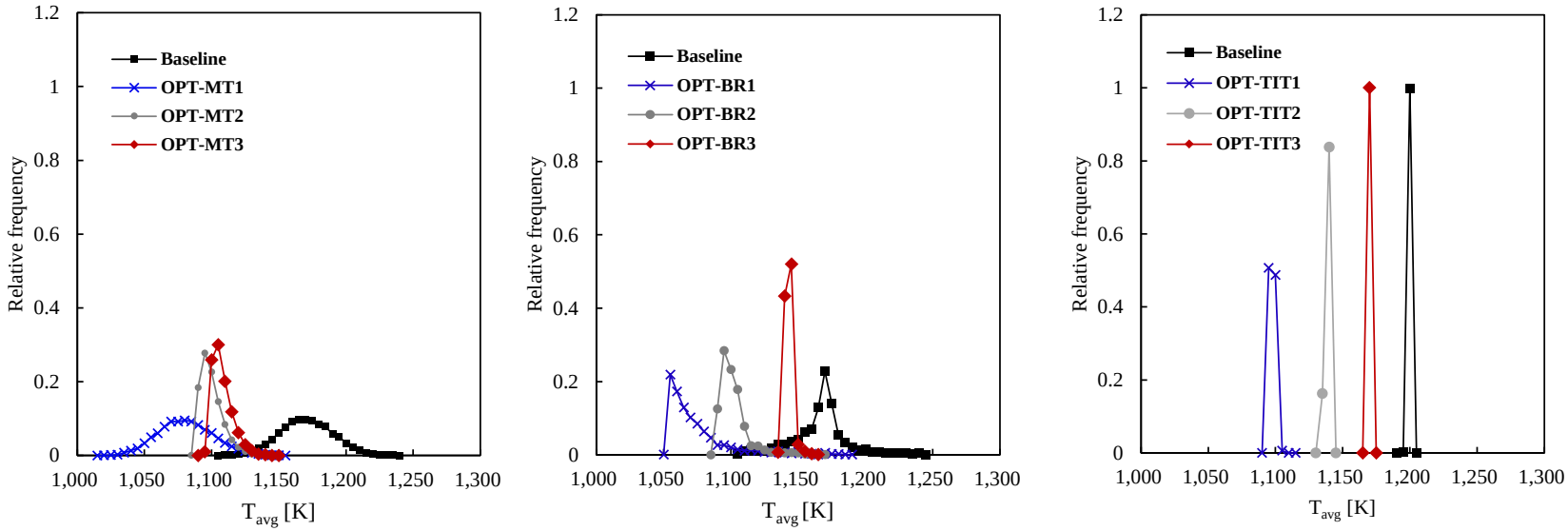

(a) manufacturing tolerance **(b) blowing ratio** **(c) TIT**

Fig. 6.5 Probabilistic distribution of optimum arrays obtained under consideration of uncertainties

To investigate the influence of each random variable in all optimization cases, the baseline and optimum arrays will be analyzed with various values of random variables.

Because there are more random variables in optimization Case1 than in the other cases, more sensitive ones among them are selected for the sake of efficient discussion. To this end, MCS is performed for the baseline and the optima obtained by Case1 with each random variable—SF0, SF1, SF2 and α_i. PDFs from the results are given in Fig. 6.6.

For the baseline, the influences apparently decrease in the order of α_i, SF0, SF1, and SF2. In the case of OPT-MT1, SF0 has an evident impact on the performance, but the influences of other tolerance factors remain at approximately the same level. OPT-MT2 and OPT-MT3 have similar forms of distribution, and even the effects on the performance of each tolerance factor are similar. From these results, it is confirmed that the most influential tolerance factors are injection angle (α_i) and scaling factor for the holes in ROW0 (SF0). It can be interpreted that the injection angle has a significant influence on the overall cooling performance because it controls three rows of the holes, whereas the other uncertainties control only a single row of the holes.

For this reason, further investigations of the influence of each random variable are performed for Case1 with SF0 and α_i, Case2 with M#1 and M#2, and Case3 with P and r_{max}.

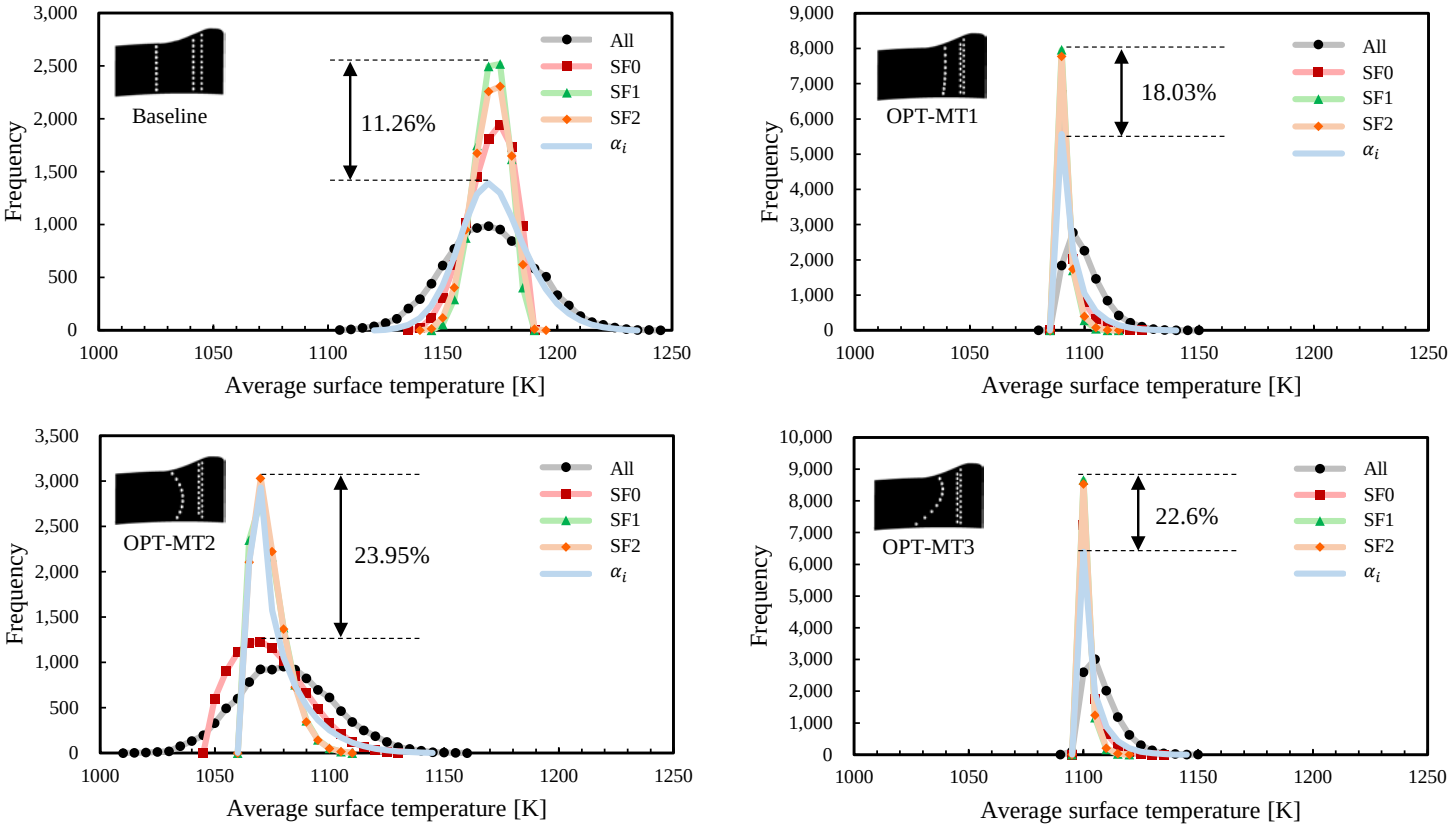

Fig. 6.6 Probability distribution according to the respective manufacturing tolerance

6.5.4 Film cooling effectiveness

For Case1, the baseline and OPT-MT2 are analyzed under the conditions of α_i =-3° and +3°, while OPT-MT1 and OPT-MT2 are analyzed under the conditions of SF0=0.9 and 1.1. For Case2, the baseline and OPT-BR2 are analyzed under the conditions of M#1=0.7, M#1=1.3, M#2=0.7 and M#2=1.3. For Case3, the baseline and OPT-TIT2 are analyzed under the conditions of P=0.05, P=0.15, r_{max}=0.1 and r_{max}=0.9. Figure 6.7~6.9 show the film cooling effectiveness contours.

Prior to the discussion of Fig. 6.7 for optimization Case1, variation of film hole shape according to manufacturing factors should be addressed first. This is because the hole shape itself is altered only in Case1.

Figure 6.10 shows the change of the inlet and exit shape of the film hole when the tolerance is intentionally applied. The hole exit is affected more notably than the inlet and both the relative position and area are affected. This finding implies that the properties of the coolant, such as momentum or mass rate, could be altered by the tolerance. When α_i =27°, the exit area increases by 21.2% from the original shape; when α_i =33°, the exit area decreases by 15.0% from the original shape. Furthermore, the exit area changes according to the change of SF0 from –6.4% to +7.0% of the original shape, relatively less than the change from α_i .

From Fig. 6.7, it is readily seen that the uncooled area of the optima is notably reduced compared to the baseline because ROW1 moves upstream and is staggered to ROW0, which leads to a significant improvement of the film cooling effectiveness between ROW0 and ROW2. Additionally, it is confirmed that the

cases that have the tolerance of low injection angle and high scaling factor, which result in having an extended exit area, exhibit high film cooling effectiveness. It is widely known that as the injection angle decreases, the cooling performance improves, whereas manufacturability and structural safety become worse; additionally, the cooling air ejected from the widened hole exit spreads more broadly but loses its momentum more easily. In this case, mass flow variance could also arise. To clarify the cause of the change of cooling performance according to the manufacturing tolerance, the dependence of the mass flow change on the tolerance is examined in Fig. 6.11. First, it is noticed that the mass flow rate of the coolants, whether the total induced coolant or the coolant for film cooling, of OPT cases is less than that of the baseline by virtue of the constraint of the optimization problem.

Second, the variance of mass flow according to the change of α_i is insignificant compared to that of the change of SF0, which varies from -1.3% to +1.8% for total induced coolant and from -5.7% to +7.1% for coolant ejected from the holes. Even the modified hole for SF0 is merely a row, whereas that for α_i is all three rows, and the change of the exit hole area of α_i (21.2%) is greater than that for SF0 (7.0%). This result implies that the performance improvement from the decrease of α_i is caused by the expansion of the hole exit area, which drives the coolant to spread more widely, whereas that from SF0 is caused by the increase of coolant mass flow. This relationship can also be observed in Fig. 6.10, the baseline and OPT-MT2 with α_i =27°, which indicates increased film cooling effectiveness

in the spanwise direction but little difference in the chordwise direction, compared to the baseline and OPT-MT2 with α_i=33°. It appears that ROW0 modified by SF0 exhibits a similar influence on the downstream region of all rows modified by α_i.

From the results, it is expected that the tolerance of the scaling factor will be more sensitive to the mass flow change of the cooling air than that of α_i. In other words, to restrict the mass flow rate of the coolant, the manufacturing factor relevant to the scaling factor should be handled more precisely than that relevant to the injection angle.

Change of film cooling effectiveness according to the blowing ratio is observed in Fig. 6.8. This subject has frequently been treated in many previous studies. The results shown in this study are not much different from those. On the concave curve of the nozzle pressure side, the cooling air is drawn to the surface more strongly. For this reason, the temperature (or film cooling effectiveness) difference from the nominal value is not easily dissipated but persists long enough to be overlapped as the flow sequentially passes the holes and approaches the trailing edge.

Variation in film cooling effectiveness according to the TIT profile is shown in Fig. 6.9. However, as already discussed above, there are no significant differences observed for the TIT profile.

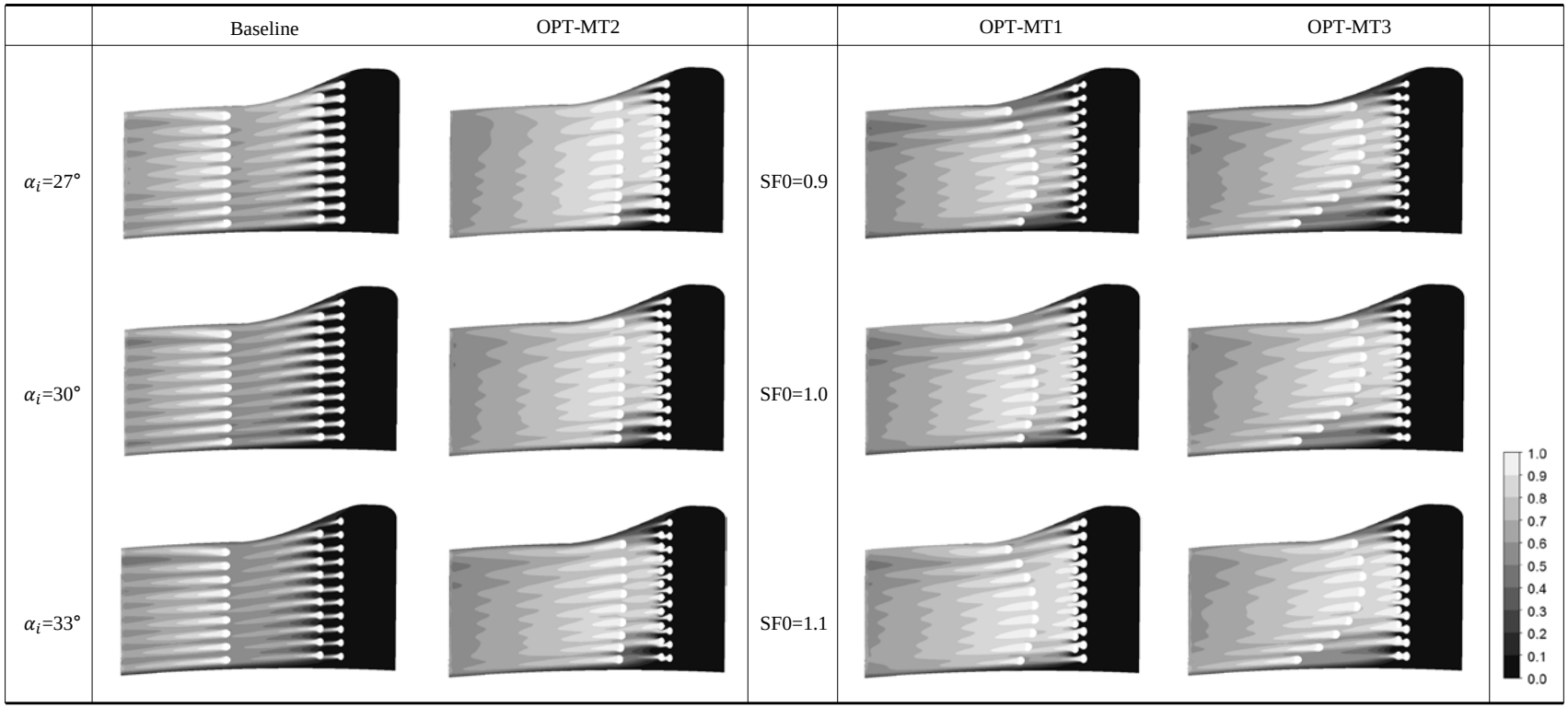

Fig. 6.7 Film cooling effectiveness contours according to the manufacturing tolerance

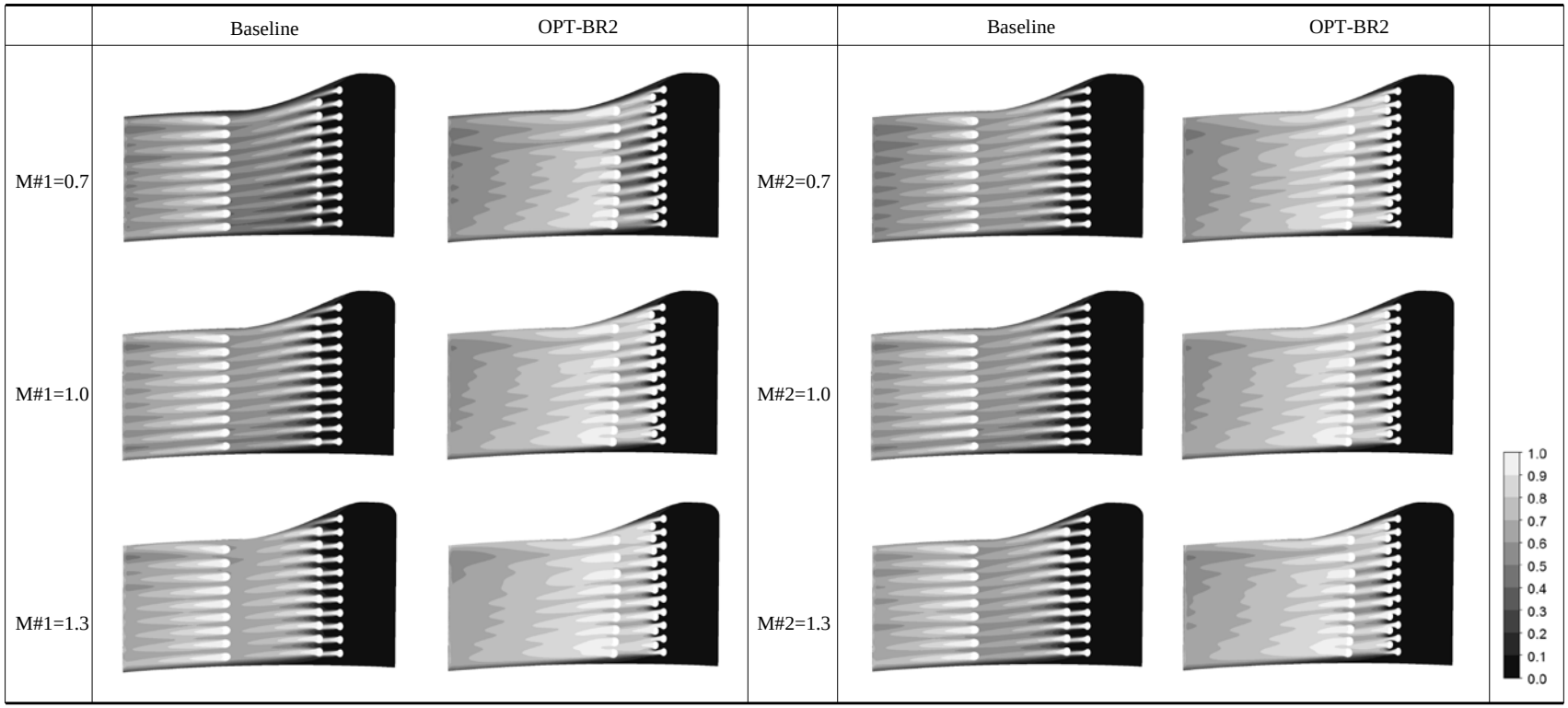

Fig. 6.8 Film cooling effectiveness contours according to the blowing ratio

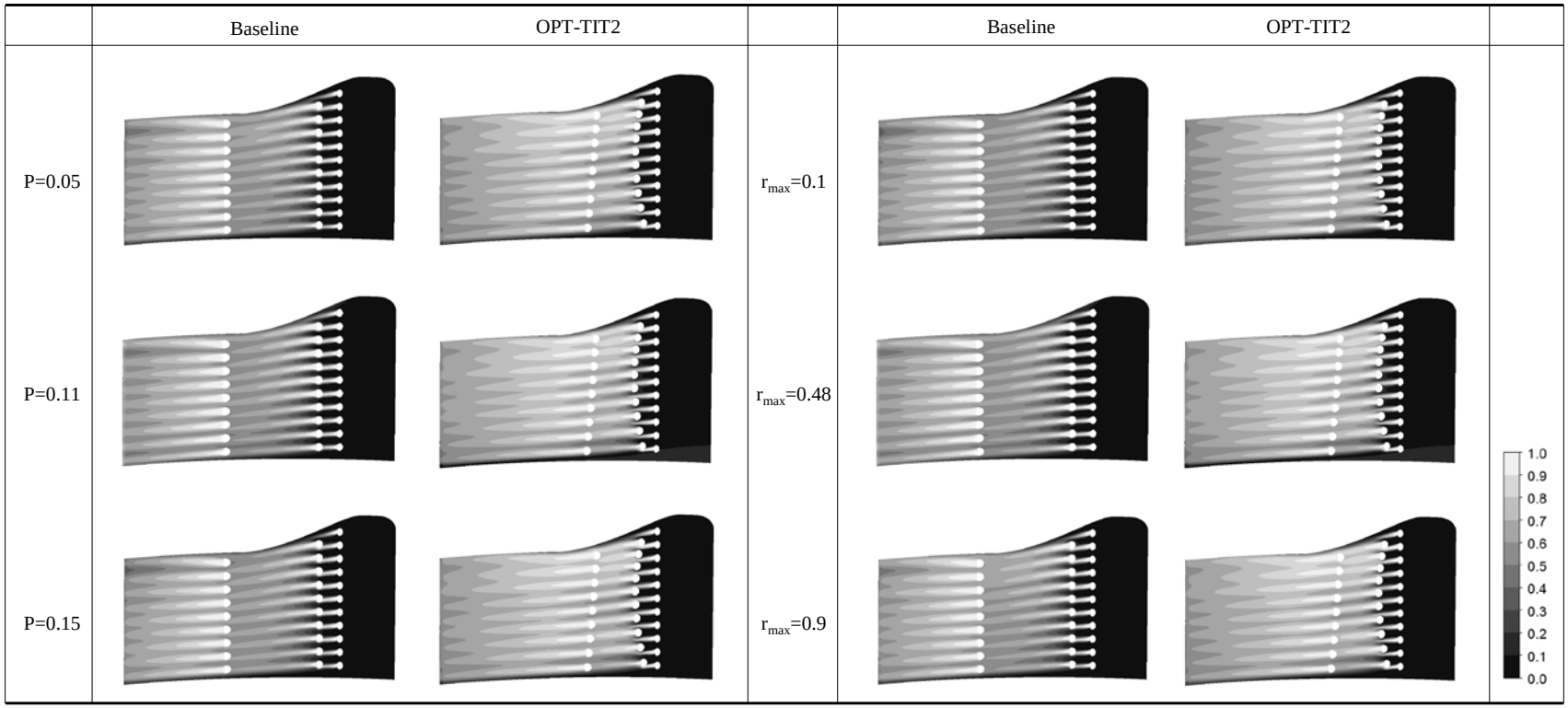

Fig. 6.9 Film cooling effectiveness contours according to the TIT profile

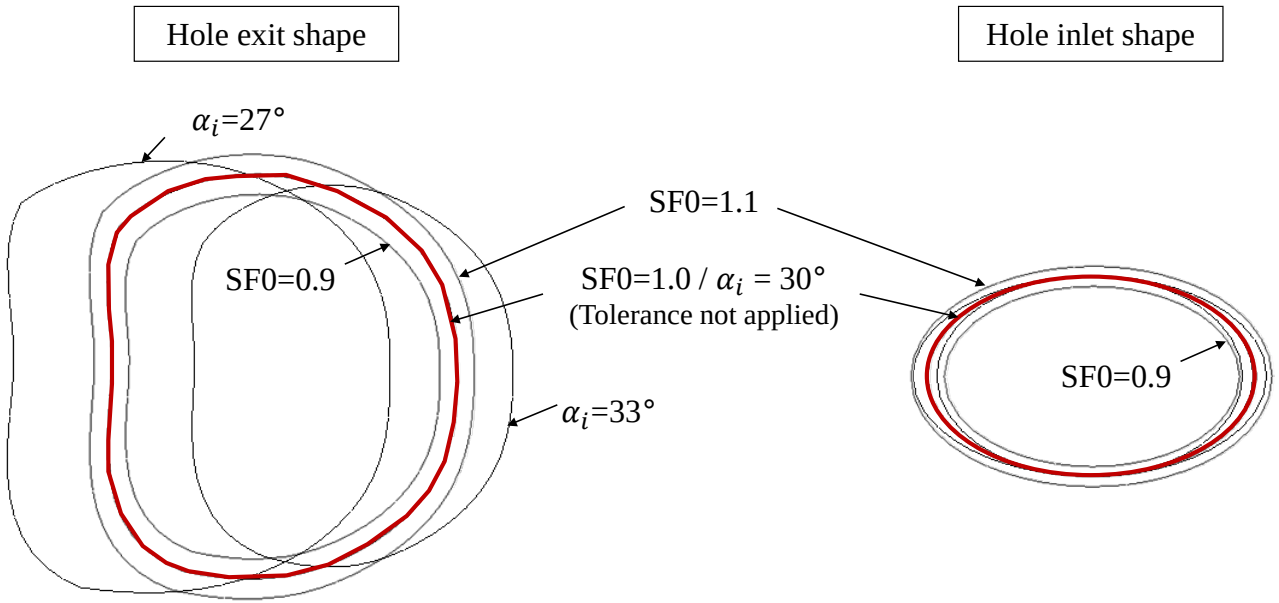

Fig. 6.10 Inlet and exit shape change of the hole according to the tolerance application

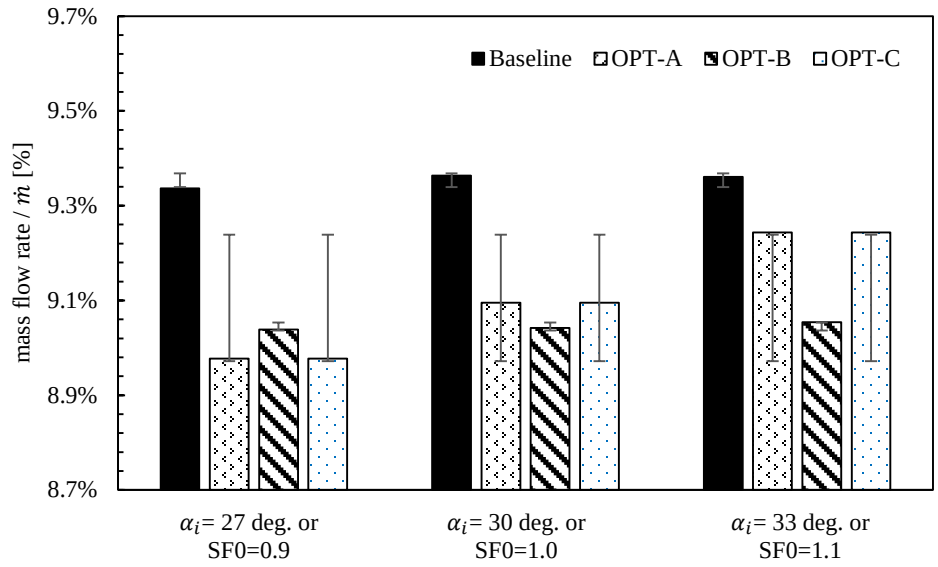

(a) Total induced cooling air ($\dot{m}_{total}$)

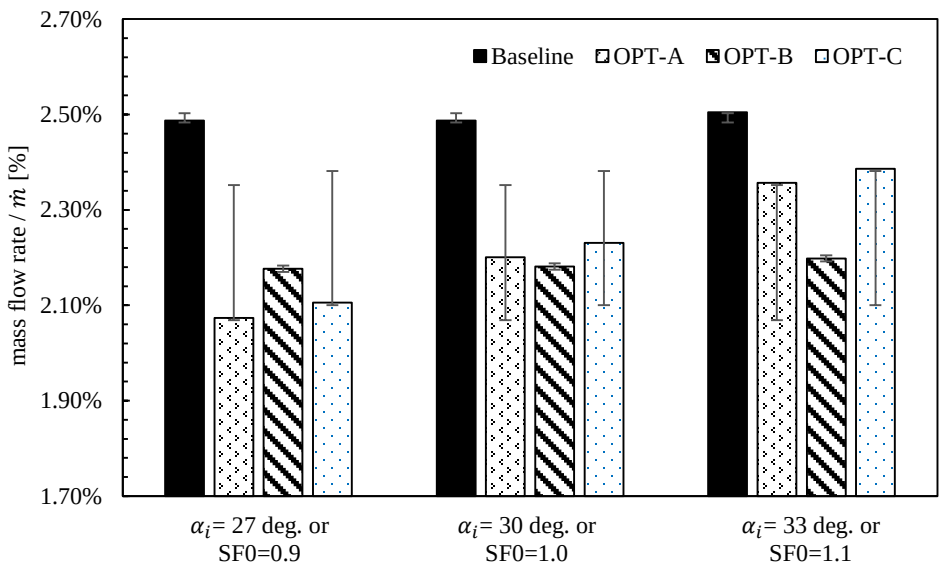

(b) Cooling air ejected from the holes ($\dot{m}_{hole}$)

Fig. 6.11 Mass flow change based on the tolerance application

To analyze the results in a quantitative manner, the spanwise-averaged film cooling effectiveness values of these 36 cases are comparatively shown in Fig. 6.12~14. The shaded region in the figures can be interpreted as a variation range according to the uncertainty. From these whole figures, it is clearly shown that the film cooling effectiveness and their variation range of optimum arrays is much higher and narrower than those of the baseline.

For optimization Case1, this is obviously shown in Fig. 6.12(a). Additionally, the trade-off relation between 2 objectives—expectation and variation—is observed in Fig. 6.12(b), which shows OPT-MT1 having higher film cooling effectiveness but wider variation range over the entire PS region compared with those of OPT-MT3.

In Fig. 6.13(a), film cooling effectiveness with baseline varies the most in the region between ROW1 and ROW3, while that region is reduced in the case of OPT-BR2. In Fig. 6.13(b), because only ROW2 is connected to the 2nd passage, the variation appears only after ROW2. It is obvious from these results that the variation of the mass flow of the 1st passage is more influential.

Meanwhile, in Fig. 6.14, the variation range by TIT is hardly observed in both optimum cases and the baseline, although the average film cooling effectiveness of the optimum increases, as in the other optimization cases.

Additionally, characteristics of the variation range show differences according to the uncertainties. Note that the variation according to variation of the blowing ratio gets increased or at least remains from the leading edge to the trailing edge.

Meanwhile, that according to the manufacturing tolerance gets decreased from upstream to downstream and hardly impacts the trailing edge.

From these results, it is confirmed that the upstream region is more sensitive to the manufacturing tolerance than the downstream region, which explains the considerable influence of the scaling factor of the holes in ROW0 (SF0). On the other hand, the downstream region is more sensitive to the variation of the blowing ratio than the upstream region, but most of the variation also comes from the change of the blowing ratio of the holes near the leading edge. In both cases, uncertainties in holes in the upstream region have more significant impacts on the film cooling performance. In other words, both manufacturing tolerance and flow conditions near the leading edge should be more precisely controlled than the other regions to minimize the performance variation of film cooling.

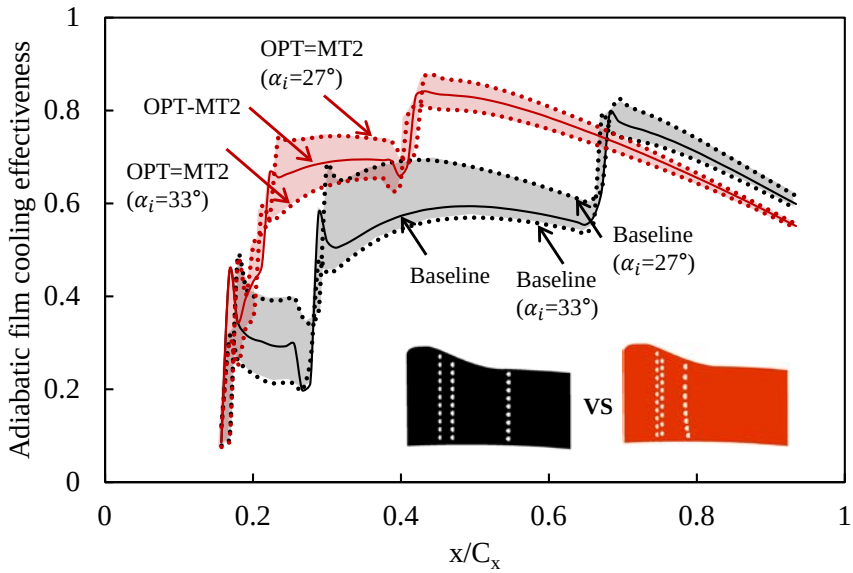

(a) by the injection angle (α_i)

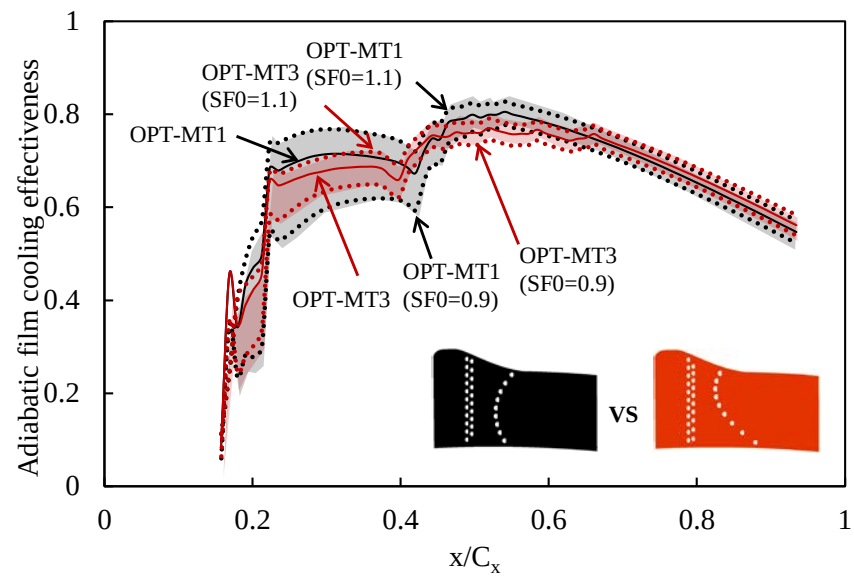

(b) by the scaling factor for the holes in ROW0 (SF0)

Fig. 6.12 Range of the film cooling effectiveness variation

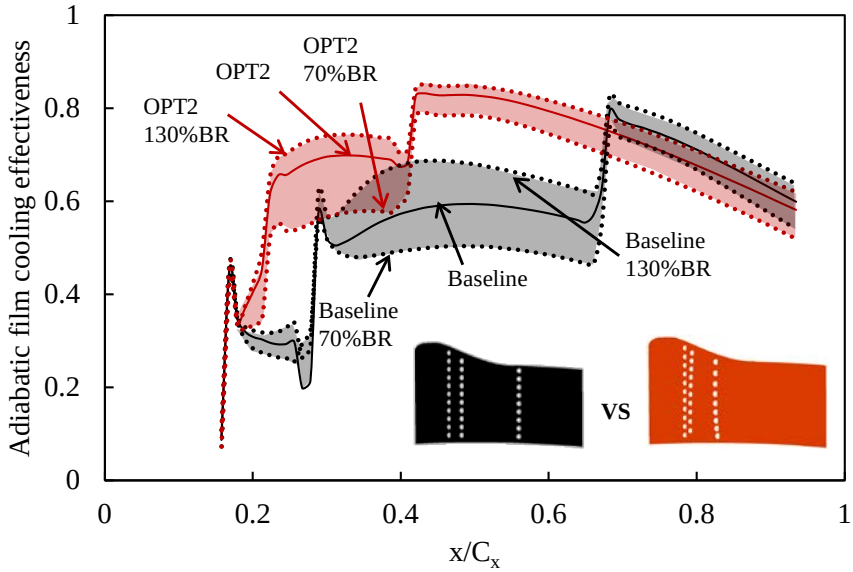

(a) by mass flow of the 1st cooling passage (M#1)

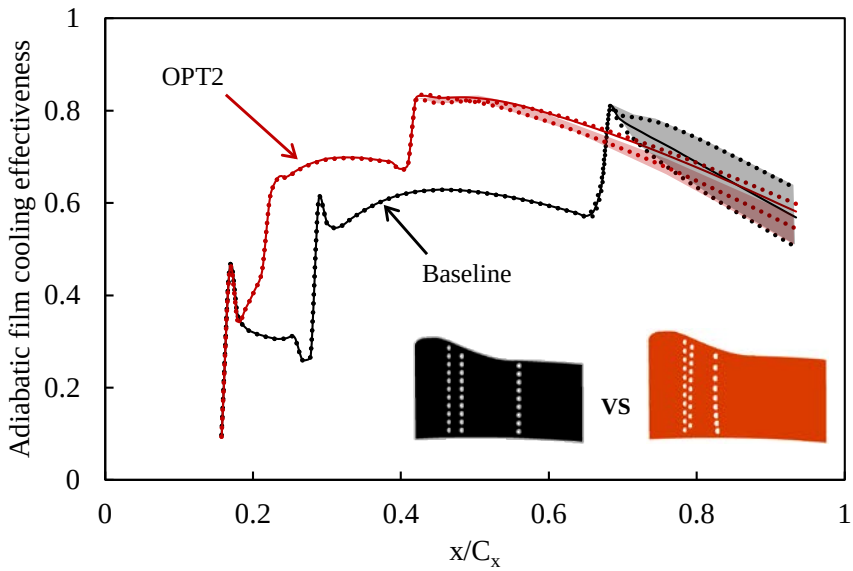

(b) by mass flow of the 2nd cooling passage (M#2)

Fig. 6.13 Range of the film cooling effectiveness variation

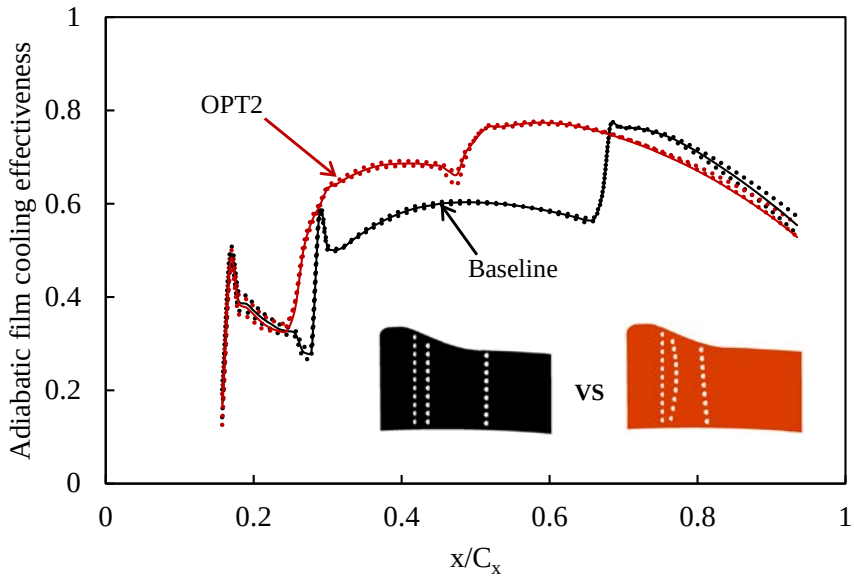

(a) by pattern factor (P)

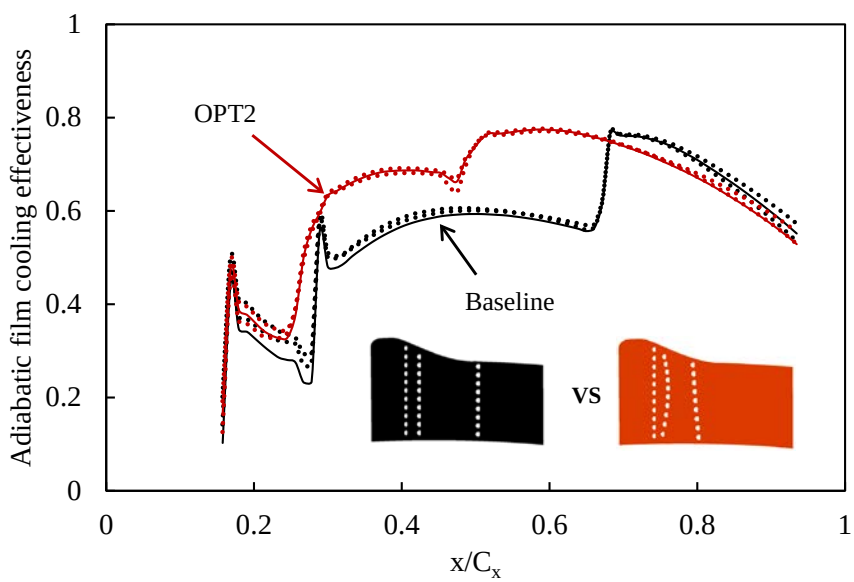

(b) by bias factor (r_{max})

Fig. 6.14 Range of the film cooling effectiveness variation

Chapter 7. Concluding remarks

7.1 Summary

Film cooling has been one of the most effective cooling techniques for gas turbine engines and has contributed to the significant increase of turbine inlet temperature. Over the past decade, research on film hole shape has been intensively focused and actively performed for improving the cooling performance; consequently, it has almost reached the limitation of improvement in the present day. Meanwhile, variation of the position of the holes has recently been paid more attention. Several optimization studies of that have been initiated to reap the benefit over modifying hole shape.

Because it started recently, there is still large room for further improvement of film hole array optimization. One of the most significant issues of this subject is the existence of uncertainties. HPT is highly loaded and exposed to strong temperature and thermal gradients; thus, the life of hot components could be affected even with small variations.

Thus, the present study attempted to improve turbine nozzle cooling performance by rearranging the locations of film holes, under consideration of uncertainties for TIT and the cooling system, which are known as key resources of the uncertainty.

To this end, first, the baseline nozzle model, a simplification of the reference nozzle model, is set to reduce the computational cost, and the array shape is

parameterized using a few parameters based on novel shape functions. By using these baseline model and parameterization methods, a deterministic design optimization study is performed prior to the robust design optimization study. The optimization results are validated by experiment and the effectiveness of numerical optimization method is validated.

Second, the probabilistic process consists of the Kriging surrogate model and MCS with the descriptive sampling method, which is coupled with the deterministic design optimization process using a GA. As a part of this process, three uncertainties in HPT are quantified by several random variables. Using this RDO process, three separate RDO studies with each uncertainty could be performed.

Thus, the following conclusions are reached:

First, an optimized yet robust film hole array configuration could be successfully obtained using the RDO process suggested in this study. Well-established robust optimization methods, including EGO, GA and MCS, are combined with quantified uncertainties. Manufacturing tolerance is quantified by 4 random variables, while blowing ratio and TIT are quantified by 2 random variables. Their probability density distributions and variation ranges are carefully determined by referring to published open literature. Cooling performance and robustness of the obtained optimum hole arrays are improved by a maximum of 7.66% and 62.53% under consideration of manufacturing tolerance, by 5.30% and 55.34% under consideration of the variance of the blowing ratio, and by 8.54% and 81.74% under

consideration of the variance of the TIT profile.

Second, characteristics of uncertainties and the film hole array configuration are understood. The optimized film hole arrays seem to show inconsistent configurations, but several features of those are also caught. For example, optimized film hole arrays are disposed on the upstream region, and in most of the optimum arrays, holes in the second array have a staggered position with respect to the prepositive holes. Additionally, from the Pareto line and probabilistic assessment of the optimum arrays, it is confirmed that the influence of variance is significant with the sequence of manufacturing tolerance, blowing ratio, and TIT. Although unpredictability of TIT is a widely known major source of uncertainty in HPT, it shows weak impacts on adiabatic film cooling effectiveness.

Lastly, the effects of uncertainties on the nozzle surface are analyzed. It is found that the influence of manufacturing tolerance gradually decreases toward the trailing edge, while that of variance of the blowing ratio increases or remains. Additionally, film cooling performance exhibits more sensitive behavior to random variables related to the holes near the leading edge, e.g., extension/contraction ratio of the film hole core for film holes closest to the leading edge and blowing ratio of the film holes connected to the cooling passage near the leading edge.

7.2 Future work

In this study, the arrangement of film holes is successfully optimized while considering major uncertainties in HPT. However, there is still room for practical usage of the optimized film hole array because this subject is in the early stage of research.

First, the uncertainties considered in the study are quantified by referring to published open literature because the actual field data are hard to access. However, there has not been enough research regarding the uncertainty quantification for HPT; thus, a large part of that in this study depends upon assumptions. For example, most of the PDFs of uncertainties are assumed as the Gaussian distribution because it is the most commonly observed probabilistic distribution in nature. If an elaborate quantification study for uncertainties or sufficient field data is combined with the RDO study, more practical results could be expected.

Second, all analyses in this study are performed under the adiabatic wall condition. In other words, only convection effects are considered and the conduction effects of internal cooling and film holes are ignored. To consider cooling effects by conduction, conjugated heat transfer analysis is required. This analysis method consumes much more time than that under the adiabatic wall condition. To address this problem, a high-power computing resource or advanced optimization scheme is required. With consideration of internal cooling effects, reliability of the results could be enhanced.

Lastly, there are many internal cooling components inside nozzles that are ignored

in the study. It is expected that with an advanced optimization scheme, they could also be simultaneously optimized with film holes. For example, there are variable fidelity optimization methods such as the hierarchical Kriging. By using this method, a high-fidelity Kriging model built based on insufficient samplings can be revised by an abundant number of samplings obtained using a low-fidelity yet low-cost solver, such as one-dimensional network heat transfer analysis. Attempts to optimize the external and internal cooling components simultaneously would encourage the practical usage of an optimization study.

References

[1] Sautner, M., Clouser, S., and Han, J. C., "Determination of surface heat transfer and film cooling effectiveness in unsteady wake flow conditions," AGARD CP, 527, East Hartford, 1992, pp. 6-1-6-12.

[2] Clifford, R. J., "Rotating heat transfer investigations on a multi-pass cooling geometry," AGARD CP, 390, 1985, pp. 2-1-2-12.

[3] Budugur, L. *Fluid dynamics and heat transfer of turbomachinery*: Wiley-VCH, 1996.

[4] Han, J.-C., Dutta, S., and Ekkad, S. *Gas turbine heat transfer and cooling technology, Second Edition*: CRC Press, 2012.

[5] Makki, Y. H., and Jakubowski, G. S., "An experimental study of film cooling from diffused trapezoidal shaped holes," AIAA/ASME 4th Joint Thermophysics and Heat Transfer Conference, Boston, MA, 1986.

[6] Schmidt, D. L., Sen, B., and Bogard, D. G., "Film cooling with compound angle holes: adiabatic effectiveness," Journal of Turbomachinery, Vol. 118, No. 4, 1996, pp. 807-813. doi: 10.1115/1.2840938

[7] Sen, B., Schmidt, D. L., and Bogard, D. G., "Film cooling with compound angle holes: heat transfer," Journal of Turbomachinery, Vol. 118, No. 4, 1996, pp. 800-806. doi: doi:10.1115/1.2840937

[8] Thole, K., Gritsch, M., Schulz, A., and Wittig, S., "Flowfield measurements for film cooling holes with expanded exits," ASME Turbo Expo, Paper 96-GT-174, Birmingham, UK, 1996.

[9] Haven, B. A., Yamagata, D. K., Kurosaka, M., Yamawaki, S., and Maya, T., "Anti-kidney pair of vortices in shaped holes and their influence on film cooling effectiveness," ASME Turbo Expo, Paper 97-GT-45, Orlando, 1997.

[10] Gritsch, M., Schulz, A., and Wittig, S., "Adiabatic wall effectiveness measurements of film-cooling holes with expanded exits," Journal of Turbomachinery, Vol. 120, No. 3, 1998, pp. 549-556.

[11] Gritsch, M., Schulz, A., and Wittig, S., "Heat transfer coefficient measurements of film-cooling holes with expanded exits," International Gas Turbine and Aeroengine Congress & Exhibition, 98-GT-028, Stockholm, Sweden, 1998.

[12] Kohli, A., and Thole, K. A., "Entrance effects on diffused film-cooling holes,"

International Gas Turbine and Aeroengine Congress and Exhibition, 98-GT-402, Stockholm, Sweden, 1998.

[13] Kohil, A., and Bogard, D. G., "Effects of hole shape on film cooling with large angle injection," International Gas Turbine & Aeroengine Congress & Exhibition, 99-GT-165, Indianapolis, Indiana, 1999.

[14] Reiss, H., and Bölcs, A., "Experimental study of showerhead cooling on a cylinder comparing several configurations using cylindrical and shaped holes," International Gas Turbine & Aeroengine Congress & Exhibition, Indianapolis, Indiana, 1999.

[15] Yu, Y., Yen, C.-H., Shih, T. I.-P., and Chyu, M. K., "Film cooling effectiveness and heat transfer coefficient distributions around diffusion shaped holes," International Gas Turbine & Aeroengine Congress & Exhibition, Paper 99-GT-34, lndianapohs, Indiana, 1999.

[16] Ganzert, W., Hildebrandt, T., and Fottner, L., "Systematic experimental and numerical investigations on the aerothermodynamics of a film cooled turbine cascade with variation of the cooling hole shape: Part I-Experimental approach," ASME Turbo Expo, 2000-GT-0295, Munich, Germany, 2000.

[17] Ganzert, W., Hildebrandt, T., and Fottner, L., "Systematic experimental and numerical investigations on the aerothermodynamics of a film cooled turbine cascade with variation of the cooling hole shape: Part II-Numerical approach," ASME Turbo Expo, 2000-GT-0298, Munich, Germany, 2000.

[18] Barthet, S., and Bario, F., "Experimental investigation of film cooling flow induced by shaped holes on a turbine blade," Annals of the New York Academy of Sciences, Vol. 934, 2001, pp. 313-320.

[19] Chen, P.-H., Hung, M.-S., and Ding, P.-P., "Film cooling performance on curved walls with compound angle hole configuration," Annals of the New York Academy of Sciences, Vol. 934, 2001, pp. 355-360.

[20] Sargison, J. E., Guo, S. M., Oldfield, M. L. G., and Rawlinson, A. J., "The variation of heat transfer coefficient, adiabatic effectiveness and aerodynamic loss with film cooling hole shape," Annals of the New York Academy of Sciences, Vol. 934, 2001, pp. 361-368.

[21] Saumweber, C., Schulz, A., Wittig, S., and Gritsch, M., "Effects of entrance crossflow directions to film cooling holes," Annals of the New York Academy of Sciences, Vol. 934, 2001, pp. 401-408.

[22] Takeishi, K.-I., and Aoki, S., "Contribution of heat transfer to turbine blades and vanes

for high temperature industrial gas turbines Part 1: Film cooling," Annals of the New York Academy of Sciences, Vol. 934, 2001, pp. 305-312.

[23] Yuen, C. H. N., Martinez-Botas, R. F., and Whitelaw, J. H., "Film cooling effectiveness downstream of compound and fan-shaped holes," ASME Turbo Expo, 2001-GT-0131, New Orleans, Louisiana, 2001.

[24] Dittmar, J., Schulz, A., and Wittig, S., "Assessment of various film cooling configurations including shaped and compound angle holes based on large scale experiments," ASME Turbo Expo, GT2002-30176, Amsterdam, The Netherlands, 2002.

[25] Ferguson, J. D., Leylek, J. H., and Buck, F. A., "Film cooling on a modern HP turbine blade: Part III-Axial Shaped Holes," ASME Turbo Expo, GT2002-30522, Amsterdam, The Netherlands, 2002.

[26] McGrath, E. L., Leylek, J. H., and Buck, F. A., "Film cooling on a modern HP turbine blade: Part IV-Compound-Angle Shaped Holes," ASME Turbo Expo, GT2002-30521, Amsterdam, The Netherlands, 2002.

[27] Bohn, D., Ren, J., and Kusterer, K., "Conjugate heat transfer analysis for film cooling configurations with different hole geometries," ASME Turbo Expo, GT2003-38369, Atlanta, Georgia, 2003.

[28] Saumweber, C., Schulz, A., and Wittig, S., "Free-stream turbulence effects on film cooling with shaped holes," Journal of Turbomachinery, Vol. 125, No. 1, 2003, p. 65.
doi: 10.1115/1.1515336

[29] Bunker, R. S., "A review of shaped hole turbine film-cooling technology," Journal of Heat Transfer, Vol. 127, No. 4, 2005, p. 441.
doi: 10.1115/1.1860562

[30] Saumweber, C., and Schulz, A., "Effect of geometry variations on the cooling performance of fan-shaped cooling holes," Journal of Turbomachinery, Vol. 134, No. 6, 2012, p. 061008.
doi: 10.1115/1.4006290

[31] Saumweber, C., and Schulz, A., "Free-stream effects on the cooling performance of cylindrical and fan-shaped cooling holes," Journal of Turbomachinery, Vol. 134, No. 6, 2012, p. 061007.
doi: 10.1115/1.4006287

[32] Liu, J. S., Malak, M. F., Tapia, L. A., Crites, D. C., Ramachandran, D., Srinivasan, B., Muthiah, G., and Venkataramanan, J., "Enhanced film cooling effectiveness with new

shaped holes," ASME TurboExpo, GT2010-22774, Glasgow, UK, 2010.

[33] Lu, Y., "Effect of hole configurations on film cooling from cylindrical Inclined holes for the application to gas turbine blades," Louisiana State University,Agricultural and Mechanical College, Louisiana State University,Ph. D Thesis, 2007.

[34] Kusterer, K., Elyas, A., Bohn, D., Sugimoto, T., Tanaka, R., and Kazari, M., "The nekomimi cooling technology: cooling holes with ears for high-efficient film cooling," ASME TurboExpo, GT2011-45524, Vancouver, British Columbia, Canada, 2011.

[35] Kusterer, K., Tekin, N., Bohn, K., Sugimoto, T., Tanaka, R., and Kazari, M., "Experimental and numerical investigations of the nekomimi film cooling technology," ASME TurboExpo, GT2012-68400, Copenhagen, Denmark, 2012.

[36] Ely, M. J., and jubran, B. A., "A numerical study on increasing film cooling effectiveness through the use of sister holes," ASME Turbo Expo, GT2008-50366, Berlin, Germany, 2008.

[37] Ely, M. J., and Jubran, B. A., "A numerical study on improving large angle film cooling performance through the use of sister holes," Numerical Heat Transfer, Part A: Applications, Vol. 55, No. 7, 2009, pp. 634-653.
doi: 10.1080/10407780902821532

[38] Khajehhasani, S., and Jubran, B. A., "Film cooling from circular and elliptical exit shaped holes with sister hole influence," ASME TurboExpo, GT2013-95138, San Antonio, Texas, USA, 2013.

[39] Lee, K.-D., Kim, S.-M., and Kim, K.-Y., "Numerical analysis of film-cooling performance and optimization for a novel shaped film-cooling hole," ASME Turbo Expo, GT2012-68529, Copenhagen, Denmark, 2012.

[40] Chi, Z., Li, X., Han, C., Ren, J., and Jiang, H., "Optimization of the hole exit shaping of film holes without and with compoind angles for maximal film cooling effectiveness," ASME TurboExpo, GT2014-25212, 2014.

[41] Nita, K., Okita, Y., Nakamata, C., Kubo, S., Yonekura, K., and Watanabe, O., "Film cooling hole shape optimization using proper orthogonal decomposition," ASME Turbo Expo, GT2014-27239, Dusseldorf, Germany, 2014.

[42] Saumweber, C., and Schulz, A., "Interactions of film cooling rows: effects of hole geometry and row spacing on the cooling performance downstream of the second row of holes," ASME Turbo Expo, GT2003-38195, Atlanta, Georgia, 2003.

[43] Lin, Y., Song, B., Li, B., and Liu, G., "Measured film cooling effectiveness of three

multihole patterns," Journal of Heat Transfer, Vol. 128, No. 2, 2006, p. 192.
doi: 10.1115/1.2137762

[44] Kusterer, K., Elyas, A., Bohn, D., Sugimoto, T., and Tanaka, R., "Double-jet film-cooling for highly efficient film-cooling with low blowing ratios," ASME TurboExpo, GT2008-50073, Berlin, Germany, 2008.

[45] Kusterer, K., Elyas, A., and Bohn, D., "Film cooling effectiveness comparison between shaped-and double jet film cooling holes in a row arrangement," ASME TurboExpo, GT2010-22604, Glasgow, UK, 2010.

[46] Lee, K.-D., Kim, S.-M., and Kim, K.-Y., "Multi-objective optimization of a row of film cooling holes using an evolutionary algorithm and surrogate modeling," Numerical Heat Transfer, Part A: Applications, Vol. 63, No. 8, 2013, pp. 623-641.
doi: 10.1080/10407782.2013.751316

[47] Johnson, J., King, P., Clark, J., and Ooten, M., "Design optimization methods for improving HPT vane pressure side cooling properties using genetic algorithms and efficient CFD," 50th AIAA Aerospace Sciences Meeting, 2012, pp. 4791-4809.

[48] Johnson, J. J., "Genetic algorithm optimization of a film cooling array on a modern turbine inlet vane," Air Force Institute of Technology,3542763, 2012, p. 375.

[49] Johnson, J. J., King, P. I., Clark, J. P., and Ooten, M. K., "Genetic algorithm optimization of a high-pressure turbine vane pressure side film cooling array," Journal of Turbomachinery, Vol. 136, No. 1, 2013, p. 011011.
doi: 10.1115/1.4023470

[50] Chi, Z., Liu, H., and Zang, S., "Semi-inverse design optimization method for film-cooling arrangement of high-pressure turbine vanes," Journal of Propulsion and Power, Vol. 32, No. 3, 2016, pp. 659-673.
doi: 10.2514/1.b35747

[51] Montomoli, F., Massini, M., and Salvadori, S., "Geometrical uncertainty in turbomachinery: Tip gap and fillet radius," Computers & Fluids, Vol. 46, No. 1, 2011, pp. 362-368.
doi: 10.1016/j.compfluid.2010.11.031

[52] Salvadori, S., Montomoli, F., Martelli, F., Adami, P., Chana, K. S., and Castillon, L., "Aerothermal study of the unsteady flow field in a transonic gas turbine with inlet temperature distortions," Journal of Turbomachinery, Vol. 133, No. 3, 2011, p. 031030.
doi: 10.1115/1.4002421

[53] Massini, M., Miller, R. J., and Hodson, H. P., "A new intermittent aspirated probe for the measurement of stagnation quantities in high temperature gases," Journal of Turbomachinery, Vol. 133, No. 4, 2011, p. 041022.
doi: 10.1115/1.4002414

[54] Montomoli, F., Carnevale, M., D'Ammaro, A., Massini, M., and Salvadori, S. *Uncertainty quantification in computational fluid dynamics and aircraft engines* Springer, 2015.

[55] Salvadori, S., Riccio, G., Insinna, M., and Martelli, F., "Analysis of combustor/vane interaction with decoupled and loosely coupled approaches," ASME Turbo Expo, GT2012-69038, Copenhagen, Denmark, 2012.

[56] Moeckel, C. W., "Probabilistic turbine blade thermal analysis of manufacturing variability and toleranced designs," Massachusetts Institute of Technology,Department of Aeronautics and Astronautics,Master thesis, 2006.

[57] Bunker, R. S., "The effects of manufacturing tolerances on gas turbine cooling," Journal of Turbomachinery, Vol. 131, No. 4, 2009, p. 041018.
doi: 10.1115/1.3072494

[58] *ANSYS14.5 CFX-solver theory guide*: ANSYS, Inc., 2012.

[59] Menter, F., and Rumsey, C., "Assessment of two-equation turbulence models for transonic flows," 25th AIAA Fluid Dynamics Conference, AIAA 94-2343, Colorado Springs, Colorado, 1994.
doi: 10.2514/6.1994-2343

[60] Menter, F. R., "Two-equation eddy-viscosity turbulence models for engineering applications," AIAA Journal, Vol. 32, No. 8, 1994, pp. 1598-1605.
doi: 10.2514/3.12149

[61] Ayoubi, C. E., "Three-dimensional aero-thermal optimization of film cooling in a high pressure turbine," Concordia University,Mechanical and Industrial Engineering,Ph. D dissertation, 2014.

[62] Blazek, J. *Computational fluid dynamics: Principles and applications, 3rd Edition*: Butterworth-Heinemann, 2015.

[63] Poling, B. E., Prausnitz, B. M., and O'Connell, J. P. *The properties of gases and liquids*. New York: McGraw-Hill, 2001.

[64] Cengel, Y. A., and Ghajar, A. J. *Heat and mass transfer: Fundamentals and applications*. New York: McGraw-Hill Education, 2014.

[65] Kadoya, K., Matsunaga, N., and Nagashima, A., "Viscosity and thermal conductivity of dry air in the gaseous phase," Journal of Physical and Chemical Reference Data, Vol. 14, No. 4, 1985, pp. 947-970.
doi: 10.1063/1.555744

[66] Simpson, T. W., Korte, J. J., Mauery, T. M., and Mistree, F., "Comparison of response surface and Kriging models for multidisciplinary design optimization," 7th AIAA/USAF/NASA/ISSMO Symposium on Multidisciplinary Analysis and Optimization, AIAA Paper 98-4755, St. Louis, MO, 1998.

[67] Simpson, T. W., Mauery, T. M., Korte, J. J., and Mistree, F., "Kriging models for global approximation in simulation-based multidisciplinary design optimization," AIAA Journal, Vol. 39, No. 12, 2001, pp. 2233-2241.
doi: 10.2514/2.1234

[68] Jeong, S., Murayama, M., and Yamamoto, K., "Efficient optimization design method using Kriging model," Journal of Aircraft, Vol. 42, No. 2, 2005, pp. 413-420.
doi: 10.2514/1.6386

[69] Montgomery, D. C. *Design and analysis of experiments, 8th Edition*: Wiley, 2012.

[70] McKay, M. D., Beckman, R. J., and Conover, W. J., "Comparison of three methods for selecting values of input variables in the analysis of output from a computer code," Technometrics, Vol. 21, No. 2, 1979, pp. 239-245.

[71] Bae, H. G., "A study on EGO method for aerodynamic optimal design," Korea Advanced Institute of Science and Technology,Mechanical Aerospace and Systems Engineering,Ph. D dissertation, 2012.

[72] Scholnlau, M., "Computer experiments and global optimization," University of Waterloo,Department of Statistics and Actuarial Science,Ph. D Thesis, 1997.

[73] Jeong, S., and Obayashi, S., "Efficient global optimization (EGO) for multi-objective problem and data mining," The 2005 IEEE Congress on Evolutionary Computation, 3, 2005, pp. 2138-2145.
doi: 10.1109/CEC.2005.1554959

[74] *Isight component guide*: Dassalt System, 2013.

[75] Deb, K., Agrawal, S., Pratap, A., and Meyarivan, T., "A fast elitist non-dominated sorting genetic algorithm for multi-objective optimization: NSGA-II," Lecture notes in computer science, Vol. 1917, 2000, pp. 849-858.
doi: 10.1007/3-540-45356-3_83

[76] Goldberg, D. E. *Genetic algorithms in search, optimization and machine learning*: Addison-Wesley Professional, 1989.

[77] Mitchell, M. *An introduction to genetic algorithms*. Cambridge: MIT Press, 1998.

[78] Rhee, D.-H., Kang, Y. S., Cha, B. J., Kang, J.-S., Lee, S., and Yee, K., "Film cooling performance improvement with optimized hole arrangements on pressure side surface of nozzle guide vane - Part II: Experimental validation," ASME Turbo Expo, Seoul, Korea, 2016.

[79] Kang, Y. S., Rhee, D. H., and Cha, B. J., "Aerodynamic design of high pressure turbine for aircraft turbofan engine," 7th National Congress on Fluids Engineering, 2012, p. 246~247.

[80] Shimoyama, K., Yoshimizu, S., Jeong, S., Obayashi, S., and Yokono, Y., "Multi-objective design optimization for a steam turbine stator blade using LES and GA," Journal of Computational Science and Technology, Vol. 5, No. 3, 2011, pp. 134-147.
doi: 10.1299/jcst.5.134

[81] Jeong, S., Chiba, K., and Obayashi, S., "Data mining for aerodynamic design space," Journal of Aerospace Computing, Information, and Communication, Vol. 2, No. 11, 2005, pp. 452-469.
doi: 10.2514/1.17308

[82] Abhari, R. S., "Impact of rotor–stator interaction on turbine blade film cooling," Journal of Turbomachinery, Vol. 118, No. 1, 1996, pp. 123-133.
doi: 10.1115/1.2836593

[83] Babaee, H., Wan, X., and Acharya, S., "Effect of uncertainty in blowing ratio on film cooling effectiveness," Journal of Heat Transfer, Vol. 136, No. 3, 2013, p. 031701.
doi: 10.1115/1.4025562

[84] Povey, T., and Qureshi, I., "Developments in hot-streak simulators for turbine testing," Journal of Turbomachinery, Vol. 131, No. 3, 2009, p. 031009.
doi: 10.1115/1.2987240

[85] Barringer, M. D., Thole, K. A., and Polanka, M. D., "Experimental evaluation of an inlet profile generator for high-pressure turbine tests," Journal of Turbomachinery, Vol. 129, No. 2, 2007, p. 382.
doi: 10.1115/1.2436897

[86] Boyce, M. P. *Gas turbine engineering handbook*: Elsevier, 2011.

국문초록

고압터빈은 운용 중 고온 고압의 환경에 노출되며 막냉각은 이런 극한환경에서 효과적으로 터빈요소를 보호한다. 이 기법은 많은 냉각기체를 소비하므로 효율적인 설계가 중요하며 이를 위한 대부분의 연구는 막냉각 홀의 형상최적화 위주로 수행되어 왔다. 그러나 막냉각 홀의 제작성과 내구성의 한계로 최근에는 막냉각 홀의 배열 최적화에 대한 효용성이 관심을 받고 있다.

한편 고압터빈 1 단 노즐의 막냉각 홀들의 높은 불확정성 환경에서 작동한다. 그 중 가장 큰 성능 변동의 요인은 터빈 입구와 냉각 시스템의 유동환경과 제작공차에서 비롯된다. 불확정성 요소에 대한 고려 없이 최적설계를 수행할 경우 설계환경에서 조금만 벗어나게 되더라도 치명적인 결함으로 이어질 수 있다.

본 연구에서는 고압터빈의 제작 및 작동환경 중 발생할 수 있는 불확정성 요소를 고려하여 막냉각 홀의 배열 최적화를 수행하였다. 먼저 변수 선정을 위해 막냉각 홀들을 각 열 별로 새로 정의한 형상함수를 이용해 매개화하였다. 설계를 위해서는 크리깅 모델을 이용한 효과적인 전역최적화 기법과, 몬테카를로 시뮬레이션, 유전알고리즘이 사용되었다. 불확정성 요소로는 제작공차, 분사비 및 터빈 입구 온도 프로파일의 변동이 고려되었으며 기존의 연구들을 참고하여 확률분포 함수와 변동범위를 정량화 하였다.

각각의 불확정성 요소에 대해 세 가지 종류의 독립적인 강건최적화를

수행해 더 높은 냉각성능을 보이면서 성능변동이 적은 막냉각 홀 배열을 도출하였으며 그 결과를 비교 분석하였다. 그 결과 막냉각 홀의 성능변동에 영향을 미치는 요소로 터빈 입구 온도 분포는 다른 두 불확정성 요소에 비해 상대적으로 영향력이 적고 유동상류에 관련된 확률변수가 막냉각 성능에 더욱 민감하며, 불확정성요소에 의한 성능변동 역시 유동상류에서 크게 나타남을 확인하였다.

주요어: 고압터빈, 막냉각, 홀 배열, 강건최적설계, 냉각시스템 불확정성, 제작공차, 분사비, 터빈입구온도

학번: 2012-30182

성명: 이상아